Photocatalytic Mineralisation of Toxic Chlorophenols and Removal of Cr (VI) in Aqueous Solution Using Cocatalyst Decorated TiO$_2$

Ayoola Shoneye

2021

A thesis submitted for the partial fulfilment of the requirements for the

degree of Doctor of Philosophy at University College London

Department of Chemical Engineering,

University College London,

London, United Kingdom

Declaration

I, Ayoola Shoneye, confirm that the work presented in this thesis is my own. Where information has been derived from other sources, I confirm that this has been indicated in the thesis.

Ayoola Shoneye

…………………………..

Signature

5th August 2021

…………………………..

Date

I. Acknowledgments

Firstly, I would like to express my sincere gratitude to my supervisor Prof. Junwang Tang, for his continued guidance and support to my research. If it had not been for his patience and words of encouragement, this thesis could not have been successful. I am also grateful to my secondary supervisor Prof. Daniel Brett for his helpful guidance and encouragements.

Great thanks to two Postdocs, Dr. Mustafa Bayazit and Dr. Savio Moniz, for their assistance with conducting experiments in the research laboratory, kind suggestions and beneficial discussions, which aided my research progress. I also appreciate the material characterisation technicians at UCL, including Mr. Martin Vickers (XRD), Mr. Steven Firth (Raman and SEM), Dr. Chi Pang and Dr. Mark Isaacs (XPS). Thanks to Dr. Jijia Xie for assisting with EDS analysis and Miss Yiyun Liu for helping with ESR measurements. I am also grateful to my colleagues in the Solar Energy and Advanced Materials (SEAM) research group at UCL, Dr. Madasamy Thangamuthu, Xiyi Li, Lunqiao Xiong, Hui Wang and Qingning Yang for their helpful and constructive comments.

 I would like to acknowledge my sponsors, Tertiary Education Trust Fund (TETFUND, Nigeria) and Federal Scholarship Board (FSB, Nigeria) for the Presidential scholarship in terms of tuition and living expenses.

I am deeply indebted to my lovely and highly inspiring wife Elizabeth Iyanoye Shoneye for exercising patience, understanding, trust and sacrificial

love, and my siblings Dr. Olumide Shoneye and Omotola Shoneye, and parents for their emotional support and words of encouragement.

II.   Abstract

One of the limitations confronting conventional water treatment technologies is the complete mineralisation of persistent organic pollutants (POPs) like chlorophenols and their derivatives. Therefore, it is important to find innovative and cost-effective techniques for the safe and complete destruction of these POPs. In the project, the possibility of enhancing the photocatalytic mineralisation activity of very benign titanium dioxide via surface modification by cocatalysts was systematically investigated.

A robust impregnation method was used to fabricate $Fe(III)/TiO_2$ composites. Highly dispersed Fe(III) oxide species on TiO_2 was optimised to achieve complete mineralisation of a few herbicides (2,4,6-trichlorophenol and 2,4-dichlorophenoxyacetic acid) under uv/visible light irradiation ($\lambda > 320$ nm). The consistent results were achieved by HPLC, TOC and UV-vis spectra measurements, which show among three Fe(III) oxide species, $Fe_4NO_3(OH)_{11}$, FeOOH and Fe_2O_3, FeOOH (0.1% Fe) is the best to improve TiO_2 activity, representing nearly two times activity of the benchmark PC50 TiO_2 photocatalyst for both herbicides tested. Such high activity was attributed to the enhanced photo-generated electron-hole separation and improved generation of hydroxyl radicals.

Next, the surface modification of TiO_2 with Fe-based alloys was also investigated under similar operating conditions. Both Fe-Cu and Fe-Co oxide alloys were found to improve the photocatalytic performance of

optimised Fe/TiO_2 towards complete mineralisation of 2,4,6-TCP with 108% and 155% enhancement, respectively in 3 h compared with TiO_2. In order to eliminate catalyst recovery cost in slurry/suspension systems, the immobilisation of photocatalysts on a rigid and photo-chemically stable polymer as a robust support was also investigated for the photocatalytic removal of methylene blue and Cr (VI) ions, which is close to the real condition for water treatment. The results were compared with those achieved under slurry/suspension system and indicated the immobilisation is a robust way to implement the technology for real water treatment.

III. Impact statement

Water security for domestic and industrial use is becoming a global concern due to environmental pollution from natural and man-made activities. According to the United Nations (UN), over two billion people (approximately 25% of the world population) do not have access to clean and safe water, especially in low and middle-income countries (LMIC). Conventional water treatment technologies such as filtration, sedimentation, coagulation, flocculation, adsorption and chlorination are presently employed in order to meet global water demand. However, most of these technologies are incapable of complete destruction of toxic organic pollutants and by-products.

Photocatalysis is a technology which employs a semiconductor for light-driven chemical reactions, mostly under ambient conditions. TiO_2 has been used in the past two decades for the photocatalytic degradation of organic contaminants due to its low-cost, low toxicity, outstanding photo-stability, excellent band alignment to many oxidation-reduction reactions and possibility for further functionalisation. However, the fast recombination of photogenerated electron–hole pairs and inappropriate reaction sites for many redox reactions are still serious challenges in TiO_2-based photocatalytic processes, leading to lower reaction efficiencies, which must be overcome in order to meet the requirement of practical applications. Therefore, in the project, a robust and economical strategy was used to enhance the photo-activity of TiO_2 nanoparticles by cocatalyst- decoration,

leading to complete photocatalytic mineralisation of non-biodegradable herbicides and derivatives under solar irradiation. The findings further proposed the use of cocatalyst alloys to improve the photocatalytic activity of TiO_2 and immobilisation on a robust UV curable polymer for practicability and sustainability on a large scale. Such novel findings will be useful in the area of fabrication of low-cost, efficient and robust photocatalysts for water treatment. Furthermore the fundamental studies carried out in this project will provide very useful information to the society in solar energy, photocatalysis and environmental purification about charge generation, separation and utilisation.

IV.   Publication & Conferences

Publications

1)   **A. Shoneye**, J.S. Chang, M.N. Chong and J. Tang, Paper title: *"Recent progress in photocatalytic degradation of non-biodegradable organic contaminants and reduction of heavy metal ions in water by TiO_2-based catalysts"*, **International Materials Reviews**, (2021). doi.org/10.1080/09506608.2021.1891368

2)   **A. Shoneye** and J. Tang, Paper title: *"Highly dispersed FeOOH to enhance photocatalytic activity of TiO_2 for complete mineralisation of herbicides"*, **Applied Surf. Sci.**, 511 (2020), 145479.

3)   F. Fu, H. Shen, X. Sun, W. Xue, **A. Shoneye**, J. Ma, L. Luo, D. Wang, J. Wang, J. Tang, Paper title: *"Synergistic Effect of Surface Oxygen Vacancies and Interfacial Charge Transfer on $Fe(III)/Bi_2MoO_6$ for Efficient Photocatalysis"*, **Appl. Catal. B Environ**., 247 (2019) 150–162.

4)   **A. Shoneye** and J. Tang, Paper title: *"Bimetallic FeO_x-MO_x loaded TiO_2 (M = Cu, Co) nanocomposite photocatalysts for complete mineralisation of herbicides"* (Submitted to: Chemistry – A European Journal).

Conference presentations

1)   **Ayoola Shoneye** and Junwang Tang, Poster title: *"Photocatalytic wastewater treatment"*, RSC Chemical Nanoscience & Nanotechnology Group Annual Symposium, The Royal Society of Chemistry, Burlington House, London, 2018.

2)   **Ayoola Shoneye**, Savio Moniz and Junwang Tang, Poster title: *"Photocatalytic decontamination of wastewater using heterojunctions of Fe/Cu decorated TiO$_2$"*, Environmental Chemistry of Water, Sediment and Soil: Early Career Researchers Meeting Programme, The Royal Society of Chemistry, Burlington House, London, 2016.

V.   Table of contents

VI.   List of tables

VII. List of figures

VIII. List of symbols and abbreviations

1,5-DPC – 1,5-diphenylcarbazide

2,4-D – 2,4-dichlorophenoxyacetic

2,4-DCP – 2,4-dichlorophenol

2,4,5-T – 2,4,5-trichlorophenoxyacetic acid

2,4,6-TCP – 2,4,6-trichlorophenol

2,4,6-TCR – 2,4,6-trichlororesorcinol

2,6-DCBT – 2,6-dichlorobenzene-1,3,4-triol

2,6-DCBQ – 2,6-dichloro-1,4-benzoquinone

2,6-DCHQ – 2,6-dichlorohydroquinone

2,6-DCHBQ – 2,6-dichloro-3-hydroxy-1,4-benzoquinone

3,5-DCC – 3,5-dichlorocatechol

7-HC – 7-hydroxycoumarin

BET – Brunauer–Emmett–Teller

CB – Conduction band

CBM – Conduction band minimum

COU – Coumarin

Cr (VI) – Chromium (VI) or hexavalent chromium

CTAB – Cetyltrimethylammonium bromide

CPs – Chlorophenols

DI – De-ionised

DOC – Dissolved organic carbon

DMPO – 5,5'-dimethyl-1-pyrroline-N-oxide

DRS – Diffuse reflectance spectroscopy

EDS – Energy-dispersive X-ray spectroscopy

EDTA – Ethylenediaminetetraacetic acid

ESI-MS – Electrospray ionisation – Mass spectrometry

ESR – Electron spin resonance

FTIR – Fourier-transform infrared

GO – Graphene oxide

HPLC- MS – High performance liquid chromatography – Mass spectrometry

HTAB – Hexadecyltrimethylammonium bromide

IC – Inorganic carbon

IPA – Isopropanol

JCPDS – Joint Committee on Powder Diffraction Standards

KHP – Potassium hydrogen phthalate

LED – Light emitting diode

LMIC – Low and middle-income countries

MB – Methylene blue

NPOC – Non-purgeable organic carbon

NTs – Nanotubes

$^{\bullet}OH$ – Hydroxyl radical

OH^- – Hydroxyl ion

$^{\bullet}O_2^-$ – Superoxide radical

Pc – Phthalocyanine

PCP – Pentachlorophenol

PDA – Photodiode array

pH_{nat} – Natural pH

PL – Photoluminescence

POM – Poly-oxo-tungstate

POPs – Persistent organic pollutants

PTFE – Polytetrafluoroethylene

PVA – Polyvinyl acetate

RGO – Reduced graphene oxide

ROS – Reactive oxygen species

SEM – Scanning electron microscopy

TC – Total carbon

TEM – Transmission electron microscopy

TiO_2 – Titanium dioxide otherwise known as Titanium (IV) oxide or Titania

TOC – Total organic carbon

TOC-L – Total organic carbon – liquid

US EPA – United States Environmental Protection Agency

UV-vis – Ultraviolet – visible

VB – Valence band

VBM – Valence band maximum

XRD – X-ray diffraction

XPS – X-ray photoelectron spectroscopy

1   Introduction

1.1   Background

Access to potable water is one of the biggest challenges globally, especially in low and middle-income countries (LMIC). Several persistent organic pollutants (pharmaceuticals, pesticides, personal care products, endocrine disrupters) are frequently detected in wastewater effluents.[1–3] Chlorophenols (CPs) and their metabolites are common and recalcitrant environmental pollutants, believed to have high bioaccumulation capability and carcinogenic effect. Four major chlorophenols: 2-chlorophenol (2-CP), 2,4-dichlorophenol (2,4-DCP), 2,4,6-trichlorophenol (2,4,6-TCP) and pentachlorophenol (PCP) have been classified as first degree toxic pollutants by the US Environmental Protection Agency (EPA 2003).[4,5] The UK Water Act, according to the Drinking Water Inspectorate (DWI), recommends a maximum allowable concentration of 0.1 µg/L for individual chlorophenols (herbicides) and 50 µg/L for chromium in consumers' taps.[6]
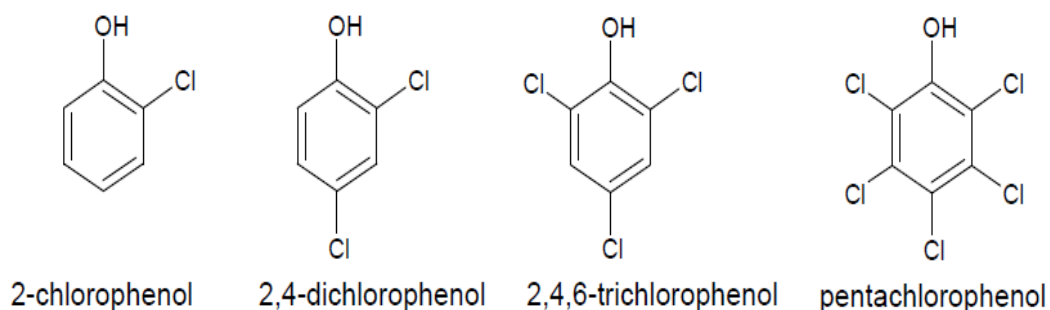
Figure 1-1 Chemical structures of some common chlorinated phenols.

Adverse effects of phenolic compounds on the human nervous system have been reported and linked to several health disorders e.g. kidney failure, liver and lung damage.[4,5,7] Chlorophenols find extensive application in the chemical, forestry, and wood-working industries. They are used as herbicides, insecticides, fungicides, wood preservatives and chemical intermediates.[4,8–10] Generally, these organic pollutants are released into the environment because of several man-made activities including water disinfection, waste incineration, uncontrolled use of pesticides and herbicides, and as by-products in the bleaching of paper pulp with chlorine.[11] It is interesting to note that 2-CP, 4-CP, 2,4-DCP and 2,4,5-TCP are the most significant chlorophenols formed as by-products of water chlorination.[12,13] Effluents from a pulp and paper mill were analysed before treatment and subsequent discharge into the Lake Baikal in Russia, 2,4-DCP concentration of (630 ± 50) µg/L, 2,4,5-TCP concentration of (2,660 ± 210) µg/L and 2,4,6-TCP concentration of (320 ± 30) µg/L were reported.[14] After treatment, the individual chlorinated phenols were present in trace quantities, except for 2,4,5-TCP with concentration of (560 ± 50) µg/L.[14] Environmental protection agencies and health organisations recommended a maximum allowable concentration for chlorinated phenols as: 0.1 µg/L in drinking water and 200 µg/L in wastewater.[12]

Various strategies have been employed to remove CPs from the environment. Conventional methods include coagulation-flocculation, reverse osmosis, active carbon adsorption, biodegradation, air stripping and incineration. However, these techniques have some drawbacks and

limitations e.g. toxic by-product generation, incomplete mineralisation, low efficiency, high energy and capital cost.[12–15] Chlorophenols absorb light of wavelength below 290 nm; thus, they do not undergo direct sunlight photolysis due to little UV photons with such short wavelength in solar spectrum reaching the earth.[16] Also, they are difficult to decompose completely to CO_2 and HCl by conventional methods due to high stability of the benzene ring.[17] Therefore, it is important to find innovative and cost-effective techniques for the safe and complete degradation of chlorinated organic pollutants such as chlorophenols.

Table 1-1 Conventional approaches to removal of chlorinated phenols.[18]

Treatment approach	Drawbacks
Biological treatment	Very slow, incomplete degradation and by-products may be more toxic than the contaminants.
Adsorption technology	Expensive due to regeneration of the adsorbent materials and post-treatment of solid wastes.
Chemical precipitation	Expensive due to high dosage of chemicals and produce large quantity of sludge which need post-treatment.
Air stripping	High capital cost due to off-gas treatment, aesthetic constraints and technically not reliable.

The current trend in wastewater treatment has moved from simple phase transfer to destruction of pollutants such as by advanced oxidation processes (AOPs). These techniques involve reactive free radical species for non-selective mineralisation of organic compounds to harmless end products. The AOPs are generally based on the generation of the hydroxyl radicals ($^{\cdot}$OH), which have a great oxidation power, thus can almost oxidize all organic compounds to carbon dioxide and water.[18] There are several methods for generating hydroxyl radicals, e.g. Fenton-based processes, UV-based processes, Ozone based processes and Photocatalytic processes.[15,19–21]

In spite of the advantages of AOPs, there are several limitations in their use for each AOP: (a) costs may be higher than competing technologies because of energy requirements, (b) harmful intermediates may be formed, (c) pre-treatment of the wastewater may be required to minimise cleaning and maintenance of UV reactor and quartz sleeves, (d) handling and storage of ozone and hydrogen peroxide require special safety precautions and (e) major challenges for the photocatalytic process are catalyst deactivation, slow kinetics, low photo efficiency, and unpredictable mechanism.[22] However, AOPs are still more effective than the other techniques for wastewater treatment containing toxic and persistent pollutants.[18]

Over the past decades, application of titanium dioxide photocatalytic oxidation technology in environmental remediation has gained considerable

attention as a cheap and clean alternative, though there are still various challenges to be resolved for its commercialisation. A high number of organic compounds (dyes, drug residues, pesticides and herbicides) have been eliminated from both aquatic and atmospheric environment via photocatalysis.[23–25]

1.2   Motivation, aim and objectives

The importance of water for sustenance of life cannot be overemphasised. In LMIC, clean water supplies are crucial for drinking and sanitation purposes, the rearing of livestock and growing crops. It was reported that about 80% of illnesses in LMIC are linked to poor water and sanitation conditions.[26] Water security is presently a global concern, because of the increasing demand for clean water due to population growth, climate change and economic activities.[27,28]

A large proportion of the LMIC are in regions that are naturally endowed with the most favourable conditions for solar technology implementation, such as high solar insolation. Nigeria (case study), with an average solar insolation of 5.5 kWh/m^2/day, is located on latitude 10 °N of the Equator, and on longitude 8 °E of the Greenwich meridian. The mean daily temperature is between 25 and 30 °C. The population is more than 150 million, spread unevenly over a national territory of 923,770 km^2. Nigeria has the eighth largest national population in the world. Water pollution in Nigeria occurs in both rural and urban areas. In rural areas, drinking water

from natural sources such as rivers and streams is usually polluted by organic substances from upstream users, such as farmers, whose organic pesticides and herbicides are easily washed into the river water, resulting in high levels of persistent organic contamination. Poverty, lack of adequate education, low budgetary funding, inefficient government policies and other anthropogenic factors, are highly contributing, to the pollution of domestic water supplies in these communities.[27–30]

Conventional water treatment technologies, such as filtration, coagulation/flocculation and adsorption using active carbon (AC), are limited in application in these rural areas due to their high capital cost and energy requirements; particularly in terms of inadequate or no electricity supplies in such rural communities. Unlike conventional water treatment technologies, which are often expensive and used primarily in urban centres, solar-driven photocatalytic water purification technology combined with stable photocatalyst materials, is a decentralised system and can be easily implemented across rural communities with little or no technical difficulty.

However, TiO_2 photocatalysis is limited in environmental application due to low efficiency dominated by a few key factors like poor visible light absorption, low adsorption capacity for contaminants and high recombination rate of photogenerated electrons and holes.[31] It is a common practice to use noble metals (Ag, Au, Pd, Pt, Ru) to enhance its photocatalytic efficiency. However, this approach will be expensive for the technology implementation on a large scale, if it is to be used in LMIC. So,

the use of earth-abundant materials in TiO_2 modification will be targeted, and optimise the synthesis process to achieve remarkable degradation efficiency for persistent organic contaminants.

The aim of this thesis is to investigate the photocatalytic mineralisation of chlorophenols and the removal of Cr(VI) in aqueous solution using cocatalyst decorated TiO_2. Optimised photocatalysts will then be prepared on a rigid and photo-chemically stable polymer as solid support and investigated for the photocatalytic oxidation of methylene blue (MB) and reduction of Cr (VI) to Cr (III), and results compared with those achieved under slurry/suspension system, which could be used in a decentralised water purification system.

Objectives:

1. Optimise the photocatalyst fabrication and properties by addition of earth-abundant cocatalysts (Fe, Cu and Co) onto TiO_2 and their alloys.

2. Investigate the rate of total organic carbon (TOC) removal during photocatalytic mineralisation of the pollutants of 2,4,6-trichlorophenol (2,4,6-TCP) and 2,4-dichlorophenoxyacetic acid (2,4-D).

3. Investigate the degradation pathway of 2,4,6-TCP by TiO_2-based junctions and possible intermediate products using HPLC-MS.

4. Investigate the redox mechanism across the photocatalyst surface by observing the effect of (holes, electrons, hydroxyl radical and superoxide radical) scavengers on photocatalytic efficiency.

5. Investigate the photocatalytic degradation of four different herbicides (2,4-DCP, 2,4,6-TCP, 2,4-D and 2,4,5-T), by optimised alloy cocatalyst decorated-TiO_2 sample, to demonstrate its wide feasibility.

6. Immobilise the optimised photocatalysts in a polymer and investigate photocatalytic activities for the removal of MB and Cr (VI) ions due to covid-19 pandemic and non-availability of HPLC for herbicides analysis.

1.3   Report outline

This project will focus on the enhancement of TiO_2 photocatalytic mineralisation efficiency, using 2,4,6-TCP as a model organic contaminant in water. In the first chapter, the background of persistent organic pollutants, with interest in chlorinated phenols is discussed, while considering the sources of these contaminants and environmental impact in details. In addition, the limitations of conventional water purification technologies, the advantages of photocatalysis as one of the advanced oxidation processes, and the motivation to conduct this research are presented. In the second chapter, the principle of TiO_2 photocatalysis, organic contaminant degradation mechanism, limitations of TiO_2-based environmental application

and countermeasures or strategies used in improving its performance will be discussed. In the third chapter, the methodology used for material synthesis, material characterisation, and photocatalytic degradation efficiency test will be described. Nanocomposites comprising earth abundant cocatalyst (e.g. Fe^{III}/TiO_2) with optimised synthesis procedure and performance for the complete mineralisation of 2,4,6-TCP will be demonstrated in the fourth chapter. Optimisation of TiO_2 photocatalytic performance using Fe-based alloys for complete mineralisation of some herbicides will be demonstrated in fifth chapter. In the sixth chapter, the practicability of immobilised powder photocatalysts in a polymer for decomposition of MB and reduction of Cr (VI) ions will be presented. A summary and conclusion of the experimental results, and some proposed future work on the optimisation of TiO_2 photocatalytic mineralisation efficiency (i.e. novel techniques in overcoming the highlighted challenges of TiO_2-based environmental application) and new photocatalysts development, will be discussed in the seventh chapter.

2   Literature review

2.1   Introduction

This review addressed the background in photocatalysis, and the removal of wastewater contaminants, via irradiation of semiconductors (e.g. nano-TiO_2) with a light of energy higher than its bandgap energy (**Figure 2-1**). This is the first step in photocatalysis. Subsequently, the excitation of photo-generated electrons into the conduction band takes place, leaving behind energetic photo-generated holes in the valence band. Oxidation reaction is initiated in the valence band, while reduction reaction is initiated in the conduction band of the semiconductor. This requires the semiconductor to have proper band alignment required for organic pollutant decomposition (**Figure 2-2**), e.g. the conduction band minimum (CBM) should be higher (more negative in potential) than the redox potential for oxygen reduction to superoxide radicals, and its valence band maximum (VBM) should be lower (more positive in potential) than the redox potential for water or hydroxyl ion oxidation to hydroxyl radicals.[13,32]
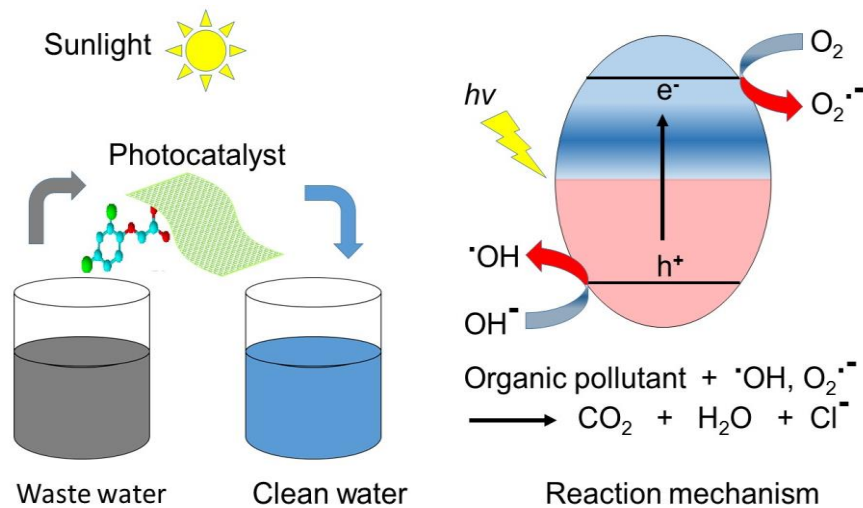
Figure 2-1 Diagram illustrating the principle of semiconductor photocatalysis for wastewater treatment.

2.2 Titanium dioxide Photocatalysis

2.2.1 Titanium dioxide as a photocatalyst

One of the most important aspects of environmental photocatalysis is the availability of an efficient photocatalyst, which should have several respects. For example, it is relatively inexpensive, physically and chemically stable, and non-toxic. Also, the band alignment in such a photocatalyst (**Figure 2-2**) makes the photo-generated holes to be highly oxidising. In addition, photo-generated electrons have reduction potential enough to produce superoxide radical from oxygen.[33–35] TiO_2 is the typical material meeting these criteria. Zhang *et al.*[36] and Hirakawa *et al.*[37], based on experimental evidence, proved that the conduction band electrons in TiO_2 have the potential to generate superoxide radicals (O_2^-) from dissolved oxygen in water.
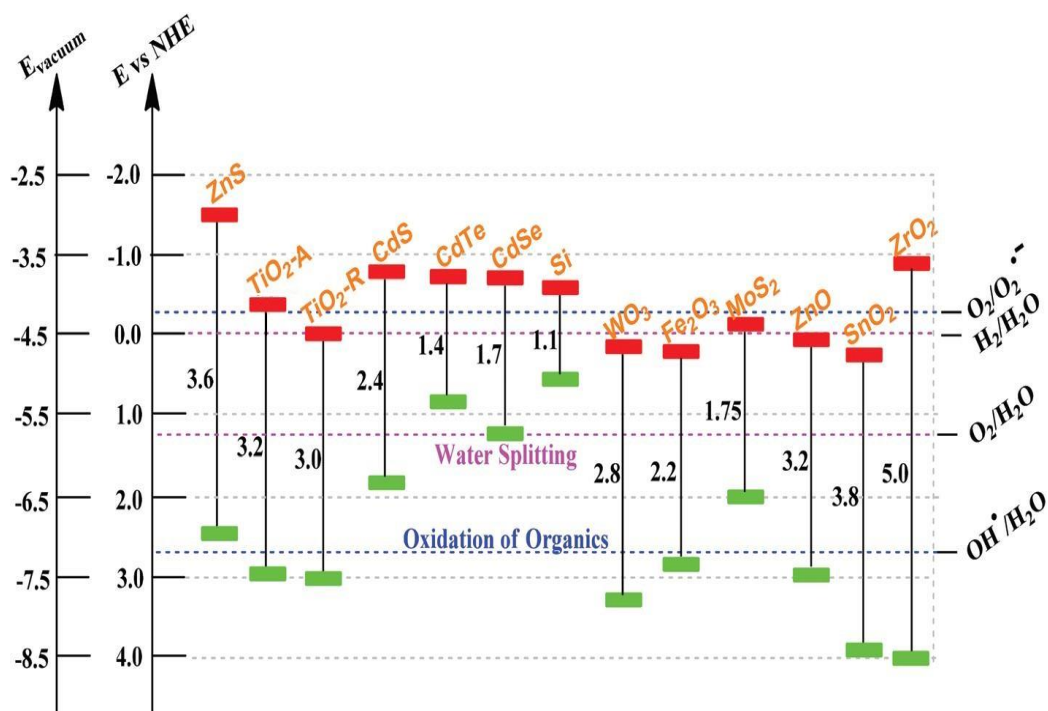
Figure 2-2 Diagram illustrating the bandgap energy, VB and CB positions of some common semiconductors. Adapted from Wu et al.[33] Copyright 2015, Royal Society of Chemistry. Reprinted with permission.

2.2.2 Physico-chemical properties of TiO$_2$ photocatalyst

Titania (TiO$_2$) is a white oxide of titanium: a white crystalline compound. The available sources include: anatase (tetragonal), brookite (orthorhombic), rutile (tetragonal), ilmenite (FeTiO$_3$) and other minerals. The metastable anatase and brookite phases convert irreversibly to the rutile phase upon heating at temperatures above 600 °C.[38,39] TiO$_2$ is often used as pigment for durable paints and plastics.[40]

Table 2-1 Specification and characterisation of some commercial TiO_2.[41]

Properties	Degussa P25	Millennium PC50	Sigma 325 mesh
TiO_2 content (%) [a]	> 99.5	98.2	99
Composition	80% Anatase, 20% Rutile	100% Anatase	95% Anatase, 5% Rutile [a]
Crystallite size [a]	25 – 30 nm	20 – 30 nm	≤ 45 µm
Surface Area ($m^2\ g^{-1}$) [a]	55 ± 15	50 ± 5	9 – 11
Solubility in water	Insoluble	Insoluble	Insoluble

[a] Information provided by supplier

2.2.3 Titanium dioxide photocatalytic mechanism

The reactions involved in TiO_2 photocatalysis in the presence of an organic pollutant are as follows,[42–44] where the contaminant adsorption on the catalyst surface is required for efficient degradation of contaminants.

In simple terms, titanium dioxide generates conduction band (CB) electrons and valence band (VB) holes upon UV light irradiation.

$$TiO_2 \quad + \quad h\nu \quad \rightarrow \quad TiO_2 \ (e_{CB}^- \ + \ h_{VB}^+) \qquad\qquad Eq.\,(2-1)$$

The hydroxide ions in water react with the VB holes to generate hydroxyl radicals on TiO_2 surface.

$$TiO_2 \ (h_{VB}^+) \quad + \quad OH^- \quad \rightarrow \quad TiO_2 \quad + \quad \cdot OH \qquad\qquad Eq.\,(2-2)$$
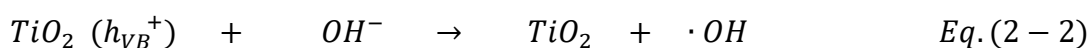
The CB electrons reduce oxygen molecules to produce superoxide radicals.

$$TiO_2 \ (e_{CB}^-) \quad + \quad O_2 \quad \rightarrow \quad TiO_2 \quad + \quad \cdot O_2^- \qquad\qquad Eq.\,(2-3)$$
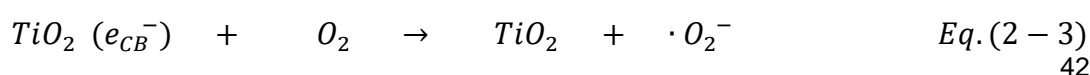
The superoxide radicals can combine with hydrogen ions to give perhydroxyl radicals.

$$\cdot O_2^- \quad + \quad H^+ \quad \rightarrow \quad HO_2^\cdot \qquad\qquad Eq.(2-4)$$

Two perhydroxyl or hydroperoxyl radicals can combine to produce hydrogen peroxide.

$$HO_2^\cdot \quad + \quad HO_2^\cdot \quad \rightarrow \quad H_2O_2 \quad + \quad O_2 \qquad\qquad Eq.(2-5)$$

The CB electrons can react with hydrogen peroxide to produce more hydroxyl radicals.

$$TiO_2 \ (e_{CB}^-) \quad + \quad H_2O_2 \quad \rightarrow \quad \cdot OH \quad + \quad OH^- \qquad Eq.(2-6)$$
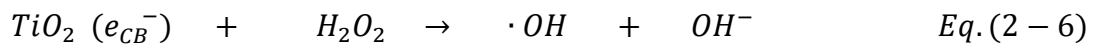
The superoxide radicals react with hydrogen peroxide to also generate hydroxyl radicals.

$$H_2O_2 \quad + \quad \cdot O_2^- \quad \rightarrow \quad \cdot OH \quad + \quad OH^- \quad + \quad O_2 \qquad Eq.(2-7)$$
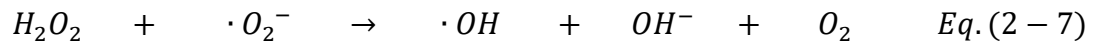
Next, the hydroxyl radicals can react directly with the organic pollutant (R-H) to form products.

$$R-H \ + \ \cdot OH \quad \rightarrow \quad Degradation\ products \dots CO_2 \ + \ H_2O \quad Eq.(2-8)$$
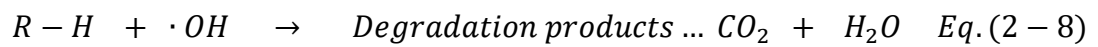
Charge–carrier trapping in bulk/surface defects of TiO_2

$$TiO_2 \ (e_{CB}^-) \qquad \rightarrow \qquad TiO_2 \ (e_{TR}^-) \qquad\qquad Eq.(2-9a)$$

$$TiO_2 \ (h_{VB}^+) \qquad \rightarrow \qquad TiO_2 \ (h_{TR}^+) \qquad\qquad Eq.(2-9b)$$

Electron–hole recombination

$$TiO_2 \ (e_{TR}^-) \ + \ TiO_2 \ (h_{TR}^+) \ \rightarrow \ TiO_2 \ (e_{CB}^-) \ + \ heat \quad Eq.\,(2-10)$$
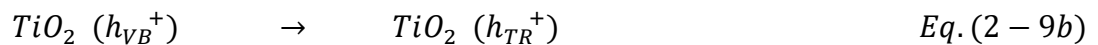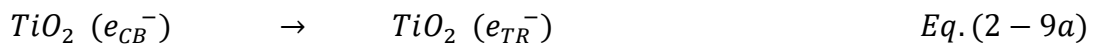
Table 2-2 Oxidation potentials of some oxidising agents.[45]

Species	Oxidation potentials (V)
Fluorine	3.03
VB holes of anatase and rutile	3.00
Hydroxyl radical	2.80
Atomic oxygen	2.42
Ozone	2.07
Hydrogen peroxide	1.78
Chlorine	1.36
Hydrogen	0.00
CB electrons in rutile	0.00
CB electrons in anatase	-0.15

Table 2-2 shows the oxidation potentials of some common oxidising agents. Following fluorine, the valence band holes of TiO_2 and hydroxyl radicals have the highest oxidation potential of 3.00 and 2.80 V, respectively. This justifies the reason why most organic pollutants can be degraded during TiO_2 photocatalysis.

2.2.4 Limitations in TiO_2 environmental application

The most studied phases of TiO_2 are anatase and rutile. The anatase phase is known to display higher photocatalytic activity than the rutile phase. The lower activity observed in rutile (E_g = 3.0 eV, λ = 413 nm), despite its lower band gap (E_g) energy than anatase (E_g = 3.2 eV, λ = 388 nm), is attributed to the rapid rate of electron-hole recombination. Also, the CBM of anatase is about 0.2 eV higher than that of rutile (**Figure 2-2** and **Table 2-2**). This implies that the conduction band electrons in anatase are more reductive than those in rutile.[31,46]

However, the inefficient utilisation of visible light, and high recombination rate of photoelectrons and holes, that drastically reduces quantum efficiency, are the major drawbacks of anatase TiO_2 application.[47,48] The challenges with TiO_2 as a potential photocatalyst for the removal of organic pollutants in wastewater are summarised in **Figure 2-3**. The challenges include, inefficient utilisation of visible light due to its large band gap, low adsorption of organic pollutants on catalyst surface due to its low surface area, aggregation of nano-sized TiO_2 particles in solution, difficulty in distributing the TiO_2 particles uniformly in solution and difficulty in recovery of nano-sized TiO_2 particles from solution. The corresponding countermeasures used in overcoming TiO_2 limitations in photocatalytic water treatment are discussed in detail below.
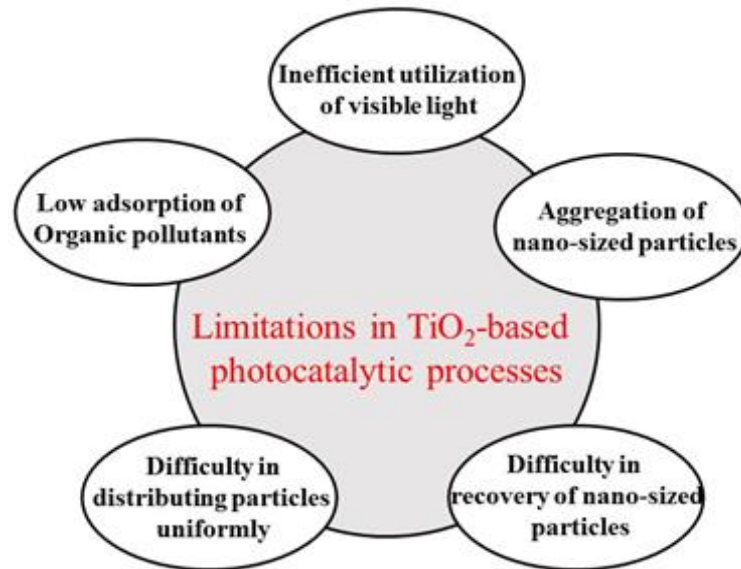
Figure 2-3 Limitations in TiO$_2$ photocatalytic processes for the degradation of organic pollutants. Adapted from Dong et al.[31]. Copyright 2015, Elsevier. Reprinted with permission.

2.2.5 Countermeasures used in overcoming TiO$_2$ limitations

Several approaches have been employed in overcoming the challenges facing TiO$_2$ photocatalytic application.

2.2.5.1 Visible light enhancement

The ultraviolet (UV) region only accounts for less than 5% of the entire solar spectrum, which TiO$_2$ is responsive to. The strategies used in extending the optical absorption of TiO$_2$ into the visible region include, metal-doping, non-metal doping, dyes sensitisation and direct reduction of TiO$_2$ (e.g., hydrogenation, chemical reduction and electrochemical reduction). Three of the methods will be addressed here.

(a) **Metal–doped TiO$_2$** (e.g., Ag, Pt, Au, Fe, Cu, Co, Ni, Cr, Mn and Ru). This method has been extensively investigated over the past decades for improving the photocatalytic degradation efficiency of TiO$_2$ for several organic pollutants under visible light (λ > 420 nm).[31,49] Khan *et al.* reported the synthesis of Ag doped TiO$_2$ using sol-gel method and the application in photocatalytic degradation of oxytetracycline under UV-visible light irradiation. The experimental results indicated 70 and 100% photocatalytic degradation of oxytetracycline in 60 min with pure TiO$_2$ and 1.9 wt.% Ag/TiO$_2$, respectively under UV-visible light irradiation. With only visible light irradiation (λ > 420 nm), the degradation efficiency of the 1.9 wt.% Ag/TiO$_2$ sample reduced drastically to 60% .[50] Generally for metal-doped TiO$_2$, the metal ion doping can either be substitutional or interstitial in the TiO$_2$ crystal lattice and can also form a mixture of oxides.[50–55] The limiting factors with this strategy include the nature of dopant species, dopant concentration, photochemical stability and thermal treatment. Several methods employed in metal-doped TiO$_2$ (e.g., impregnation, co–precipitation and sol–gel) were reported in literature.[56–58] The visible light activity of metal-doped TiO$_2$ is primarily due to the introduction of new energy levels in the bandgap of TiO$_2$, and photo-generated electrons can be excited from the defect state to the conduction band in TiO$_2$. Dopant ions above the optimum dosage could act as electron-hole recombination centres and will automatically reduce photocatalytic efficiency.[31]

(b) **Non-metal–doped TiO$_2$** (e.g., S, N, C, P, F and B). This method extends the visible light absorption of TiO$_2$ more than metal-doped

counterparts. This is because their impurity states are close to the valence band edge of TiO_2.[31] Compared to other non-metals, the N-doped and C-doped TiO_2 powders have been reported to show exceptional photocatalytic activity under visible light irradiation. Chen *et al.* prepared $C-TiO_2$, $N-TiO_2$ and $C-N-TiO_2$ using sol-gel method and tested their photocatalytic activities for the degradation of methylene under visible light irradiation.[59] In the absence of catalysts, about 5% photodegradation of MB was observed in 7 h. The C-N co-doped sample exhibited the highest efficiency with about 95% MB removal in 7 h, while 26, 60 and 70% degradation efficiencies were observed for unmodified TiO_2, $N-TiO_2$ and $C-TiO_2$ samples, respectively. The major drawbacks associated with non-metal doping include, formation of oxygen vacancies in the bulk in which the created defects act as electron-hole recombination sites, thus reducing the visible light photocatalytic efficiency. More so, instability is a major concern due to liberation of doped non-metals atoms in solution during photocatalysis.[60,61]

(c) **Reduced TiO_2** (TiO_{2-x}). Hydrogenation of TiO_2 was reported in 2011 by Chen *et al.* as an effective method in shifting the bandgap of TiO_2 to around 1.5 eV (~820 nm) with an optical onset of around 1.0 eV (black TiO_2).[62] The photocatalytic activity of the coloured TiO_2 was compared with unmodified TiO_2 for MB decomposition under solar light irradiation. Complete bleaching of MB was achieved after 8 min for the black TiO_2, while the unmodified white TiO_2 under the same experimental conditions, took nearly 1 hour. Under similar experimental conditions, complete degradation of phenol was achieved after 40 min for the black TiO_2, while the unmodified TiO_2 took 80

min to achieve the same. Total organic carbon (TOC) removal efficiency of the black TiO_2 was not reported by the author. Furthermore, without any form of treatment, the black TiO_2 was highly stable after 8 successive photocatalytic degradation cycles. This discovery led to an extensive research into coloured TiO_2 synthesis globally. Other methods used in fabricating reduced TiO_2 include, Al reduction,[63] Zn reduction,[64] imidazole reduction,[65] $NaBH_4$ reduction,[66] CaH_2 reduction,[67] and electrochemical reduction.[68] It has been widely accepted that heating TiO_2 under vacuum or in a reducing atmosphere also leads to colour changes.[69] The coloured TiO_2 (red, yellow, blue or black) resulted from the creation of Ti^{3+} or/and oxygen vacancies in the white TiO_2. However, their activities in the visible region are still far from satisfactory.[69,70]

2.2.5.2   Improved adsorption of organic pollutants

The photocatalytic activity of TiO_2 is also dependent on its adsorption capacity for the pollutants in aqueous solution. Several approaches have been used to overcome the low adsorption capacity of TiO_2. Modification of TiO_2 with some chelating ligands (arginine and salicylic acid) and carbon nanomaterials (graphene, carbon nanotubes and activated carbon) have been reported to enhance the adsorption of organic water contaminants.[71–73] With respect to doping with carbon-based nanoparticles, the higher adsorption capability and better photocatalytic activity were reported to be related to their high surface area, high conductivity and high visible light absorption intensity.[64,65]

2.2.5.3   TiO$_2$ particles stabilisation

TiO$_2$ particles suffer from severe aggregation during photocatalytic application, which will reduce their active sites and light harvesting capability. Since photocatalytic degradation occurs at the surface of TiO$_2$, mass transfer limitations need to be reduced for its effective application in water treatment.[74,75] Two possible approaches employed are:

(a) **Stabilisation by support structures** (glass beads, fibre glass, glass pellets, glass sheets, silica, organo-clays, stainless steel, Al$_2$O$_3$ fibre, quartz beads, polymers, activated carbon and zeolites).[74] However, there is still no ideal support that is suitable in terms of mechanical stability and selectivity.[75] Immobilisation on supports reduces TiO$_2$ surface area-to-volume ratio and the photocatalytic efficiency compared to unsupported TiO$_2$ particles.[76]

(b) **Stabilisation by surface modification** (humic acid, carboxylic acids, amino acids and polylactic acid). This method tends to generate high negatively charged density (zeta potential) on the TiO$_2$ surface and promotes repulsive forces among particles, thus reduces aggregation rate. The main drawback is the stability of these organic modifiers during photocatalysis.[77–80]

2.2.5.4   Separation of TiO$_2$ particles from solution

Recovery of fine particles of TiO$_2$ from solution is a huge challenge in suspension systems. Thus, the recovery and reusability of TiO$_2$ is required

before the technology can proceed beyond lab scale to industrial application. Two potential approaches applied are:

(a) **Immobilisation on solid supports** (glass fibres, glass, quartz and stainless steel). This method has been discussed under TiO_2 particles stabilisation using solid supports.[76] Although this approach overcomes the solid-liquid separation problem, slurry-type reactors are still more efficient over immobilised catalyst-type reactors, due to the availability of catalyst's surface and superior mass-transfer properties.[81]

(b) **Magnetic separation** (Fe_3O_4, γ-Fe_2O_3, $NiFe_2O_4$, $CoFe_2O_4$, FeCo and Co_3O_4). Compared to other magnetic materials, magnetite (Fe_3O_4) has received considerable attention due to its remarkable magnetic properties, low toxicity and biocompatibility.[82–84] This approach is very convenient for separating, recovering and reusing the fine magnetic TiO_2 particles by applying an external magnetic field.[85,86] It was reported that a direct deposition of TiO_2 onto the surface of magnetic oxide particles led to severe photo-dissolution of the magnetic core. In order to overcome the challenge, addition of silica (SiO_2) layer between the magnetic core and the TiO_2 shell provided magnetic nanoparticles with a chemically inert surface, which inhibited the oxidation of the magnetic core (Fe_3O_4) by the photogenerated VB holes in the outer layer (TiO_2).[87] The synthesis of a multipurpose catalyst (graphene/TiO_2/SiO_2/Fe_3O_4) was reported for the degradation of 2,4-dichlorophenoxyacetic acid (a herbicide). It took the advantages of TiO_2 photocatalysis, graphene (excellent electron transfer ability and high

adsorption capability), Fe_3O_4 (magnetic separation) and SiO_2 (suppressing photo-dissolution of magnetic core). The TiO_2 composite achieved 100% degradation of 2,4-D in 140 min under simulated solar irradiation, while commercial P25 recorded only 33% under same conditions. More so, the composite was highly stable after 8 successive cycles. The photocatalytic activity was dependent on the calcination temperature, magnetic core size and the silica layer content.[88,89]

2.3   Physico-chemical properties of chlorinated phenols

Monochlorophenols and 2,4-DCP are volatile due to their high vapour pressure (**Table 2-3**) and volatilisation may be the major dispersal mechanism of these chemicals into the atmosphere. Trichlorophenols and tetrachlorophenols are slightly volatile.

Table 2-3 Physico-chemical properties of chlorinated phenols.[11]

Compound	Melting point (^{o}C)	Density (gcm^{-3})	Solubility (gL^{-1})/ H$_2$O (25 ^{o}C)	Vapour pressure (mmHg) (25 ^{o}C)	Boiling point (^{o}C)	pKa
2-CP	9.3	1.2634	28.5	0.99	174.9	8.49
4-CP	43.2-43.7	1.2238	27.1	0.23	220	8.85
2,4-DCP	45	1.383	4.5	0.14	210	7.68
2,4,5-TCP	67	1.678	0.948	0.05	235	7.43
2,4,6-TCP	69	1.4901	0.8	0.03	246	7.42
2,3,4,5-TRCP	116-117	1.67	0.166	0.0059	Sublimes	6.96
2,3,4,6-TRCP	70	1.83	0.183	0.0059	64	5.38
2,3,5,6-TRCP	115	1.84	0.1	0.0059	288	5.48
PCP	190	1.987	0.014	0.0002	310	4.74

CP- chlorophenol, DCP- dichlorophenol, TCP- trichlorophenol,

TRCP- tetrachlorophenol and PCP- pentachlorophenol

2.4 Degradation of organic pollutants

The project targets mineralisation of chlorophenols and derivatives by photocatalysis and this section thus made a comprehensive review of the processes involved. Effect of operating variables on the degradation of organic pollutants will be discussed first. Next, a summary on the

degradation of 2,4-dichlorophenol and -trichlorophenol using TiO_2 is presented in **Table 2-4**, while the application of other photocatalysts is presented in **Table 2-5**. The effect of solution pH (optimum pH, 4-5) seems to play an important role in the degradation efficiency of the photocatalytic process. One out of various photocatalytic degradation pathways proposed in literature for 2,4,6-trichlorophenol is shown in **Figure 2-4**.

2.4.1 Effect of light intensity

The UV light intensity of the irradiation source determines the extent of light absorption by the semiconductor catalyst at a given wavelength. This is affected by changing the distance of the light source. Basically, degradation efficiency increases with UV light intensity as the excitation of photocatalyst particles will be enhanced to generate electron-hole pairs. There are three main categories which include, low light intensity (0 – 20 mW cm^{-2}), intermediate light intensity (25 – 50 mW cm^{-2}) and high light intensity (above 100 mW cm^{-2}). It is important to note that both light intensity and the nature of light source don't affect the degradation pathway.[90]

2.4.2 Effect of dissolved oxygen

Dissolved oxygen (DO) plays a significant role as an electron scavenger in TiO_2 photocatalysis. The dissolved oxygen improves the separation of photo-generated electrons and holes as well as the yield of hydroxyl (·OH) radical. It was found that pure oxygen was more effective relative to air for the enhancement of decontamination.[91]

2.4.3 Effect of pollutant concentration

Photocatalysis is a surface reaction initiated by adsorption. It is believed that increased concentration of substrate (pollutant) affects light penetration into the contaminant solution, especially for dyes. In general, the quantity of the substrate adsorbed on the surface of the photocatalyst is of utmost importance. It is evident that only this amount contributes to photocatalytic process and not the one in the bulk of the solution.[92]

2.4.4 Effect of TiO$_2$ dosage

An increase in the catalyst amount (concentration) causes an increase in the number of hydroxyl (·OH) radicals generated. This is due to an increase in the number of active sites on catalyst surface. The initial rates of photoreaction are directly proportional to the mass of catalyst present in the solution. Above optimum dose, the degradation efficiency is limited because of the increase in solution turbidity, aggregation of catalyst particles and blockage of UV radiation.[93]

2.4.5 Effect of solution pH

The pH of contaminant solution determines the surface charge of the photocatalyst and the size of aggregates it forms. Under acidic or alkaline conditions, the surface of TiO$_2$ can be protonated or deprotonated respectively as seen in equations (2-11 and 2-12).

$$TiOH \quad + \quad H^+ \quad \rightarrow \quad TiOH_2^+ \qquad\qquad Eq.(2-11)$$

$$TiOH \quad + \quad OH^- \quad \rightarrow \quad TiO^- \quad + \quad H_2O \qquad Eq.(2-12)$$
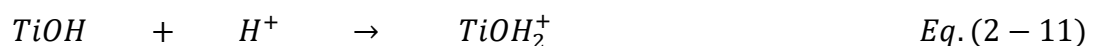
The point of zero charge (PZC) is the pH at which the surface of the catalyst is electrically neutral in solution. The PZC of TiO_2 anatase is within $6.2 – 6.8$, that is, the TiO_2 surface will remain positively charged in acidic medium (pH < PZC) and negatively charged in alkaline medium (pH > PZC). TiO_2 has a higher oxidising activity at lower pH. However, excess H^+ at very low pH can decrease reaction rate.[90]

2.4.6 Effect of H_2O_2

Hydroxyl radical is vital to enhance the photocatalytic degradation activity. H_2O_2 can absorb light energy from UV irradiation and O–O bond is ruptured, leading to the production of activated ·OH radical and the atomic oxygen. Addition of H_2O_2 increases the hydroxyl radical in the reaction mixture which inhibits the electron–hole recombination as seen in the following equations:

$$TiO_2\ (e_{CB}^-)\quad +\quad H_2O_2\quad \rightarrow\quad \cdot OH\quad +\quad OH^-\qquad\qquad Eq.(2-6)$$

$$H_2O_2\quad +\quad hv\quad \rightarrow\quad 2\cdot OH\qquad\qquad Eq.(2-13)$$
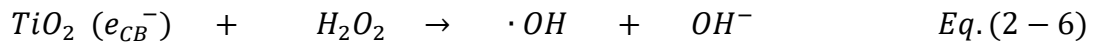
At high H_2O_2 dosage the degradation efficiency decreases due to its hydroxyl radical scavenging effect as shown in equations (2-14 and 2-15).[94]

$$H_2O_2\quad +\quad \cdot OH\quad \rightarrow\quad HO_2^{\cdot}\quad +\quad H_2O\qquad\qquad Eq.(2-14)$$

$$HO_2^{\cdot}\quad +\quad \cdot OH\quad \rightarrow\quad H_2O\quad +\quad O_2\qquad\qquad Eq.(2-15)$$
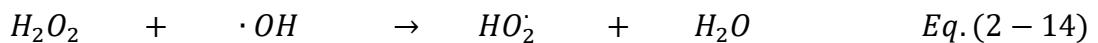
2.4.7 Review on photocatalytic degradation of chlorophenols using TiO$_2$

This section reviews the recent progress (last 10 years) in photocatalytic degradation of chlorophenols in aqueous solution using TiO$_2$ and slurry/suspension batch reactors (**Table 2-4**). These reactions were reported using distilled or de-ionised (D.I.) water as solvent for laboratory simulated wastewater. Various studies show that the rate of degradation of chlorophenols is dependent on, solution pH [90,95–98] and molecular structure-especially the number of substituted Cl groups and their positions on the benzene ring relative to the hydroxyl group.[99–101] It is well known that the initial degradation rate of most organic pollutants with TiO$_2$ and other photocatalysts follows the pseudo-first-order reaction model.[99,102–105]

Rengaraj *et al.* synthesised Ag-doped TiO$_2$ using sol-gel method and evaluated the photocatalytic activity for the degradation of 2,4,6-trichlorophenol under UV-A irradiation (365 nm).[106] It was observed that the Ag dopant effectively increased the photocatalytic activity of the TiO$_2$ (0.5 wt.% optimum Ag loading), due to efficient separation of photogenerated charge carriers (electrons and holes). The electron transfer from the conduction band of TiO$_2$ to silver particles at the interface was reported to be achievable since the Fermi level of TiO$_2$ is higher than that of Ag metal.[107] It was found that the unmodified TiO$_2$ and 0.5 wt.% Ag-TiO$_2$ samples achieved 2,4,6-TCP degradation rates of ~92 and 98% after 40 min and slow mineralisation rates of 66 and 79% total organic carbon (TOC)

removal, respectively after 120 min. In addition, it was found that the 2,4,6-TCP degradation and its dechlorination were faster than its mineralisation.

Vijayan *et al.* prepared Fe-doped TiO_2 using sol-gel method with hydrothermal treatment.[108] A photocatalytic degradation efficiency of 93% was achieved with unmodified TiO_2 in 180 min under UV light irradiation, while the 0.5 wt.% Fe-TiO_2 sample (optimum) recorded ~98% degradation efficiency under same conditions.

Peng *et al.* synthesised a multipurpose photocatalyst, La-doped magnetic TiO_2 (Fe_3O_4/SiO_2/La-TiO_2) using sol-gel method and investigated its photocatalytic activity for 2,4,6-TCP degradation.[109] The magnetic La-TiO_2 exhibited a higher photocatalytic degradation activity (90% in 60 min) compared to magnetic TiO_2 (50%). However, the La-doped magnetic TiO_2 was fairly stable after 7 successive cycles.

Sinirtas *et al.* prepared a binary oxide catalyst (V_2O_5/TiO_2) using solid-state dispersion method and evaluated the photocatalytic activity for 2,4-dichlorophenol degradation under UV-visible light irradiation.[110] Photocatalytic degradation efficiencies of 55, 60, 70 and 85% were achieved in 30 min with TiO_2 (synthesised), commercial TiO_2 (P25), V_2O_5 and V_2O_5/TIO_2, respectively. The effect of surfactant additives (CTAB, HTAB and PVA) on the photocatalytic activity of the binary oxide catalyst was also investigated. Under similar operating conditions, the (V_2O_5/TiO_2/CTAB) sample displayed the highest activity (complete degradation in 30 min), while the samples prepared with HTAB and PVA

recorded degradation efficiencies of ~92 and ~55%, respectively. However, the photochemical stability of $V_2O_5/TiO_2/CTAB$ was not reported.

Table 2-4 Summaries on TiO_2 photocatalysis for the degradation of chlorophenols.

Photocatalyst	Bandgap (eV)	Experimental condition	Performance	Year [Ref.]
$Fe_3O_4/SiO_2/La$-TiO_2 (sol-gel)	Nil	UV-visible light (λ > 340 nm), catalyst dose (2.0 g/L), 2,4,6-TCP concentration (2 mg/L)	90% degradation in 60 min	(2015) [109]
0.5 wt.% Fe-TiO_2 (sol-gel)	2.72 – 3.10	(8 x 8 W) low pressure Hg lamp, cat dose (0.8 g/L), 2,4,6-TCP conc (50 mg/L, pH = 5)	100% degradation and 100% TOC removal in 180 min	(2009) [108]
1 wt.% Fe/TiO_2 (sol-gel)	Nil	UV 20 W lamp (254 nm), catalyst dose (1 g/L), 2,4-DCP conc (15 mg/L, pH = 4)	97% degradation and 71% TOC removal in 120 min	(2012) [98]
$V_2O_5/TiO_2/CTAB$ (Solid state dispersion)	2.21	64-W UV-B lamp, catalyst dose (2 g/L), 2,4-DCP (25 mg/L, pH = 5)	100% degradation and 97% TOC removal in 30 min	(2016) [110]
Sepiolite/TiO_2 (sol-gel)	Nil	360 W UV lamp, cat dose (2 g/L), 2,4-DCP (80 mg/L, pH = 2)	90.9% degradation in 120 min	(2015) [111]

Table 2-4 Summaries on TiO_2 photocatalysis for the degradation of chlorophenols (continued).

Photocatalyst	Bandgap (eV)	Experimental condition	Performance	Year [Ref.]
C/Cl-TiO_2@C_3N_4 NTs	Nil	300 W Xe lamp (λ > 420 nm), catalyst dose (1.0 g/L), PCP concentration (20 mg/L)	100% degradation in 4 h, 75% TOC removal in 18 h	(2016) [112]
N-F-TiO_2 (sol-gel)	Nil	2.2 kW Xe lamp (λ > 290 nm), catalyst dose (0.5 g/L), PCP concentration (5 mg/L, pH_{nat} = 6.7)	100% degradation in 120 min, 85% TOC removal in 240 min	(2015) [113]
TiO_2 (P25)	3.1	500 W Xe lamp (λ > 365 nm), catalyst dose (0.02 g/L), PCP concentration (10 µM)	~90% degradation in 15 min	(2019) [114]
Ag/TiO_2 (photodeposition)	Nil	40 W UV LED (λ = 365 nm), catalyst dose (1.0 g/L), 4-CP concentration (10 mg/L)	90% degradation and 25% TOC removal in 60 min	(2019) [115]
0.21 mol. % Cu-TiO_2 (sol-gel)	Nil	(5 x 7 W) Vis LED (λ = 440 - 490 nm), catalyst dose (3.0 g/L), 2-CP concentration (20 mg/L, pH = 5.5)	100% degradation in 6 h	(2018) [97]

Table 2-4 Summaries on TiO_2 photocatalysis for the degradation of chlorophenols (continued).

Photocatalyst	Bandgap (eV)	Experimental condition	Performance	Year [Ref.]
N-doped mesoporous TiO_2	2.65	Natural sunlight, catalyst dose (0.2% w/v), 2-CP concentration (50 mg/L, pH = 7)	98.6% degradation in 4 h	(2012) [116]
0.5%-Ga,I-TiO_2 (sol-gel)	2.49	400 W Dy lamp (visible light), catalyst dose (1.0 g/L), 2-CP concentration (0.25 mM)	~90% degradation and ~70% TOC removal in 4 h	(2011) [117]
S-TiO_2 (sol-gel)	2.47	Visible light LED (λ = 490, 565 & 660 nm), catalyst dose (1.0 g/L), 2-CP concentration (25 mg/L)	71.4%, 71.5% and 86.7% degradation, respectively in 180 min	(2015) [118]
TiO_2–RGO–CoO (sol-gel)	2.83	200 W Xe lamp (visible light), catalyst dose (0.5 g/L), 2-CP concentration (10 mg/L, pH = 6)	98.2% degradation in 8 h	(2016) [119]
N-In-Sn-TiO_2 (sol-gel)	3.10	UV and visible light (λ > 400 nm), catalyst dose (0.125 and 0.25 g/L), 4-CP conc (50 µM, pH = 5.38)	96% degradation in 1 h (UV), 90.7% degradation in 8 h (Vis)	(2018) [120]

Table 2-4 Summaries on TiO_2 photocatalysis for the degradation of chlorophenols (continued).

Photocatalyst	Bandgap (eV)	Experimental condition	Performance	Year [Ref.]
8.0 wt.% B-TiO_2 (sol-gel)	2.89	(18 x 8 W) UV-A lamp and (2 X 150 W) visible light (λ > 400 nm), cat dose (1.0 g/L), 2,4-DCP (20 mg/L, pH = 6.5)	90% degradation in 5 h (UV), 75% degradation in 5 h (Vis)	(2017) [121]
I/TiO_2 –T (5/2) n(Ti)/n(I) ratio of 5/2 (lignin as template, T)	3.16	350 W Xe lamp (λ > 400 nm), catalyst dose (0.5 g/L), 4-CP concentration (50 mg/L)	100% degradation in 60 min, ~90% TOC removal in 100 min	(2019) [122]
0.5 wt.% Co-TiO_2 (sol-gel)	2.1	18 W low pressure Hg lamp (λ = 254 nm), catalyst dose (1.0 g/L), chlorophenols (400 mg/L, pH = 5)	2-CP (80%), 4-CP (100%), 2,6-DCP (45%), 2,4-DCP (70%) and 2,4,6-TCP (90%) degradation in 180 min	(2014) [99]
CdS@TiO_2	2.25	Mic-LED-455 (visible light), catalyst dose (1.0 g/L), CPs (10 mg/L)	2,4-DCP (73.8%) and 2,4,6-TCP (77%) degradation in 360 min	(2019) [123]
Fe_3O_4@TiO_2@Au	Nil	150 W Xe lamp (UV–vis light), catalyst dose (0.5 g/L), 2,4,6-TCP concentration (7.5×10^{-5} M, pH = 10)	97.7% degradation in 40 min	(2019) [124]

Table 2-4 Summaries on TiO_2 photocatalysis for the degradation of chlorophenols (continued).

Photocatalyst	Bandgap (eV)	Experimental condition	Performance	Year [Ref.]
2 wt.% CuS/TiO_2	2.73	125 W Hg lamp (λ = 365 nm), 4-CP (20 mg/L, 60 mL)	87% degradation in 150 min	(2016) [125]
M/TiO_2 (M = CoPc, ZnPc)	2.67 – 2.78	128 W Lightex LT50 lamp (visible light), cat dose (1.0 g/L), 4-CP (0.013 M, pH = 7)	~100% degradation in 30 min	(2016) [126]
1 wt.% M-TiO_2 (M = Fe, Cu, Ni)	2.5 – 3.4	(4 x 15 W) UV lamp (λ = 365 nm), cat dose (2.0 g/L), 4-CP (10 mg/L)	Ni (90%, 80%), Cu (90%, 73%), Fe (37%, 31%) degradation and TOC removal, respectively in 6 h	(2019) [102]
Y_2O_3/TiO_2 nanosheets	2.92 – 3.20	Natural sunlight, catalyst dose (1.0 g/L), 4-CP (20 mg/L)	98% degradation and 67.6% TOC removal in 120 min	(2017) [127]
TiO_2(R)-CuOx (0.12 wt.% Cu) and TiO2(R)-FeOx (0.13 wt.% Fe)	3.0	150 W Xe lamp (λ > 320 nm), catalyst dose (1.0 g/L), 4-CP (2.5 x 10^{-4} M)	~80% and ~55% degradation in 180 min with CuOx and FeOx, respectively	(2014) [128]

Table 2-4 Summaries on TiO_2 photocatalysis for the degradation of chlorophenols (continued).

Photocatalyst	Bandgap (eV)	Experimental condition	Performance	Year [Ref.]
7 wt.% (Fe_2O_3, Co_3O_4 and CuO) loaded $ZnTiO_3$–TiO_2	2.82 – 3.12	Natural sunlight, 0.3 mL H_2O_2, cat dose (2.0 g/L), 4-CP conc (25 mg/L, pH = 5)	100, 76 and 85% degradation in 45 min with Fe_2O_3, Co_3O_4 and CuO, respectively	(2016) [129]
20 wt.% ZnO–TiO_2 mixed oxide	2.82	16 W UV-B lamp, cat dose (2.0 g/L), 4-CP conc (25 mg/L, pH = 5.2)	100% degradation and 91% TOC removal in 75 min	(2014) [130]
Fe-TiO_2-Ag nano-sphere (0.3 wt.% Fe and 2.0 wt.% Ag)	Nil	(2 x 8 W) UV-C lamp, catalyst dose (1.5 g/L), 4-CP conc (40.4 mg/L, pH = 4.86)	97% degradation in 165 min	(2017) [131]
10 wt.% GO–TiO_2 (titanate nanotubes)	2.8	UV lamp (λ = 254 nm), catalyst dose (1.0 g/L), 4-CP conc (50 mg/L)	65% degradation in 175 min	(2019) [132]
Magnetic TiO_2/FeOx/POM	2.65	Simulated solar light, catalyst dose (0.5 g/L), 2,4-DCP concentration (10 mg/L, pH = 5)	76% degradation and 55.9% TOC removal in 180 min	(2019) [133]

Table 2-4 Summaries on TiO_2 photocatalysis for the degradation of chlorophenols (continued).

Photocatalyst	Bandgap (eV)	Experimental condition	Performance	Year [Ref.]
TiO_2 – 325 mesh	3.2	Medium pressure Hg lamp ($\lambda > 360$ nm), cat dose (0.5 g/L), 4-CP (10 µM), 2,6-DCP (20 µM)	100% 4-CP degradation in 30 min and 100% 2,6-DCP degradation in 60 min	(2012) [134]
FeOOH/TiO_2 (0.14 wt.% Fe)	3.2	300 W Xe lamp ($\lambda > 320$ nm), catalyst dose (0.5 g/L), 2,4,6-TCP concentration (50 mg/L, $pH_{nat} = 6$)	100% degradation and 85% TOC removal in 240 min	(2020) [135] This work
FeOx-CoOx/TiO_2 (0.1 wt.% Fe and 0.1 wt.% Co)	3.2	300 W Xe lamp ($\lambda > 320$ nm), catalyst dose (0.5 g/L), 2,4,6-TCP concentration (50 mg/L, $pH_{nat} = 6$)	100% degradation and 92% TOC removal in 180 min	This work

CTAB: cetyltrimethylammonium bromide, HTAB: hexadecyltrimethylammonium bromide, PVA: polyvinyl acetate, NTs: nanotubes, RGO: reduced graphene oxide, Pc: phthalocyanine, GO: graphene oxide, POM: poly-oxo-tungstate, LED: light emitting diode, CP: chlorophenol, DCP: dichlorophenol, TCP: trichlorophenol, PCP: pentachlorophenol, TOC: total organic carbon, pH_{nat}: natural pH.

2.5 Summary

In summary, by comparing the activities of the reviewed optimised photocatalysts, relative to their pristine TiO_2 counterparts in **Table 2-4**, TiO_2 heterojunction nanocomposites performed better than metal-doped TiO_2 nanocomposites under UV light irradiation. This is likely due to better charge separation efficiency on surface of TiO_2 heterojunction nanocomposites, as dopant ions in TiO_2 lattice can act as charge recombination centres in metal-doped TiO_2. Also, the modification of TiO_2 with an adsorbent greatly improved its photocatalytic degradation efficiency by increasing surface contact with the water contaminant.

However, photocatalyst stability and mineralisation efficiency are some of the present-day challenges encountered during water decontamination. In **Table 2-4**, the mineralisation efficiencies based on TOC analysis were either not thoroughly reported or very moderate, especially for 2,4,6-TCP. The TOC measurement is very important in confirming the complete transformation of the chlorophenols to carbon dioxide, instead of partial oxidation to other organic compounds, which may be more toxic or undetected during quantitative measurements. Photocatalyst stability test was not thoroughly reported in some cases. Some of the reviewed photocatalysts displayed very slow chlorophenol mineralisation efficiencies compared to degradation efficiencies. Also, some of the reviewed photocatalysts contain rare earth elements, expensive metals or toxic metals, which may impede their commercialisation. The project aims to

proffer a solution, by using low-cost methods in preparing robust and stable TiO_2 nanocomposites, containing earth-abundant metals as cocatalyst, with high herbicide mineralisation efficiency.

In the project, the optimised $FeOOH/TiO_2$ (0.14 wt.% Fe) sample achieved nearly a two-fold enhancement in photocatalytic activity, compared to pristine TiO_2, towards the complete mineralisation of 2,4,6-TCP under UV light irradiation (λ > 320 nm). Photoluminescence (PL) measurements confirmed the enhanced photo-generated electron-hole separation, while in situ electron spin resonance (ESR) measurements confirmed the catalytic effect of FeOOH for improved generation of hydroxyl radicals, thus led to high photocatalytic activity.

 Further optimisation of the photocatalytic activity of $FeOOH/TiO_2$ was achieved using bimetallic cocatalyst decoration of TiO_2 surface. The optimised $FeOx$-$CoOx/TiO_2$ (0.1 wt.% Fe and 0.1 wt.% Co) nanocomposite achieved nearly a 50% enhancement in photocatalytic activity, compared to $FeOOH/TiO_2$, towards the complete mineralisation of 2,4,6-trichlorophenol, under similar operating conditions. The outstanding photocatalytic performance of optimised $FeOx$-$CoOx/TiO_2$ sample for herbicides mineralisation was due to an increased charge separation and enhanced hydroxyl radicals production monitored by diverse spectroscopies.

The optimised $FeOOH/TiO_2$ and $FeOx$-$CoOx/TiO_2$ samples achieved TiO_2 enhancement factors of 2 and 2.5, respectively compared to unmodified TiO_2 for TOC removal during 2,4,6-TCP mineralisation. However, only one

TiO_2-based photocatalyst, metal-doped TiO_2 (0.5 wt.% Fe-TiO_2) in **Table 2-4** was reported in literature, with available TOC removal data, for 2,4,6-TCP mineralisation.[108] About 92% and 100% TOC removal were achieved in 180 min using TiO_2 and 0.5 wt.% Fe-TiO_2, respectively. The reported 0.5 wt.% Fe-TiO_2 photocatalyst achieved a TiO_2 enhancement factor of ~ 1.1 throughout the duration of 2,4,6-TCP mineralisation.

TCP – trichlorophenol, DCQ – dichlorobenzoquinone, DCHQ – dichlorohydroquinone, DCHB – dichlorohydroxybenzoquinone, DCC – dichlorocatechol, TRCP – tetrachlorophenol

Figure 2-4 Typical degradation pathway for 2,4,6-TCP. Adapted from Ji et al.[136] Copyright 2013, Elsevier. Reprinted with permission.

Compared to other photocatalysts, TiO_2 remains the best for the commercialisation of photocatalytic water treatment technology because of its relative low toxicity, low-cost and high photochemical stability. Due to the aforementioned drawbacks of reported TiO_2 photocatalysts for the degradation of chlorinated phenols, extensive research is still required to develop a cheap, non-toxic, visible-light active, photo-chemically stable and highly efficient TiO_2-based composite for wastewater purification.

3   Methodology

This chapter presents only the characterisation methods used throughout the research and the other specific methods will be defined in the following chapters.

3.1   X-ray diffraction

In X-ray powder diffractometry, X-rays are generated within a sealed tube that is under vacuum. A current is applied that heats a filament within the tube; the higher the current the greater the number of electrons emitted from the filament. This generation of electrons is analogous to the production of electrons in a television picture tube. A high voltage, typically 15-60 kilovolts, is applied within the tube. This high voltage accelerates the electrons, which then hit a target, commonly made of copper. When these electrons hit the target, X-rays are produced. The wavelength of these X-rays is characteristic of that target. These X-rays are collimated and directed onto the sample, which has been ground to a fine powder (typically to produce particle sizes of less than 10 microns). A detector detects the X-ray signal; the signal is then processed either by a microprocessor or electronically, converting the signal to a count rate. Changing the angle between the X-ray source, the sample, and the detector at a controlled rate between pre-set limits is an X-ray scan.[137,138]

The diffraction pattern exhibited by a crystal is explained using Bragg's law (equation 3-1). The law states that when the X-ray is incident onto a crystal

surface, its angle of incidence, θ will reflect with a same angle of scattering, θ. And, when the path difference, d is equal to a whole number, n of wavelength, a constructive interference will occur.
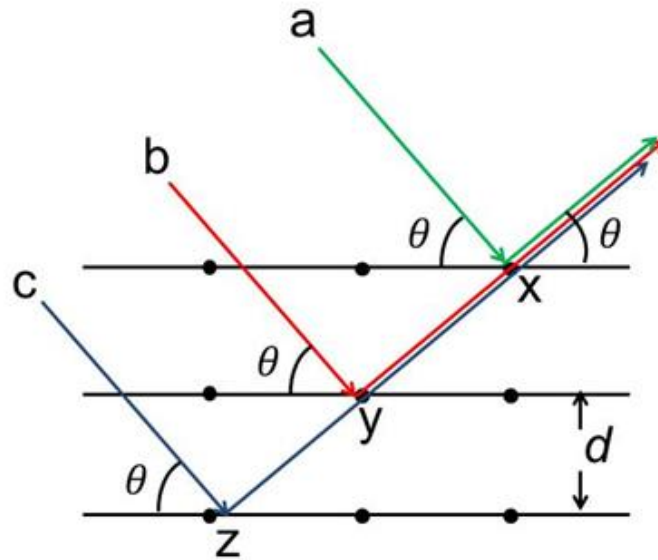
Figure 3-1 X-ray scattering on a crystal surface.

$$n\lambda \ = \ 2d sin\theta \qquad\qquad Eq.\,(3-1)$$

Where,

- λ = the wavelength of the X-ray

- d = the spacing of the crystal layers (path difference)

- θ = the incident angle (the angle between incident ray and the scatter plane)

- n = an integer

In the project, measurements were performed using a STOE StadiP (Germany) diffractometer with a range from $2\theta = 2 - 40^o$ in transmission geometry and Mo kα radiation (λ = 0.071 nm, 50 kV, 30 mA) and a Bruker D4 (Germany) diffractometer with a range from $2\theta = 10 - 80^o$ in reflection geometry and Cu kα radiation (λ = 0.154 nm, 40 kV, 30 mA).

3.2   X-ray Photoelectron Spectroscopy

X-ray photoelectron spectroscopy (XPS) is a surface-sensitive quantitative spectroscopic technique that measures the elemental composition at the parts per thousand range, empirical formula, chemical state and electronic state of the elements that exist within a material. XPS spectra are obtained by irradiating a material with a beam of X-rays, while simultaneously measuring the kinetic energy and number of electrons that escape from the top 0 to 10 nm of the material being analysed. XPS requires a high vacuum (P ~ 10^{-8} millibar) or ultra-high vacuum (UHV; P < 10^{-9} millibar) condition.[138–140]

The binding energy (E_b) of the core level and kinetic energy of the detected electron (E_{KE}) are related by the following equation:

$$E_b = E_\gamma - (E_{KE} + \emptyset) \qquad\qquad Eq.\,(3-2)$$

Where, E_γ is the energy of the incident X-ray photons and $\emptyset$ is the work function of the instrument.

To count the number of electrons during the acquisition of a spectrum with a minimum of error, XPS detectors must be operated under ultra-high vacuum

(UHV) conditions because electron counting detectors in XPS instruments are typically one meter away from the material irradiated with X-rays. This long path length for detection requires such low pressures.[141]

In the project, measurements were performed on a Thermo Scientific K-alpha (USA) spectrometer using monochromatic Al kα radiation. The results were analysed using Casa XPS software.

3.3   Raman Spectroscopy

Raman spectroscopy is a spectroscopic technique used to observe vibrational, rotational, and other low-frequency modes in a system. Raman spectroscopy is commonly used in chemistry, to provide a fingerprint by which molecules can be identified, as vibrational information is specific to the chemical bonds and symmetry of molecules. It relies on inelastic scattering, or Raman scattering of monochromatic light, usually from a laser in the visible, near infrared, or near ultraviolet range. The laser light interacts with molecular vibrations, phonons or other excitations in the system, resulting in the energy of the laser photons being shifted up or down.[142]

The shift in energy gives information about the vibrational modes in the system. Infrared (IR) spectroscopy yields similar, but complementary information. Raman shifts are typically reported in wavenumbers, which have units of inverse wavelength, as this value is directly related to energy.[142]

$$\Delta w \; = \; \left[\frac{1}{\lambda_o} \; - \; \frac{1}{\lambda_1} \right] \qquad\qquad Eq.\,(3-3)$$

Where,

- Δw = Raman shift expressed in wavenumber (cm^{-1})

- λ_o = excitation wavelength

- λ_1 = Raman spectrum wavelength

In the project, measurements were performed on a Renishaw InVia (UK) Raman microscope, using 325 nm or 514 nm excitation laser beams and the wavenumber range was from 100 to 3500 cm^{-1}.

3.4   Photoluminescence spectroscopy

Photoluminescence (PL) spectroscopy is a contactless, non-destructive method of probing the electronic structure of materials. Light is directed onto a sample, where it is absorbed and imparts excess energy into the material in a process called photo-excitation. One way this excess energy can be dissipated by the sample is through the emission of light, or luminescence. In the case of photo-excitation, this luminescence is called PL. With respect to photocatalysis, the quantity of PL emitted from a material is directly related to the relative amount of radiative and non-radiative recombination rates of photo-generated electrons and holes.[143,144]

In the project, measurements were performed on a Renishaw InVia (UK) Raman microscope, using 325 nm excitation laser beam and the wavelength range was from 200 to 800 nm.

3.5   BET Surface Area Analysis

The Brunauer–Emmett–Teller (BET) is a non-destructive technique that measures the specific surface area and pore size distribution of a powdered sample based on gas adsorption. Generally, the powdered samples are degassed at a moderate temperature (~ 120 ^{o}C) overnight to remove adsorbed contaminants from the surface and pores of a sample prior to BET analysis.   The analyser collects the nitrogen (N_2) gas adsorption/desorption isotherms at 77 K. The BET equation describes the physical adsorption of gas molecules on a solid surface to calculate the specific surface area (m^2/g). More so, the BET theory follows the Langmuir isotherm for multilayer adsorption of adsorbate on the surface of an adsorbent. A non-corrosive gas like nitrogen is usually employed as an adsorbate, because it is readily available in high purity, has relatively strong gas-solid interaction and has a widely accepted cross section area (16.2 $Å^2$).[145,146]

In the project, BET measurements were performed on a Micromeritics TriStar 3000 (USA) gas adsorption analyser with N_2 gas as the adsorbate.

3.6   Microscopes (SEM, TEM)

Scanning electron microscopy (SEM) and transmission electron microscopy (TEM) are two different techniques used for imaging the microstructure and morphology of materials. SEM applies a focused beam of high-energy electrons to generate a variety of signals at the surface of solid samples. The signals that are generated from electron-sample interactions reveal information about the size of particles, surface morphology and orientation

of materials making up the sample. In most applications, data are collected over a selected area of the surface of the sample, and a 2-dimensional image is generated that displays spatial variations in these properties.[147,148] TEM involves the transmission of an electron beam through a thin sample (< 100 nm). The beam interacts with the sample and refracts around atoms, generating an image on a photographic film.[149]

In the project, SEM measurements were performed on JEOL JSM-7401F (Japan) microscope. The powder samples were loaded on carbon tips with gold coating. A JEOL 2010F (Japan) microscope was used for TEM measurements. The powder samples were diluted in chloroform, sonicated to give a uniform suspension and few droplets transferred onto a conductive copper grid.

3.7   UV-visible spectroscopy

The UV-vis spectroscopy (ultraviolet-visible spectroscopy), also known as electronic absorption spectroscopy, is based on the measurement of the light absorbed due to electronic transitions in a sample around 190 to 800 nm wavelength range. Different molecules exhibit different energy transitions depending on their chromophores. A chromophore is a covalently unsaturated group responsible for electronic absorption or any group of atoms that absorbs light, whether a colour is thereby produced or not. The technique has been widely used for the identification and quantification of organic compounds. UV-vis absorption spectra will give data where the wavelength is on the abscissa and absorbance (A) on the ordinate.[138,150]

A linear relationship between absorbance and concentration of a solution is expressed by Beer Lambert's law, which states that the absorption of light in a sample solution is dependent on the concentration c of the dissolved molecule, the specific molar extinction coefficient at a defined wavelength λ and the path length d. It is stated mathematically in equation (3-4) below.

$$A = -logT = log\frac{I_o}{I} = \varepsilon.\text{c}.\text{d} \qquad\qquad Eq.(3-4)$$

Where,

A = absorbance, T = transmittance

I_o = intensity of incident light, I = intensity of transmitted light

ε = molar extinction coefficient (L mol^{-1} cm^{-1})

c = concentration (mol L^{-1}) and d = cuvette/cell path length   (cm)

$$\% \; degradation \; = \; 100 \; x \; \frac{C_o \; - \; C_t}{C_o} \qquad\qquad Eq.(3-5)$$

Where,

- C_o = initial concentration of water pollutant

- C_t = remaining concentration of water pollutant after time, t

In the project, UV-vis spectra measurements were performed on a Shimadzu UV-2550 (Japan) spectrophotometer. A calibration curve was plotted using various concentrations of tested solutions, prepared within the

working range (absorbance ≤ 1) before further measurements. When the Beer-Lambert law is valid, this calibration curve is linear.

3.8 Diffuse Reflectance Spectroscopy (DRS)

UV-vis diffuse reflectance spectroscopy is used to investigate the optical properties of semiconductors in the solid state. The semiconductors usually have band gap energies between 1 to 4 eV, which refers to the band absorption around 1200 to 300 nm. A UV-vis DRS spectra will give data where the wavelength is on the abscissa and reflectance (R) on the ordinate.[149,151]

The absorption coefficient F(R) can be calculated using the following Kubelka-Munk equation:

$$F(R) = \frac{(1-R)^2}{2R} \qquad\qquad Eq.(3-6)$$

The indirect bandgap is then estimated from the intercept of the linear portion of the plot using equation (3-7).

$$E_g = \frac{hc}{\lambda} \rightarrow h\nu = \frac{1240}{\lambda} \qquad\qquad Eq.(3-7)$$

For a direct bandgap, semi-conductor, the absorption near the band edge can be estimated from equation (3-8), known as the Tauc plot.

$$(\alpha h\nu) = C\left(h\nu - E_g\right)^n \qquad\qquad Eq.(3-8)$$

Where, C is a constant, E_g the optical bandgap, α is the optical absorption coefficient, hv is the photon energy, h the Plank's constant, v the frequency of light and the exponent n characterises the nature of band transition; the values of n = 1/2 and 3/2 correspond to direct allowed and direct forbidden transitions, respectively.

In the case of direct allowed band gap of a semi-conductor, the relation becomes:

$$(\alpha h v)^2 \; = \; C\big(h v \; - \; E_g\big) \hspace{4cm} Eq.\,(3-9)$$

An extrapolation of the linear region of a plot of $(\alpha hv)^2$ on the Y-axis versus photon energy (hv) on the X-axis gives the value of the optical band gap.

In the project, the UV-vis absorption spectra measurements of powdered samples were performed on a Shimadzu UV-2550 (Japan) spectrophotometer fitted with an integrating sphere. $BaSO_4$ powder was used as a reflectance standard ($\geq$ 98% reflectance) within the UV-vis wavelength range (200 – 800 nm). UV-Probe software was used to directly convert reflectance to absorbance via the Kubelka-Munk transformation.

3.9   TOC-L Analysis

Total organic carbon- liquid (TOC-L) analyser is used to quantify the amount of organic carbon present in an aqueous solution. The sample is delivered to the combustion furnace, which is supplied with purified air. There, it undergoes combustion through heating to 680 °C with a platinum catalyst. It decomposes and is converted to carbon dioxide. The carbon dioxide

generated is cooled and dehumidified, and then detected by the infrared gas analyser (NDIR).[152]

In environmental water and other samples in which the inorganic carbon (IC) component of the total carbon (TC) is extremely large, the organic carbon in the sample is usually measured via a non-purgeable organic carbon (NPOC) measurement as shown in **Figure 3-2**. By adding a small amount of acid to the sample, followed by bubbling of a chemically inert gas, such as nitrogen, argon, or helium, through the sample (sparging), to remove dissolved gases, the IC (e.g. bicarbonate and carbonate ions) in the sample is converted to carbon dioxide. This carbon dioxide is removed, and the TOC is obtained by measuring the TC in the treated sample. When the carbon dioxide from the IC is removed, purgeable organic carbon (POC) may also be lost. Accordingly, the TOC obtained with this method may be referred to as NPOC.[152]
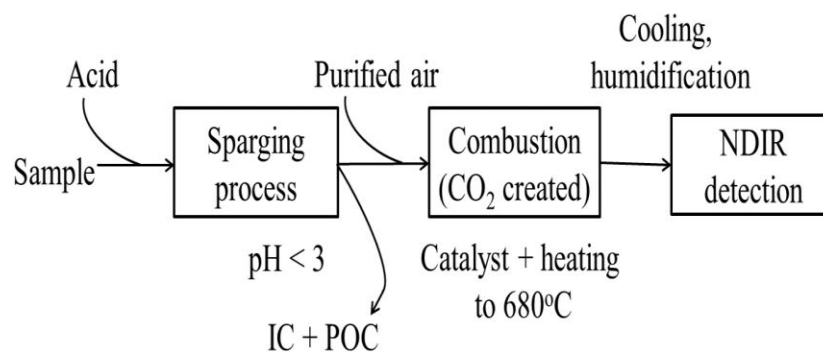
Figure 3-2 A typical sketch illustrating TOC-L analyser (Shimadzu) NPOC measurement.[152]

$$\% \, mineralisation \; = \; 100 \; x \; \frac{TOC_o \; - \; TOC_t}{TOC_o} \qquad\qquad Eq. \, (3-10)$$

Where,

- TOC_o = initial concentration of organic carbon in water pollutant

- TOC_t = remaining concentration of organic carbon after time, t

In the project, TOC measurements of liquid samples were obtained from a Shimadzu TOC-L CPH (Japan) analyser after calibration with potassium hydrogen phthalate (KHP) as a primary standard. In the laboratory simulated wastewater prepared using D.I. water, the IC component of the TC is negligible, thus the use of an acid and inert gas bubbling in the sparging process were excluded from the NPOC measurement.

3.10 Electron Spin Resonance

Electron spin resonance (ESR), or also known as electron paramagnetic resonance (EPR), is a powerful non-destructive analytical method for the detection and characterisation of unpaired electrons in a substance. ESR spectroscopy involves the absorption of microwave radiation by an unpaired electron when it is exposed to a strong magnetic field. Species that contain unpaired electrons (e.g. free radicals, odd-electron molecules, transition metal complexes and rare earth ions) can therefore be detected by ESR.[153,154]

In the project, in situ ESR spectra measurements were performed on a bench-top Magnettech MS-5000 (Germany) ESR spectrometer, using 10 mW microwave power, 10 kHz modulation frequency and magnetic field range from 326.7 to 346.7 mT. A 300 W Xe lamp was used as light source

(λ > 320 nm). In situ ESR signals of radical species ($\bullet OH$ and $\bullet O_2^-$) generated during photocatalytic water treatment were measured using a spin-trapping agent, DMPO (5,5'-dimethyl-1-pyrroline-N-oxide) in the absence of herbicide. Aqueous dispersion of DMPO and photocatalyst was used for $\cdot OH$ radical detection, while methanol dispersion of DMPO and photocatalyst was used for $\cdot O_2^-$ detection.[155]

3.11 Fluorescence spectroscopy

Fluorescence spectroscopy is a sensitive analytical technique used for the characterisation of molecular constituents (fluorescent molecules or fluorophores) present in a sample. It is a type of electromagnetic spectroscopy, which involves the excitation of electrons from the fluorescent molecules upon collision with a high energy photon. During the transition process of fluorophores from their higher energy level (excited state) to the ground state by lowering their energy level, photons are emitted. In order to separate the fluorescence produced by the sample and the transmitted light, the fluorescence detector is placed at an angle of 90° to the incident light direction, thus a four-sided transmission cell (quartz cuvette) is used. To obtain a spectrum, the fluorescence is dispersed using a diffraction grating.[156,157]

In the project, spectrofluorometric measurements were performed on Shimadzu RF-6000 (Japan) spectrofluorometer, with a xenon arc lamp installed as light source, and a fluorescence detector capable of measurements between 200 and 900 nm. Terephthalic acid and coumarin

are the two widely used probe molecules, for the detection and quantification of •OH radicals, due to their high reactivity with •OH to produce highly fluorescent products.[158,159] Coumarin was used as a probe molecule to quantify the hydroxyl radicals generated in the photocatalytic water treatment set-up. Coumarin reacts with •OH radicals to give a highly fluorescent adduct (7-hydroxycoumarin). The excitation wavelength was set at 332 nm and the emission wavelength range between 340 and 600 nm.[158]

3.12 Liquid chromatography and Mass spectrometry

Liquid chromatography (LC) is an analytical technique used for the separation and analysis of individual components of a liquid mixture. The process involves mass transfer of a sample through a polar mobile phase (mostly methanol or acetonitrile) and non-polar stationary phase. The stationary phase consists of a porous granular solid material such as silica or polymers filled in a packed column made of metal. The interaction between mobile phase and stationary phase is the basis for column separation of the individual components and elution at a different time. The retention time is the time from the start of sample injection to detector response. The unknown compound can be characterised by comparing the retention time with that of a known standard under the same conditions.[160,161]

In the project, two types of detectors are utilised, which are Photodiode array detector (PDA) and Mass spectrometry detector (MS). The PDA detector is equipped with a linear array of discrete photodiodes on an

integrated circuit chip. It can scan a wavelength range from 190-800 nm, unlike the conventional single wavelength UV/vis detector. Array detectors are especially useful for recording the full uv-vis absorption spectra of samples that are rapidly passing through a sample flow cell. UV/vis detectors visualise the obtained result in two dimensions (light intensity and time), but PDA adds the third dimension (wavelength). This is convenient to determine the most suitable wavelength without repeating analyses.[160]

In the project, the change in herbicide concentration was monitored using a high performance liquid chromatograph (Shimadzu LC-2030C, Japan) consisting of a binary pump, an autosampler, a PDA detector and an ACE-5 C18 (5µm × 150 mm × 4.6 mm) reverse phase column maintained at 40 $^{\circ}$C. The HPLC used a 5–95% gradient (Acetonitrile/H_2O with 0.1% formic acid) as the mobile phase.

Before the emergence of electrospray ionisation mass spectrometry (ESI-MS), there were several ionisation methods (electron ionisation, chemical ionisation, etc.), but the propensity of analyte to fragment was a challenge. ESI-MS is a soft ionisation technique used for the generation of gaseous ions without fragmentation of thermally unstable large molecules such as proteins. In positive ion mode (when the spraying nozzle is kept at positive potential) the charging generally occurs via protonation, while in negative ion mode (when the spraying nozzle is kept at negative potential) the charging generally occurs via deprotonation.[162]

In the project, intermediate products formed during herbicide mineralisation were detected using HPLC with a single quadrupole tandem mass spectrometer (Shimadzu 2020 series, Japan, HPLC-MS system), equipped with an ESI source. The MS detection was operated in negative ionisation mode.

4 Highly dispersed FeOOH to enhance photocatalytic activity of TiO$_2$ for complete mineralisation of herbicides

4.1 Introduction

This chapter presents the synthesis of novel nanocomposites comprising different phases of Fe(III) species on PC50 (commercial anatase TiO$_2$), using a reproducible surface impregnation method. The active species of Fe$_4$NO$_3$(OH)$_{11}$, FeOOH and Fe$_2$O$_3$ were found to be readily controlled by synthesis temperature. The Fe(III) species were thoroughly characterised in order to clarify their functionality and actual active species. The mineralisation of 2,4,6-trichlorophenol (2,4,6-TCP) in water was carried out under UV/Vis light irradiation. The effects of cocatalyst concentration, choice of Fe(III) precursor and calcination temperature were investigated. The charge transfer mechanism and the reaction pathway were also discussed. Photocatalytic mineralisation ability of the optimised catalyst was also evaluated with another widely used herbicide, 2,4-dichlorophenoxyacetic acid (2,4-D) to demonstrate its wide feasibility. Due to its remarkable photocatalytic activity, only the optimised FeOOH/TiO$_2$ nanocomposite with 0.14 wt.% Fe loading and 250 $^{\circ}$C calcination temperature was comprehensively characterised.

4.2   Experimental section

4.2.1   Chemicals

PC50 TiO_2 (purely anatase) was purchased from Millennium chemicals. 2,4,6-trichlorophenol (98%) was purchased from Alfa Aesar. 2,4-dichlorophenoxyacetic acid was purchased from Cayman Chemical Company. 1,4-benzoquinone (99%) was purchased from Acros Organics. $Fe(NO_3)_3.9H_2O$, $FeCl_3.6H_2O$, $Fe_2(SO_4)_3.H_2O$, Ethylenediaminetetraacetic acid (EDTA) and DMPO were purchased from Sigma-Aldrich. Isopropanol (HPLC grade), Potassium hydrogen phthalate (KHP) and Acetonitrile (HPLC grade) were purchased from Fischer Scientific. All reagents were used as received without further purification.

4.2.2   Fabrication of photocatalysts

A modified surface impregnation and drying technique was used to fabricate $FeOOH/TiO_2$ and Fe_2O_3/TiO_2 composites.[128] In the experiment, the appropriate percentage weight of iron (III) nitrate nonahydrate was added to an aqueous suspension of 1.0 g of commercial PC50 TiO_2 in a clean alumina crucible under mild stirring, with Fe/TiO_2 composition range (0.07 to 2.8 wt.% Fe).[128] The obtained slurry was continuously stirred with a magnetic stirrer bar and dried slowly at 80 ^{o}C on a hotplate. The resultant dried powder was hand-milled and calcined in a muffle furnace under air atmosphere at 250 ^{o}C for 4 hours during study on effect of Fe loading on photocatalytic activity. The sample prepared at this temperature was denoted as $FeOOH/TiO_2$ as proved by XRD and Raman characterisations. It

was collected after cooling down to room temperature, hand-ground again and stored for photocatalytic activity tests and characterisations. Subsequent study on the choice of Fe(III) precursor (nitrate, sulphate and chloride) was evaluated using optimum Fe loading (0.14 wt.%), followed by a study on the effect of calcination temperature (120 to 450 ^{o}C).

4.2.3 Characterisation

High resolution XPS was performed using a Thermo Scientific K-alpha photoelectron spectrometer with monochromatic Al kα radiation; peak positions were calibrated to carbon (C1s = 284.5 eV) and plotted using the CasaXPS software. Powder XRD measurements were performed using a STOE StadiP diffractometer in foil mode with Mo kα radiation (λ = 0.071 nm, 50 kV, 30 mA) and a Bruker D4 diffractometer in reflection geometry with Cu kα radiation (λ = 0.154 nm, 40 kV, 30 mA). Specific surface area (S.A) measurements were performed using the BET method (N_2 adsorption, TriStar 3000, Micrometrics). The morphologies of the products were characterised using TEM (JEOL 2010F) with EDS detector. Raman scattering and PL were measured using a Renishaw 1000 Raman microscope with 514 nm and 325 nm excitation lasers at room temperature, respectively. In situ ESR signals of radicals trapped by DMPO were obtained using MS-5000 Magnettech ESR spectrometer.

4.2.4 Photocatalytic activity test

A 300 W Xe lamp (Newport) was used as the light source with a plain glass window (λ > 320 nm) as a cut-off filter. The glass window shields all UV light

with wavelength < 320 nm. In the photocatalysis experiment, 0.1 g of photocatalyst was suspended in 200 mL 50 mg/L aqueous solution of 2,4,6-trichlorophenol (2,4,6-TCP) at natural solution pH of 6 or 200 mL 25 mg/L aqueous solution of 2,4-dichlorophenoxyacetic acid (2,4-D) at natural solution pH of 4 in D.I. water. The suspension was sonicated in an ultrasonic water-bath for 15 min and then magnetically stirred in the dark for 1 h to achieve adsorption/desorption equilibrium of herbicides on the photocatalyst before photocatalysis. The photocatalyst had negligible effect on the overall pH of the suspension before photocatalysis. The experimental setup is shown in **Fig. 4-1**.
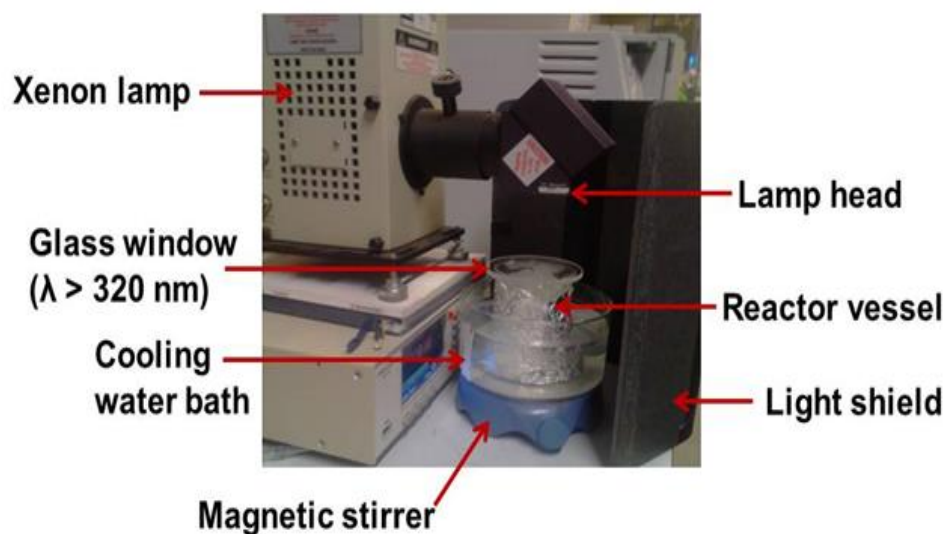
Figure 4-1 Reactor set-up used for photocatalytic mineralisation of herbicides.

The suspension was then exposed to light irradiation ($\lambda > 320$ nm) for 4 h, under continuous magnetic stirring, and the reaction vessel was immersed in a water-bath to regulate temperature (T $\leq$ 30 ^{o}C). The distance between the lamp head and the top of the solution was maintained at 8 cm to achieve similar light intensities. Upon light irradiation, 3 mL aliquot was withdrawn from the bottom of the suspension at regular time intervals and filtered through a micropore syringe filter (PTFE, 0.2 μm) before further analysis.

Similar experimental setup was used in the control tests (photolysis and dark adsorption) for 4 h. However, photolysis of 2,4,6-TCP and 2,4-D were carried out without photocatalyst and sonication, while dark adsorption of 2,4,6-TCP was carried out without light irradiation. The photolysis experiment was carried out to observe any possibility of direct photodegradation of 2,4,6-TCP and 2,4-D, while dark adsorption experiment was carried out to observe adsorption/desorption equilibrium of herbicides on photocatalyst and validate the duration (1 h) of dark adsorption used in photocatalysis procedure.

Stability test was carried out on the best samples under similar operational conditions during photocatalytic 2,4,6-TCP mineralisation experiments, except for the increase in amount of photocatalyst powder to 0.5 g. The cycle tests were performed at three hours intervals. The photocatalyst was recovered from solution via centrifugation method and re-used immediately for subsequent cycles without any pre-treatment or make-up.

Studies on uv-vis absorption spectra of 2,4,6-TCP (50 mg/L) at different solution pH was carried out to investigate the influence of 2,4,6-TCP dark adsorption on the absorption spectra around 310 nm. 0.1 M sodium hydroxide (NaOH) and 0.1 M sulfuric acid (H_2SO_4) aqueous solutions were used for the adjustment of solution pH.

4.2.5 Activity analysis

The photocatalytic activity of the prepared TiO_2 samples towards herbicides mineralisation before and after test was investigated primarily using a TOC-L analyser to measure TOC removal rate, after calibration of analyser with KHP as a primary standard. The change in herbicide concentration (degradation rate) was measured using HPLC consisting of a binary pump, an autosampler, a PDA detector and an ACE-5 C18 (5µm × 150 mm × 4.6 mm) reverse phase column maintained at 40 ^{o}C. The HPLC used a 5–95% gradient (Acetonitrile/H_2O with 0.1% formic acid) as the mobile phase. The flow rate was set at 1.0 mL/min and the injection volume was 20 µL. The initial mobile phase was 5% A (acetonitrile) and 95% B (water containing 0.1% formic acid) and kept isocratic for 1 min, followed by a linear gradient to 95% A in 15 min, and kept isocratic for 3 min, and then back to 5% A in 0.5 min. A UV-vis spectrophotometer was also used to monitor herbicides degradation rate with the optimised sample for comparison. The graphical plots were expressed in terms of relative amount of TOC or herbicide concentration left in solution as shown in equations (4-1 and 4-2), while the percentage degradation and mineralisation were calculated from equations (3-5 and 3-10), respectively.

$$Relative\ residual\ TOC \quad = \quad \frac{TOC}{TOC_o} \qquad\qquad Eq.(4-1)$$

$$Relative\ residual\ herbicide \quad = \quad \frac{C}{C_o} \qquad\qquad Eq.(4-2)$$

Where,

- TOC_o = initial concentration of organic carbon in water pollutant

- TOC = remaining concentration of organic carbon after time, t

- C_o = initial concentration of water pollutant

- C = remaining concentration of water pollutant after time, t

Intermediate products formed during herbicide mineralisation were detected using HPLC with a single quadrupole tandem mass spectrometer (HPLC-MS system), equipped with an ESI source. The MS detection was operated in negative ionisation mode.

4.3   Results and discussion

4.3.1 Materials characterisations

The XRD patterns of unmodified PC50 TiO_2 and the selected $FeOOH/TiO_2$ samples with varying Fe concentration are shown in **Fig. 4-2**. Typical diffraction peaks corresponding to anatase (JCPDS 21-1272) are observed in these samples.[163,164] The main diffraction peaks are indexed as the (101), (004), (200), (105), (211), (204), (116), (220) and (215) reflections of

crystalline anatase phase. No characteristic diffraction peaks of Fe-related species (e.g. Fe, FeO, FeOOH, $Fe(OH)_x$, Fe_2O_3 or Fe_3O_4) are observed on the surface modified TiO_2. This could be due to the highly dispersed and low amount of iron species loaded on TiO_2 and the intensive background signal caused by TiO_2.
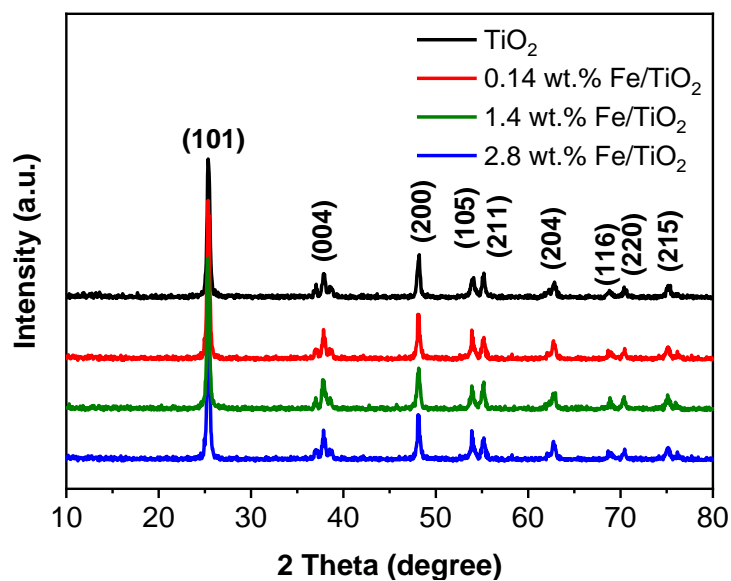
Figure 4-2 XRD patterns of PC50 TiO_2 and FeOOH/TiO_2 samples (0.14, 1.4 and 2.8 wt.% Fe).

The absorption spectra of unmodified PC50 TiO_2 and as-prepared FeOOH/TiO_2 nanocomposites are shown in **Fig. 4-3**. There is a slight change in band-gap for low Fe samples (0.07 - 0.7 wt.%) samples compared to unmodified PC50 TiO_2 (ca. 3.2 eV), indicating low amount of Fe contributes little to the light absorption of the nanocomposites. With increasing Fe loading (up to 2.8 wt.%), there is a significant red shift in light

absorption band edge and lowering of the nanocomposites band-gap to ca. 2.6 eV or 475 nm using equation (3-7), which is due to visible light absorption from the Fe(III) species on TiO_2 surface.
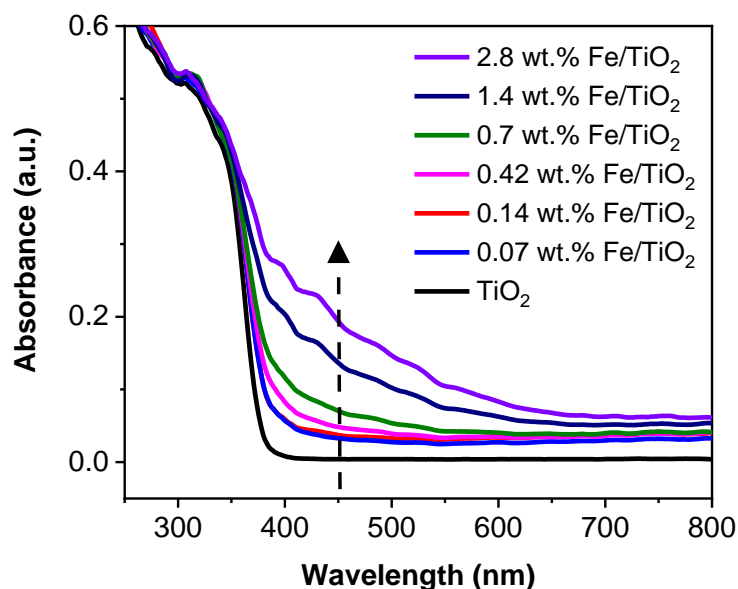
Figure 4-3 UV/vis absorption spectra of prepared $FeOOH/TiO_2$ composites.

High resolution XPS was used to identify the Fe species present in the $FeOOH/TiO_2$ samples. Fe 2p peaks are not observed in the XPS survey spectrum of the 0.14 wt.% Fe sample (**Fig. 4-4**), which is due to the low amount of Fe loading and high dispersion on TiO_2. The Fe 2p peaks are observed after increasing the Fe concentration to 1.4 wt.%. Peaks corresponding to Fe^{3+} are confirmed around 711 eV (Fe $2p^{3/2}$) and 724 eV (Fe $2p^{1/2}$) in the Fe 2p XPS spectrum of 1.4 wt.% Fe sample and no peaks are observed for the 0.14 wt.% Fe sample (**Fig. 4-5**). This could also be due to the low Fe loading in the sample and the intensive background signal

caused by Ti 2p and O 1s signals of TiO_2.[128] Absence of a peak at 709 eV

rules out the presence of Fe^{2+} in the $FeOOH/TiO_2$ nanocomposites.[165]
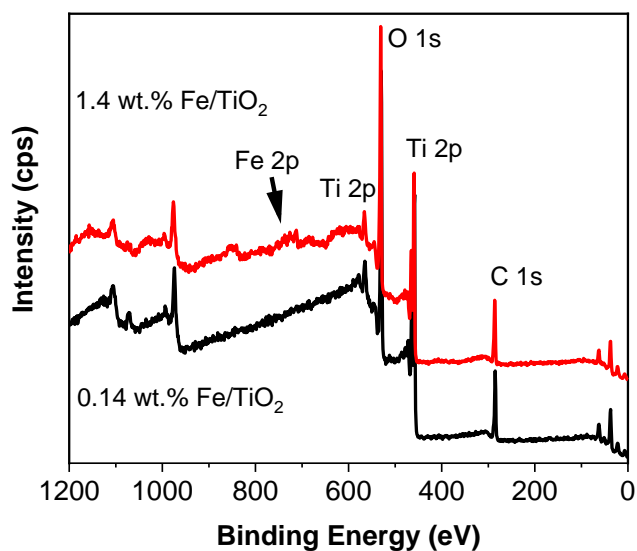
Figure 4-4 XPS survey spectra of $FeOOH/TiO_2$ samples (0.14 and 1.4 wt.% Fe).
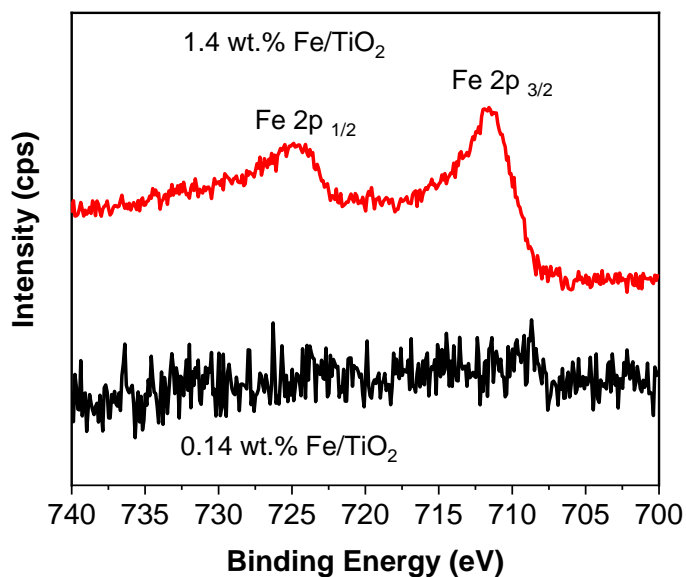
Figure 4-5 High resolution XPS Fe 2p spectra of $FeOOH/TiO_2$ samples (0.14 and 1.4 wt.% Fe).

Based on the N1s scan in **Fig. 4-6**, residual nitrogen species, which were absent in the PC50 TiO_2, could be slightly detected on the surface of FeOOH/TiO_2 (0.14 wt.% Fe) sample. Furthermore, for N 1s scan, a single peak observed around 407 eV corresponds to NO_3^- species as reported in literature.[166]
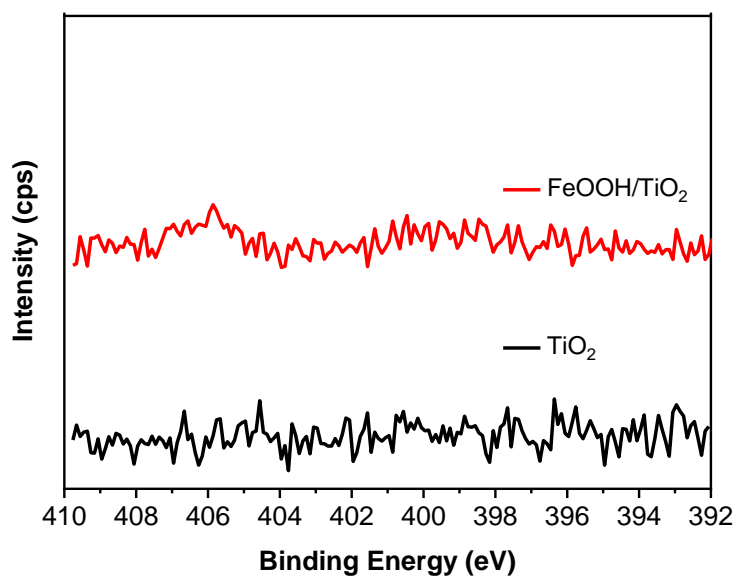
Figure 4-6 N 1s spectra of PC50 TiO_2 and FeOOH/TiO_2 (0.14 wt.% Fe).

The XRD patterns of 0.14 wt.% Fe/TiO_2 samples, calcined at different temperatures are shown in **Fig. 4-7**. Typical diffraction peaks corresponding to anatase (JCPDS 21-1272) are also observed in all samples.[163,164] The diffraction peaks relating to Fe species could not be identified here. This could again be due to the highly dispersed and low concentration of Fe species and intensive background signal caused by TiO_2.
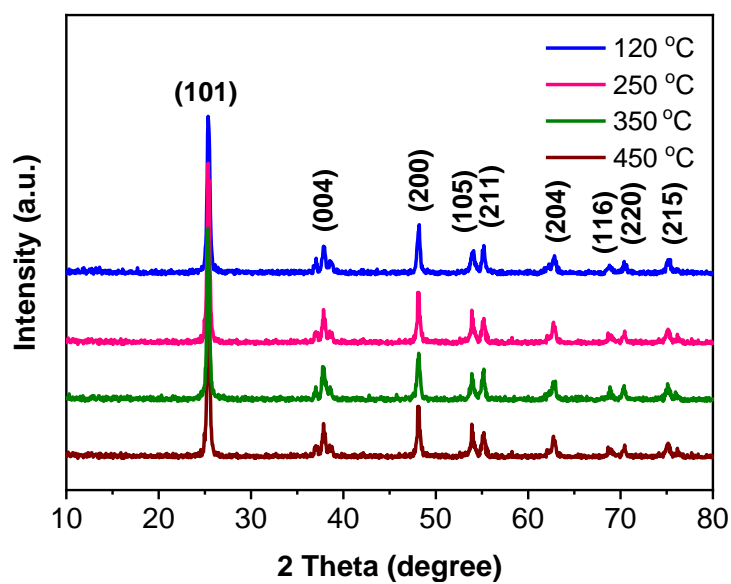
Figure 4-7 XRD patterns of 0.14 wt.% Fe/TiO$_2$ composites calcined at different temperatures.

The UV-vis absorption spectra of 0.14 wt.% Fe/TiO$_2$ nanocomposites calcined at different temperatures are shown in **Fig. 4-8**. There is no significant shift in the light absorption band-edge for all samples.
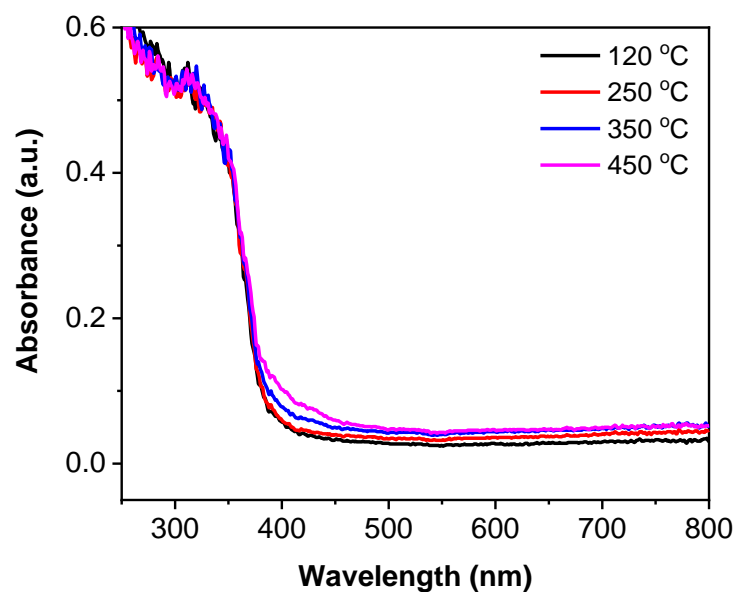
Figure 4-8 UV/vis absorption spectra of 0.14 wt.% Fe/TiO$_2$ composites calcined at different temperatures.

The SEM and TEM images in **Figs. 4-9** and **4-10** reveal an aggregate structure of the nanoparticles with average particle size of the anatase TiO$_2$ to be approximately 20–30 nm but the Fe (III) species could not be imaged directly at this low Fe concentration. This is due to the high dispersity of Fe species on TiO$_2$ as shown in the EDS elemental mapping for Fe and Ti (**Fig. 4-10**).
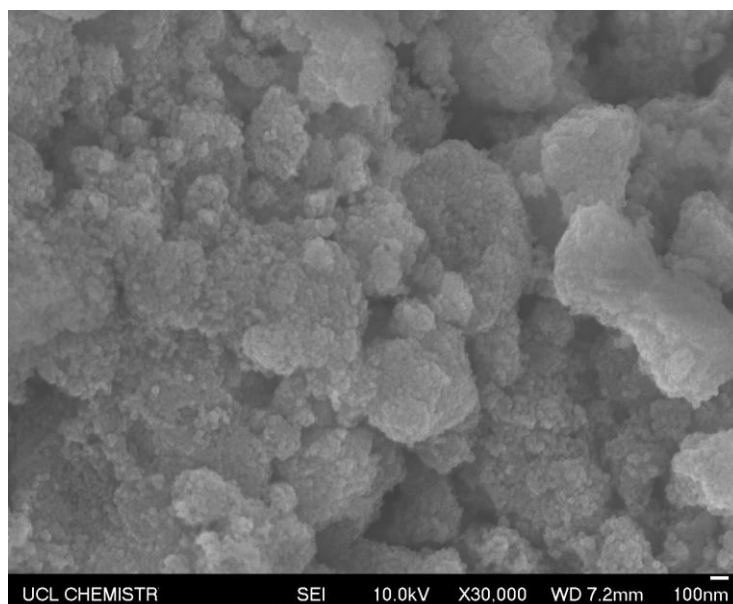
Figure 4-9 SEM image of FeOOH/TiO$_2$ (0.14 wt.% Fe).
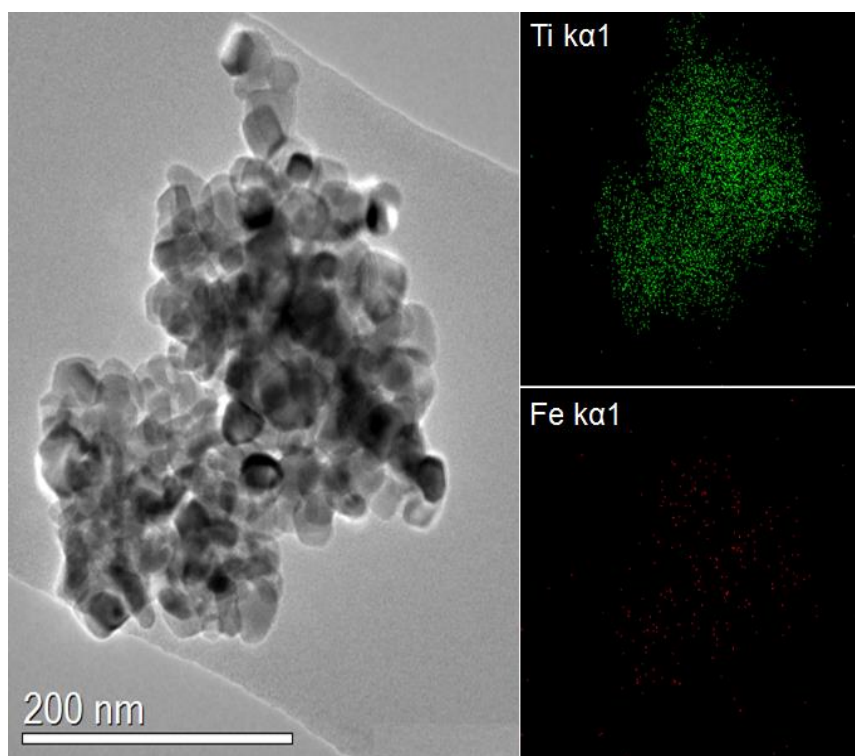
Figure 4-10 TEM image of FeOOH/TiO$_2$ (0.14 wt.% Fe) and EDS elemental mapping showing Ti and Fe.

To investigate the impact of calcination temperature on the physical properties of the modified samples, BET surface area measurements were carried out and results are displayed in **Table 4-1**. From the results, there appears to be little variation in surface area from unmodified TiO_2 to the sample calcined at 450 ^{o}C. This implies that the moderate surface impregnation method neither reduced the surface area of PC50 TiO_2 nor significantly increased the surface area.

Table 4-1 BET surface area analysis for effect of calcination temperature.

BET surface area					
Sample	TiO_2		0.14 wt.%	Fe	
	(unmodified)	(120 ^{o}C)	(250 ^{o}C)	(350 ^{o}C)	(450 ^{o}C)
S.A (m^2/g)	47	48	48	49	49

4.3.2 Photocatalytic mineralisation of herbicides

The calibration curve for the TOC analyser using KHP standard solutions as organic substrate is displayed in **Fig. 4-11** and it shows a good linear fit (r^2 = 0.9999).
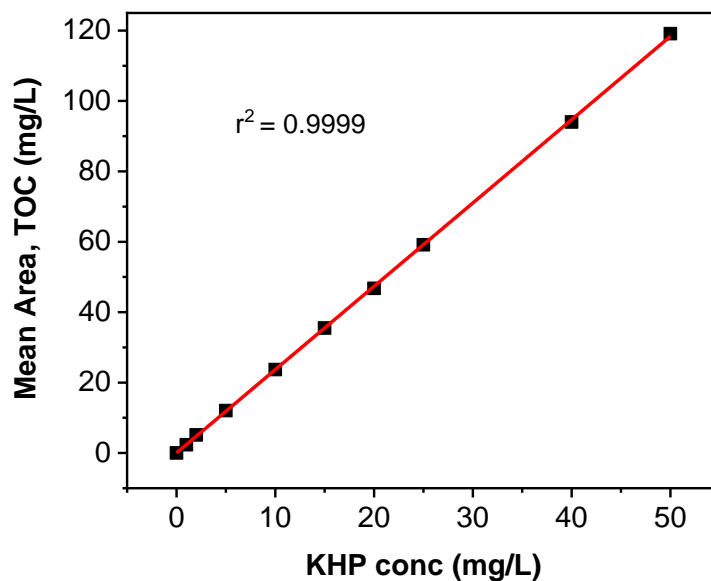
Figure 4-11 TOC calibration curve using KHP standards.

The adsorption-desorption equilibrium of 2,4,6-TCP on the photocatalyst was achieved in 30 min as shown in **Fig. 4-12** and **Fig. 4-13**. The peak at 292 nm was monitored since the shoulder peak at 310 nm is very sensitive to slight changes in solution pH as confirmed in **Fig. 4-14**. This phenomenon could be due to protonation/deprotonation of the O-H group in 2,4,6-TCP.[90]
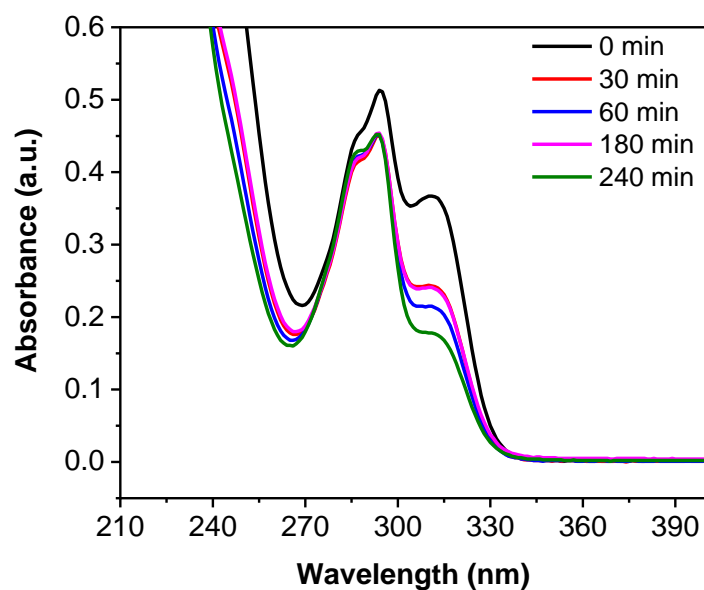
Figure 4-12 Typical UV-vis absorption spectra of 2,4,6-TCP on FeOOH/TiO$_2$ (0.14 wt.% Fe) in the dark.

Conditions: 2,4,6-TCP (50 mg/L, 200 mL, pH$_{nat}$ = 6, catalyst concentration = 0.5 g/L).
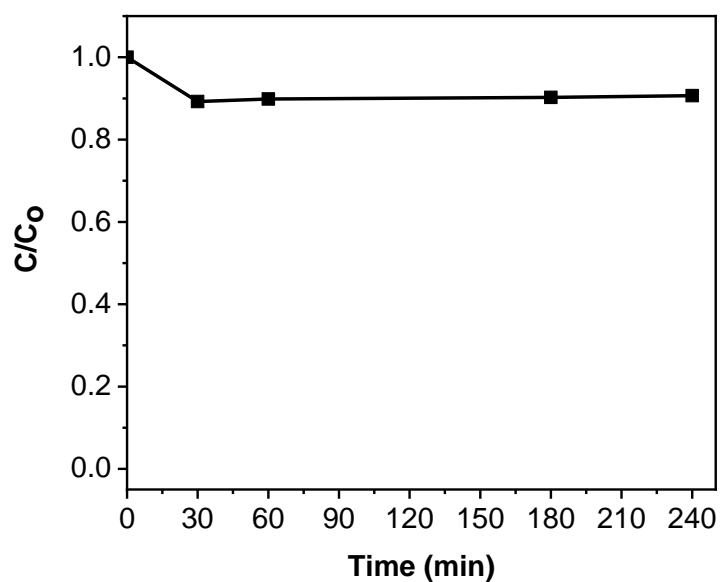
Figure 4-13 Adsorption-desorption equilibrium graph.

Conditions: 2,4,6-TCP (50 mg/L, 200 mL, pH$_{nat}$ = 6, catalyst = 0.5 g/L).
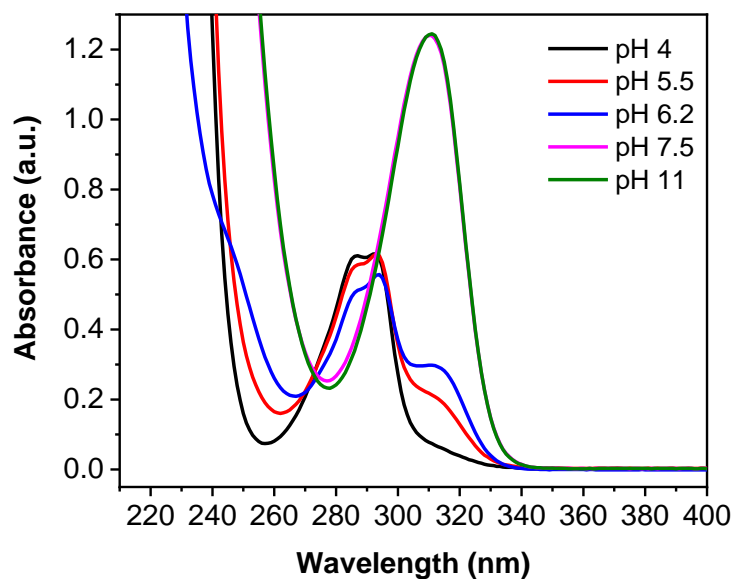
Figure 4-14 Typical UV-vis absorption spectra of 2,4,6-TCP (50 mg/L) at different solution pH.

The control experiment was carried out with only 2,4,6-TCP solution in the absence of photocatalyst. Virtually 0% TOC removal is observed after 4 h of light irradiation as shown in **Fig. 4-15**. Photocatalytic activities of the as-prepared $FeOOH/TiO_2$ composites were then evaluated by the mineralisation of 2,4,6-TCP under full arc light irradiation ($\lambda > 320$ nm) as shown in **Fig. 4-15**. Similar observation is recorded from the UV-vis absorption spectra measurements in **Fig. 4-16** since the glass window shields all UV light with wavelength below 320 nm. The 2,4,6-TCP mineralisation rate recorded by PC50 TiO_2 is nearly 50% after 4 h. Approximately 71% TOC removal is achieved with $FeOOH/TiO_2$ (0.07 wt.% Fe) sample after 4 h. An increase in Fe concentration up to 0.14 wt.% Fe

leads to a further increase in photocatalytic activity, while poor 2,4,6-TCP

mineralisation rates are observed with 1.4 and 2.8 wt.% Fe-loaded samples.
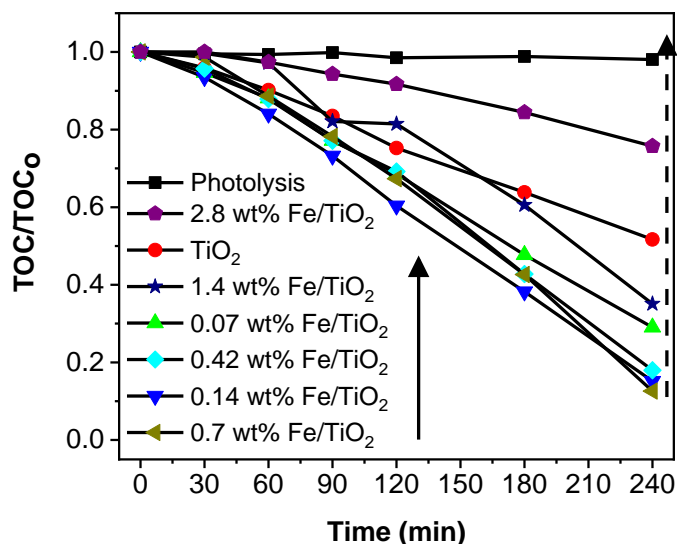
Figure 4-15 Mineralisation profiles of 2,4,6-TCP using $FeOOH/TiO_2$ with different Fe loading and control experiment.

Conditions: 2,4,6-TCP (50 mg/L, 200 mL, pH_{nat} = 6, catalyst concentration = 0.5 g/L, λ > 320 nm).
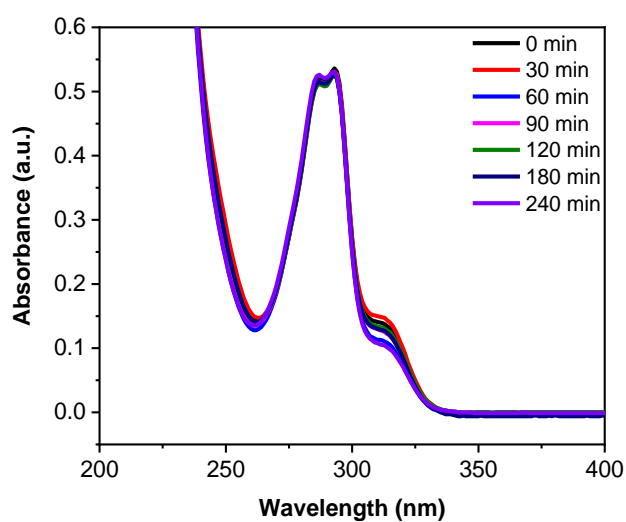
Figure 4-16 Typical UV-vis absorption spectra of 2,4,6-TCP (50 mg/L, pH_{nat} = 6) during photolysis.

The optimum condition for the preparation of FeOOH/TiO$_2$ nanocomposites is found to be 0.14 wt.% Fe with ca. 85% TOC removal after 4 h, nearly doubling the benchmark photocatalyst PC50 activity. Cocatalyst loading of 0.42 and 0.7 w.t% Fe also display close photocatalytic activity as the optimised sample in **Fig. 4-17**. However, a significant reduction in the photocatalytic mineralisation efficiency is observed with higher Fe concentration (2.8 wt.% Fe), compared to unmodified PC50 TiO$_2$ after 4 h test.
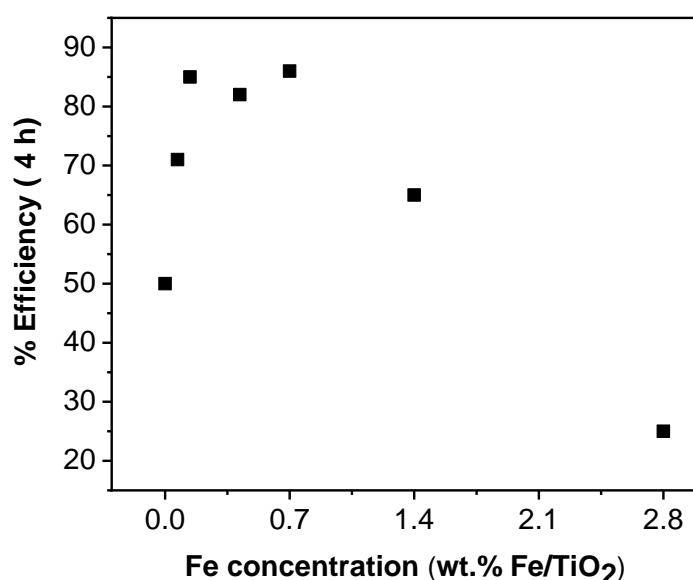
Figure 4-17 A plot of 2,4,6-TCP mineralisation efficiency versus Fe concentration in FeOOH/TiO$_2$ at 4 h run.

Generally, cocatalyst is required to improve the photocatalytic degradation rate due to enhanced charge separation and catalytic effect, while

increasing the amount of cocatalyst over the optimum adversely affects the photocatalytic activity, which was also reported in literature.[167–169] This observation could be due to shielding of intrinsic light absorption by colorful cocatalysts and occupying the oxidation sites on TiO_2.[128] Higher loadings of Fe(III) on the surface of TiO_2 may hinder light irradiation, thus reduces the generation and separation of electrons and holes on TiO_2. Therefore, for the FeOOH/TiO_2 nanocomposites, there is a trade-off between the two effects incurred by supporting Fe species, leading to the existence of an optimum Fe loading on TiO_2.[170]

Furthermore, to investigate the contribution of the choice of Fe(III) precursors, FeOOH/TiO_2 (0.14 wt.% Fe) was prepared using other low cost Fe precursors (sulphate and chloride). From the results in **Fig. 4-18**, there is no significant difference in photocatalytic mineralisation activities of the three samples. However, the composite prepared from Fe(III) nitrate has a slight edge after 240 min as observed from the TOC measurements, thus Fe(III) nitrate was used again as Fe precursor for subsequent experiments.
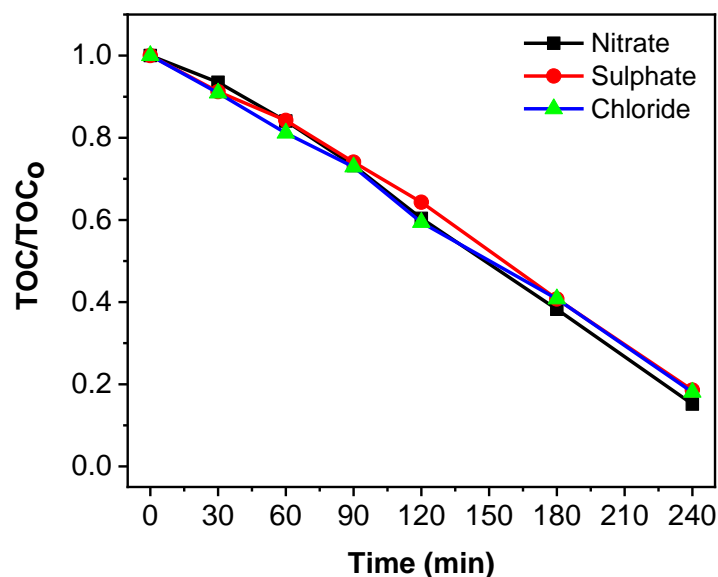
Figure 4-18 Mineralisation profiles of 2,4,6-TCP using $FeOOH/TiO_2$ (0.14 wt.% Fe) prepared with different Fe (III) precursors.

Conditions: 2,4,6-TCP (50 mg/L, 200 mL, pH_{nat} = 6, catalyst concentration = 0.5 g/L, λ > 320 nm).

The effect of calcination temperature was investigated with optimised Fe/TiO_2 composite (0.14 wt.% Fe loading). The highest photocatalytic activity is observed with the sample prepared at 120 ^{o}C. Nearly complete 2,4,6-TCP mineralisation (100% TOC removal) is achieved in 4 h run, as shown in **Fig. 4-19**, and about 15% higher than the $FeOOH/TiO_2$ sample prepared at 250 ^{o}C. The $FeOOH/TiO_2$ is 40% more active than Fe_2O_3/TiO_2 prepared at 350 ^{o}C, while the latter is still better than pure TiO_2 as was earlier reported.[23] An increase in calcination temperature beyond 350 ^{o}C negatively affects the photocatalytic activity of the nanocomposites. The

worst is the sample calcined at 450 ^{o}C, with only about 35% TOC removal in

4 h run.
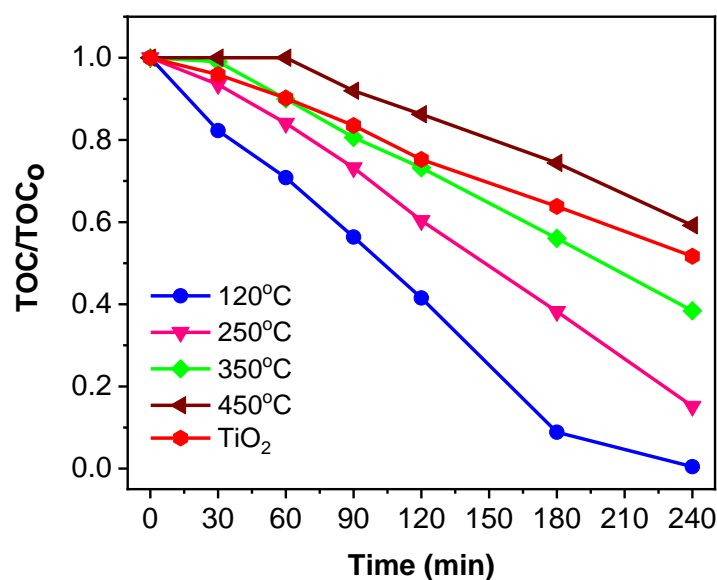
Figure 4-19 Mineralisation profiles of 2,4,6-TCP using 0.14 wt.% Fe/TiO$_2$
with different calcination temperatures.

Conditions: 2,4,6-TCP (50 mg/L, 200 mL, pH$_{nat}$ = 6, catalyst concentration =
0.5 g/L, λ > 320 nm).

The experimental error bar of the optimised FeOOH/TiO$_2$ is shown in **Fig. 4-20** after carrying out the mineralisation experiment in triplicates. The result signifies that the experiment is repeatable to a large extent. Such enhancement in activity of the sample calcined at both 120 ^{o}C and 250 ^{o}C might have some contribution from defects on FeOOH cocatalyst. Also,

FeOOH could improve the adsorption of organic contaminants on TiO_2 as reported in literatures.[171]
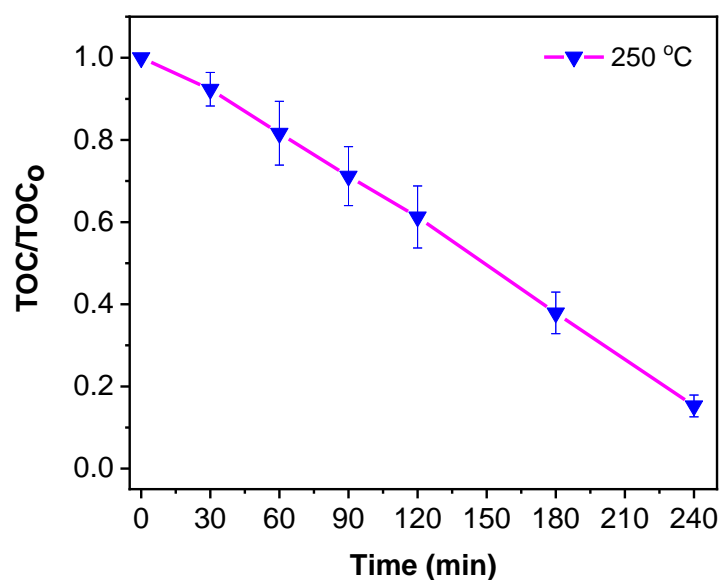
Figure 4-20 TOC measurement with experimental error bar of optimised FeOOH/TiO_2 (0.14 wt.% Fe) after conducting triple experiments.

In order to measure 2,4,6-TCP concentration and evaluate its degradation rate, a calibration curve (**Fig. 4-21**) was plotted using measurements from an HPLC system. The PDA detector wavelength was set at 292 nm (lambda max, λ_{max}) and it shows a good linear fit (r^2 = 0.998). The corresponding temporal HPLC chromatograms for 2,4,6-TCP degradation over optimised FeOOH/TiO_2 are displayed in **Fig. 4-22**. Six intermediate products are

identified, which will be discussed in detail under 2,4,6-TCP degradation pathway (**4.3.5**). The limit of direct quantification of 2,4,6-TCP in aqueous phase with the HPLC is around 0.04 mg/L or 40 µg/L at 292 nm wavelength.
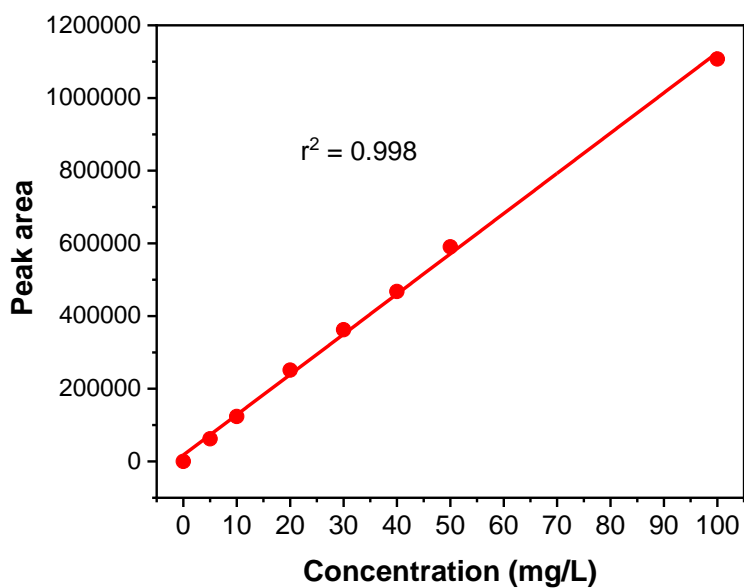
Figure 4-21 Calibration curve for 2,4,6-TCP standards using HPLC with 292 nm as PDA wavelength.
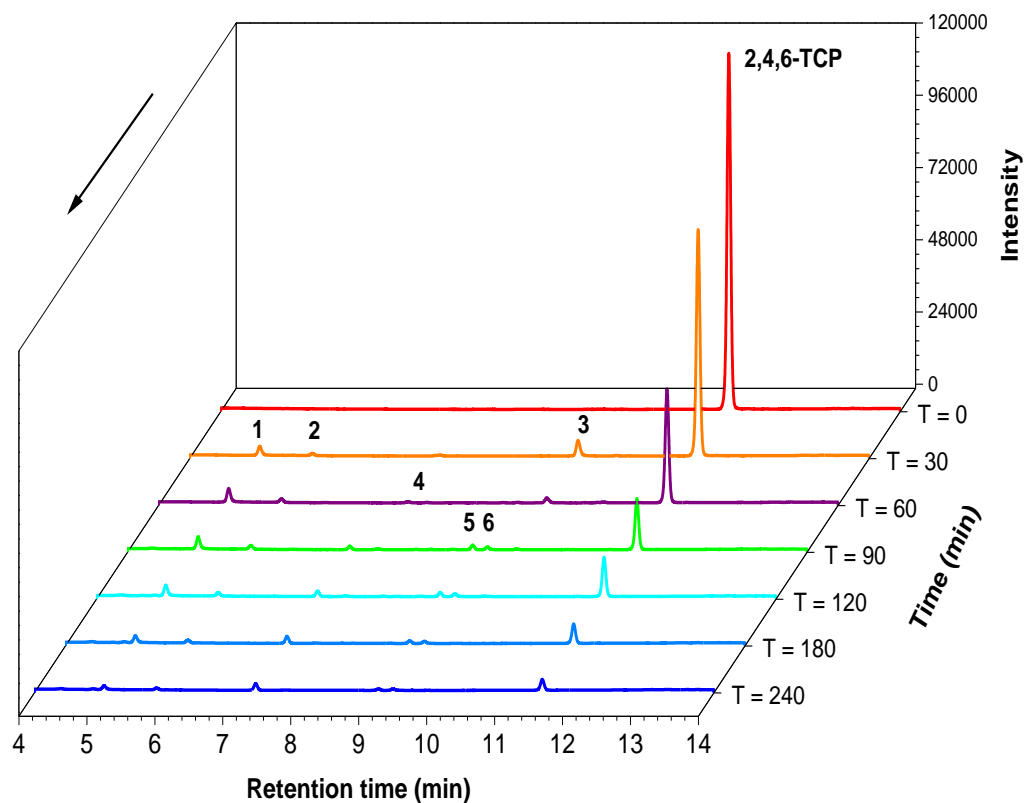
Figure 4-22 HPLC chromatograms showing the degradation profiles of 2,4,6-TCP over FeOOH/TiO$_2$ (0.14 wt.% Fe).

Conditions: 2,4,6-TCP (50 mg/L, 200 mL, pH$_{nat}$ = 6, catalyst concentration = 0.5 g/L, λ > 320 nm).

The 2,4,6-TCP degradation process follows typical pseudo-first-order kinetics on both unmodified TiO$_2$ and optimised FeOOH/TiO$_2$ samples (**Fig. 4-23**).[172] The initial rate constant for the optimised FeOOH/TiO$_2$ sample was calculated to be 0.0193 min^{-1}, which is 3 times that of unmodified PC50 TiO$_2$ (0.00647 min^{-1}).
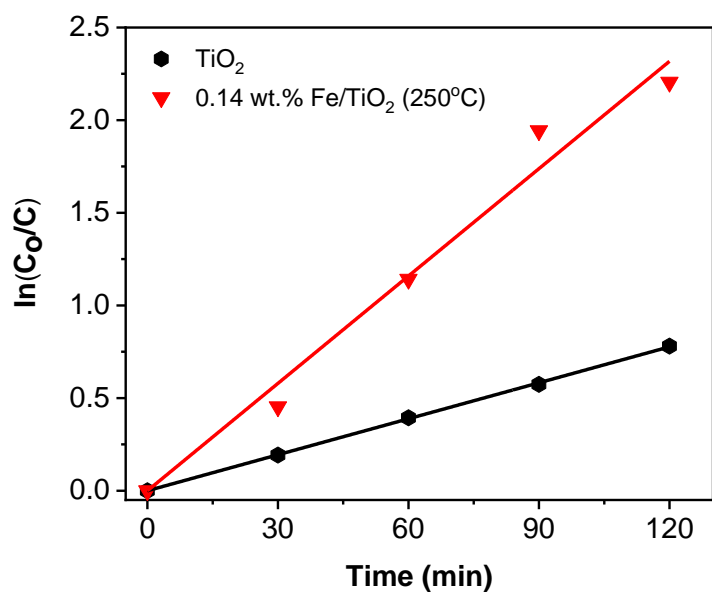
Figure 4-23 Pseudo-first-order kinetics plots for 2,4,6-TCP degradation using PC50 TiO_2 and $FeOOH/TiO_2$ (0.14 wt.% Fe).

Fig. 4-24 shows a comparison between unmodified TiO_2 and $FeOOH/TiO_2$ (0.14 wt.% Fe) for 2,4,6-TCP degradation. Nearly 50% and 90% degradation rates are achieved in 2 h with the unmodified TiO_2 and optimised $FeOOH/TiO_2$ sample, respectively.
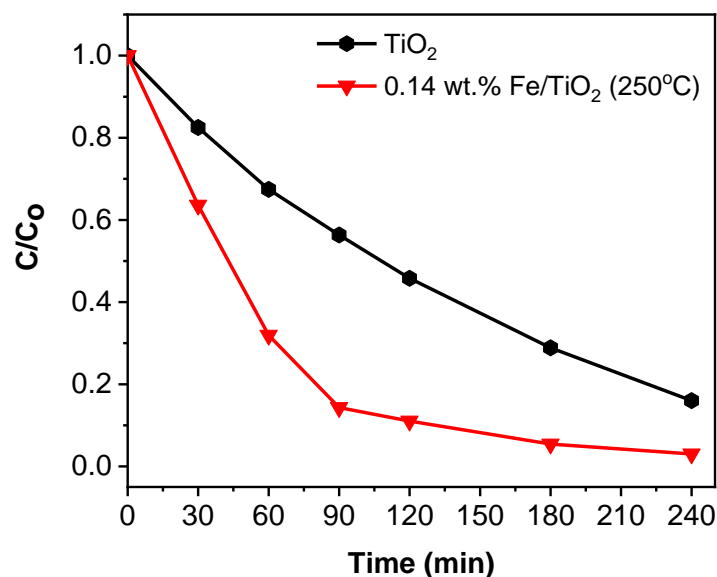
Figure 4-24 Degradation profiles of 2,4,6-TCP using PC50 TiO_2 and optimised $FeOOH/TiO_2$ sample monitored by HPLC.

Conditions: 2,4,6-TCP (50 mg/L, 200 mL, pH_{nat} = 6, catalyst concentration = 0.5 g/L, λ > 320 nm).

2,4,6-TCP removal over optimised $FeOOH/TiO_2$ was also analysed with a UV-vis spectrophotometer and compared with results obtained from TOC and HPLC analyses, as shown in **Fig. 4-25**. The UV-vis result tends to be less accurate when compared with measurements from HPLC. This could be due to interference of colorless intermediate products at the monitored wavelength (292 nm) for 2,4,6-TCP degradation. In 120 min, TOC shows approximately 60% of organic substance still exists, while HPLC indicates 90% of 2,4,6-TCP was converted. The mineralisation efficiency is notably less than the degradation efficiency due to the generation of organic intermediates during photocatalysis.
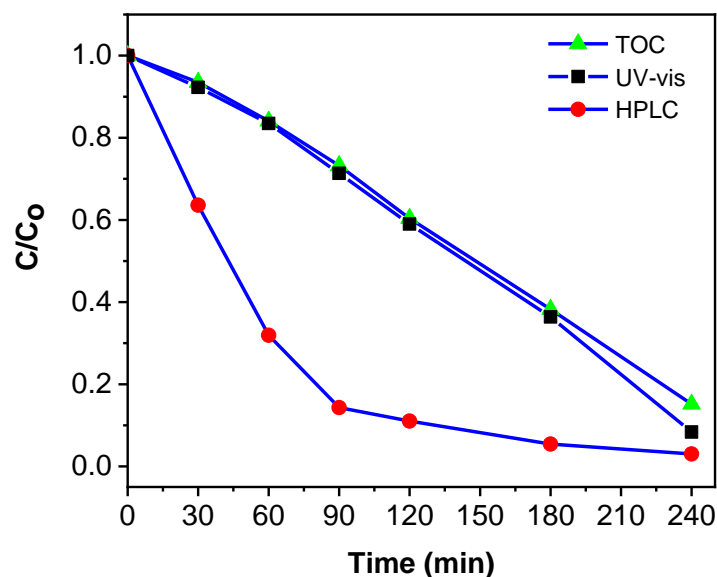
Figure 4-25 Comparison of results obtained from TOC, HPLC and UV-vis measurements for 2,4,6-TCP degradation using optimised FeOOH/TiO$_2$ sample.

Conditions: 2,4,6-TCP (50 mg/L, 200 mL, pH$_{nat}$ = 6, catalyst concentration = 0.5 g/L, λ > 320 nm).

The poor 2,4,6-TCP mineralisation rates recorded for the samples calcined at 350 and 450 ^{o}C are not related to the BET surface area of the samples (**Table 4-1**) and light absorption ability (**Fig. 4-8**). This implies that the nature of Fe (III) species on TiO$_2$ is responsible for the disparity in photocatalytic degradation efficiency. The Fe(III) containing oxides were thus prepared without the substrate TiO$_2$ and evaluated for 2,4,6-TCP degradation.[171] The results in **Fig. 4-26** show 0 and 10% 2,4,6-TCP mineralisation efficiencies in 3 h are obtained by Fe$_2$O$_3$ prepared at 450 ^{o}C and FeOOH prepared at 250 ^{o}C without TiO$_2$, respectively, indicating the FeOOH species prepared at 250 ^{o}C is rather active. It was reported that if

115

the Fe_2O_3 content is dominating over FeOOH, such as in the 0.14 wt.% Fe/TiO$_2$ (450 °C) sample and Fe(III) species prepared at 450 °C, part of the Fe_2O_3 sites may become electron-hole recombination centers.[171]
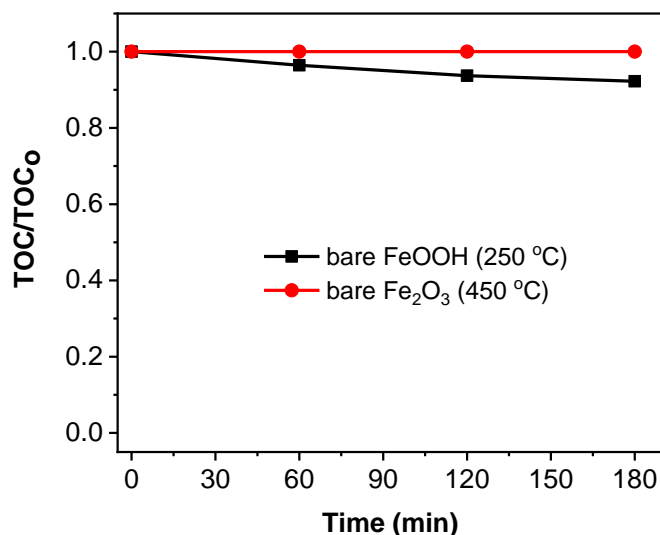
Figure 4-26 Mineralisation profiles of 2,4,6-TCP using only as-prepared Fe(III) cocatalysts without TiO$_2$.

Conditions: 2,4,6-TCP (50 mg/L, 200 mL, pH$_{nat}$ = 6, catalyst concentration = 0.5 g/L, λ > 320 nm).

Further studies on photocatalytic mineralisation ability of the optimised FeOOH/TiO$_2$ sample, based on its 2,4,6-TCP mineralisation efficiency, was evaluated with a widely used herbicide, 2,4-dichlorophenoxyacetic acid (2,4-D) and results are displayed in **Fig. 4-27**. 0% TOC removal is observed after 3 h of light irradiation in the absence of a photocatalyst. Similar observation was recorded from the UV-vis absorption spectra measurements (**Fig. 4-28**). Nearly 60% and 95% TOC removal are achieved with the unmodified TiO$_2$ and optimised FeOOH/TiO$_2$ sample, respectively.
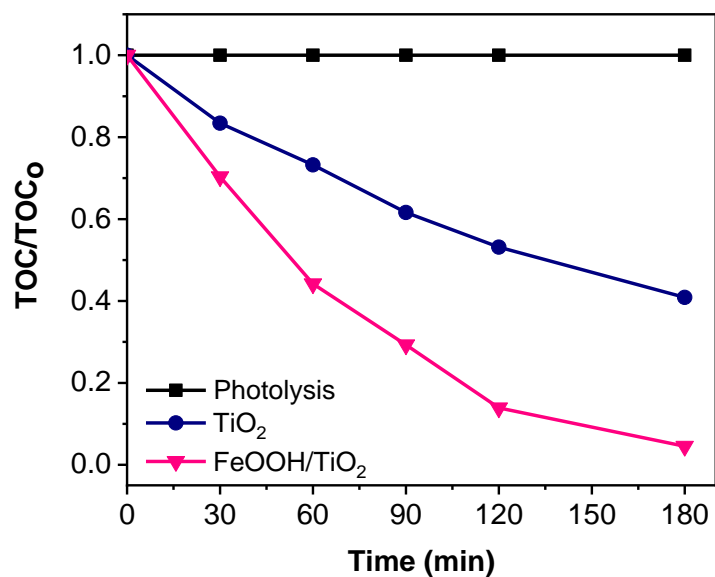
Figure 4-27 Mineralisation profiles of 2,4-D using PC50 and FeOOH/PC50 (0.14 wt.% Fe) sample.

Conditions: 2,4-D (25 mg/L, 200 mL, pH_{nat} = 4, catalyst concentration = 0.5 g/L, λ > 320 nm).
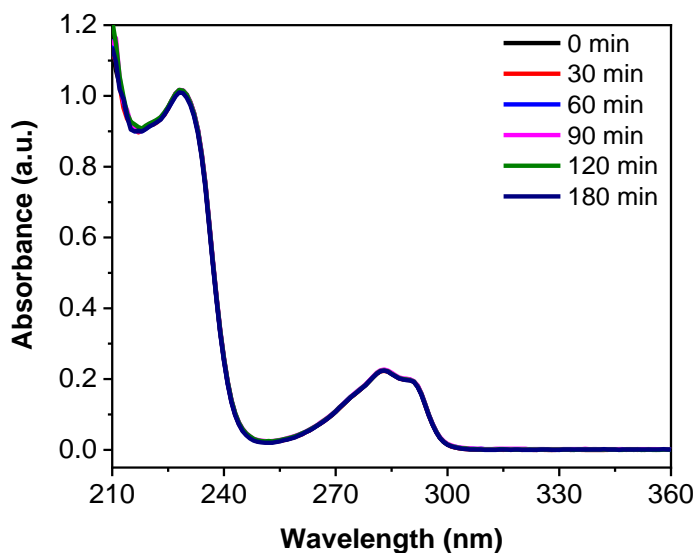
Figure 4-28 Typical UV-vis absorption spectra of 2,4-D during photolysis.

Conditions: 2,4-D (25 mg/L, 200 mL, pH_{nat} = 4, λ > 320 nm).

2,4-D removal by the optimised $FeOOH/TiO_2$ was also analysed with HPLC and UV-vis spectra and results are shown in **Fig. 4-29**. Similar to what is observed in **Fig. 4-25**, the UV-vis spectra results is less accurate when compared with measurements from HPLC, which is again due to interference of colorless intermediate products at the monitored wavelength (228 nm)[173] for 2,4-D degradation.
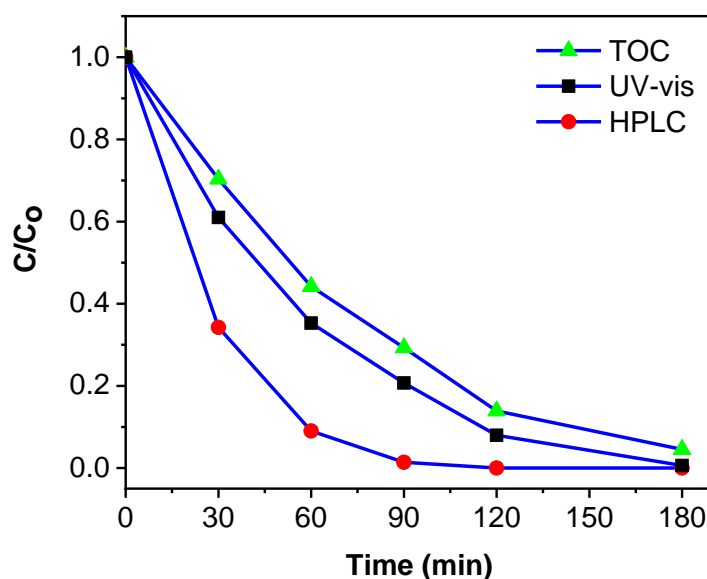
Figure 4-29 Comparison of results obtained from TOC, HPLC and UV-vis spectrophotometer for 2,4-D degradation using optimised $FeOOH/TiO_2$ sample.

Conditions: 2,4-D (25 mg/L, 200 mL, pH_{nat} = 4, catalyst concentration = 0.5 g/L, λ > 320 nm).

4.3.3 The characterisation of Fe(III) species as cocatalysts

Due to the difficulty in identifying the highly dispersed specific Fe(III) species on TiO_2, the iron precursor of large amount was used to prepare samples at different temperatures[171] (1 g of sample, calcined for 6 h) and the yield was sufficient for analysis using Raman spectroscopy and XRD. The XRD patterns in **Fig. 4-30** with enlarged XRD patterns of some selected samples (**Fig. 4-31**) are matched with a reference database, and could give a clue to the likely Fe(III) species obtained at different calcination temperatures. Samples calcined at 350 and 450 ^{o}C consist of hematite, Fe_2O_3 (JCPDS 33-0664)[174,175], sample calcined at 250 ^{o}C matches FeOOH (JCPDS 76-0182)[176], while the sample calcined at 120 ^{o}C is a mixture of Fe(III) species i.e., trace amount of $Fe_4NO_3(OH)_{11}$ (JCPDS 44-0520)[177] and the major phase of FeOOH.
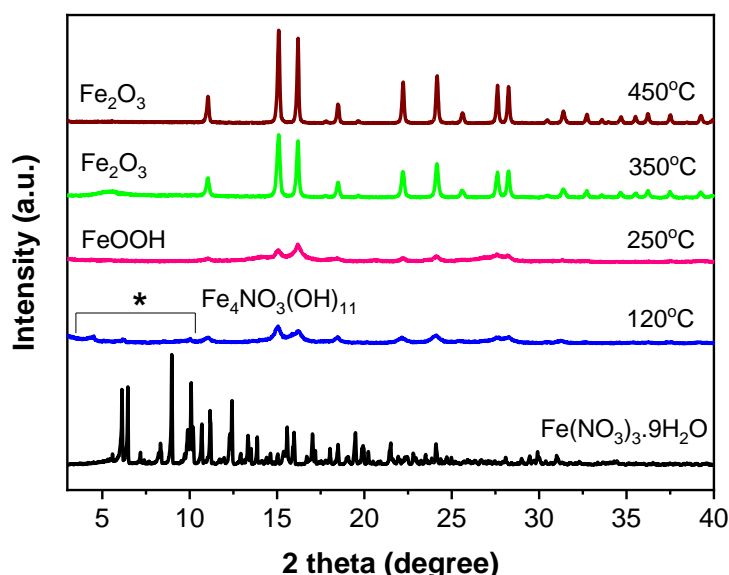
Figure 4-30 XRD patterns of the products obtained after calcination of Fe(III) nitrate nonahydrate at different temperatures.

119
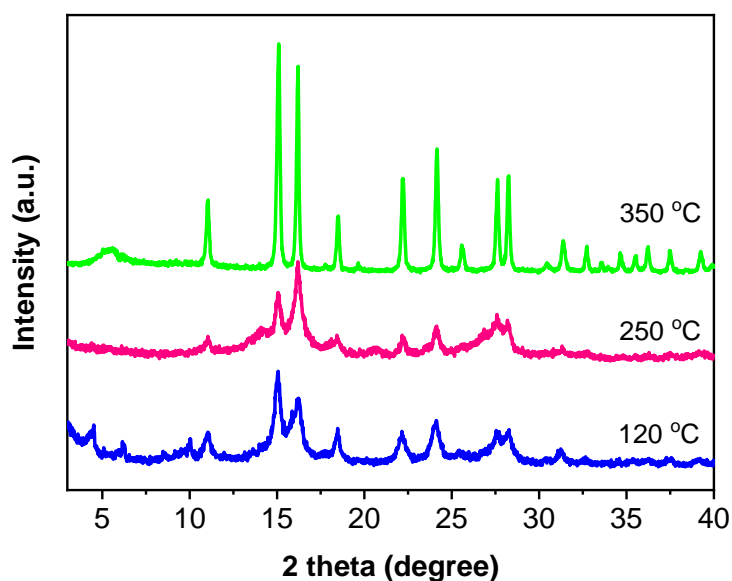
Figure 4-31 Enlarged XRD patterns of three Fe(III) samples from **Fig. 4-30**.

Based on the Raman spectra in **Fig. 4-32**, the samples calcined at 350 and 450 ^{o}C exhibit the characteristic Raman shift peaks of hematite (Fe_2O_3) i.e. 293, 405 and 613 cm^{-1}, which are absent in the samples calcined at 120 and 250 ^{o}C, and consistent with XRD analysis.[178] The Raman peaks of samples calcined at 120 and 250 ^{o}C are left-shifted, with a characteristic peak (*) around 390 cm^{-1} indicating FeOOH species.[178] Therefore, the presence of FeOOH species is the key here which enhanced the photocatalytic activity of the composites prepared at 120 ^{o}C and 250 ^{o}C.
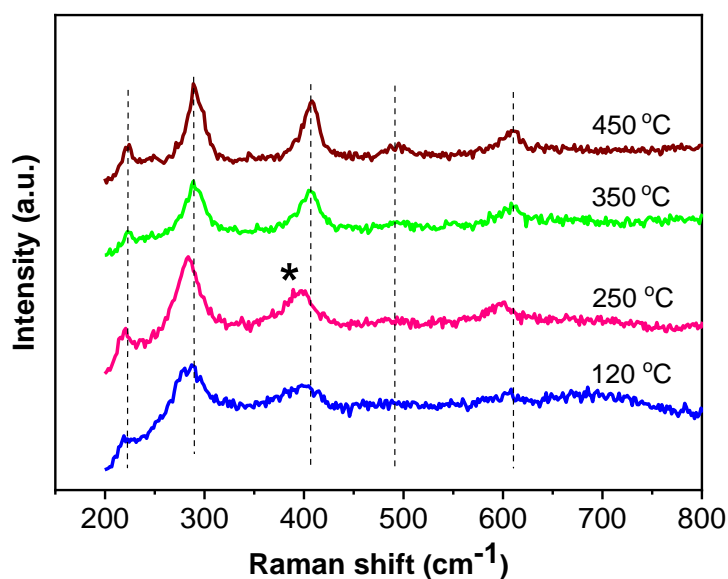
Figure 4-32 Raman spectra of the products obtained after calcination of Fe (III) nitrate nonahydrate at different temperatures.

To investigate whether charge transfer is facilitated between TiO_2 and the Fe (III) species, PL measurements were carried out (**Fig. 4-33**). Strong light emission spectra with peak around 550 nm is observed from bare TiO_2 under 325 nm laser light excitation/absorption but surprisingly, about 95% and 80% reduction in the emission intensities are observed with optimised Fe/TiO_2 samples prepared at 250 ^{o}C and 120 ^{o}C, respectively. Although the samples exhibit similar band-gap absorption (**Fig. 4-8**), this is a strong indication of the efficiency of charge separation and transfer between FeOOH and TiO_2. Therefore, the enhanced photocatalytic performance is attributed to the efficient charge separation and catalytic effect of FeOOH.
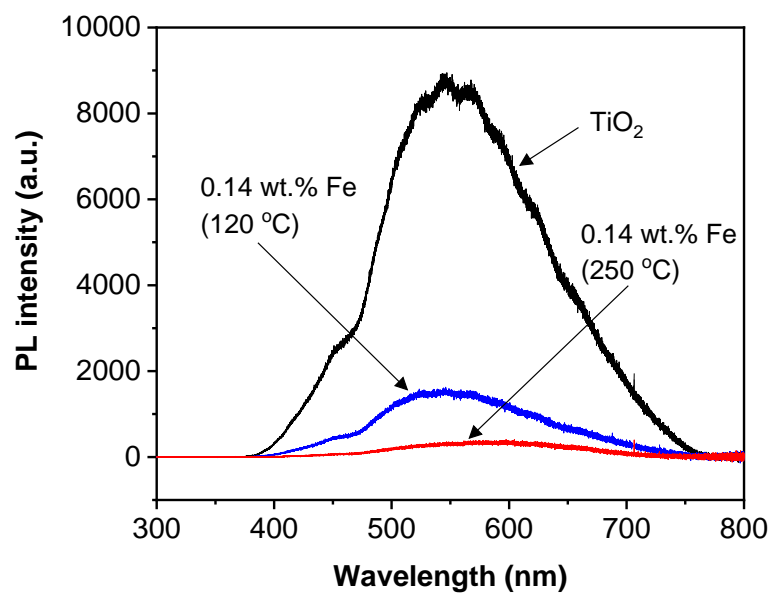
Figure 4-33 PL spectra of unmodified PC50 TiO_2 and optimised Fe/TiO_2 (0.14 wt.% Fe) samples prepared at 120 and 250 °C.

4.3.4 Catalyst recycling and reactive oxygen species tests

The graph in **Fig. 4-34** shows normalised activities with TiO_2 as a reference,

when taking into account the stable activity of pure TiO_2 (**Fig. 4-35**).
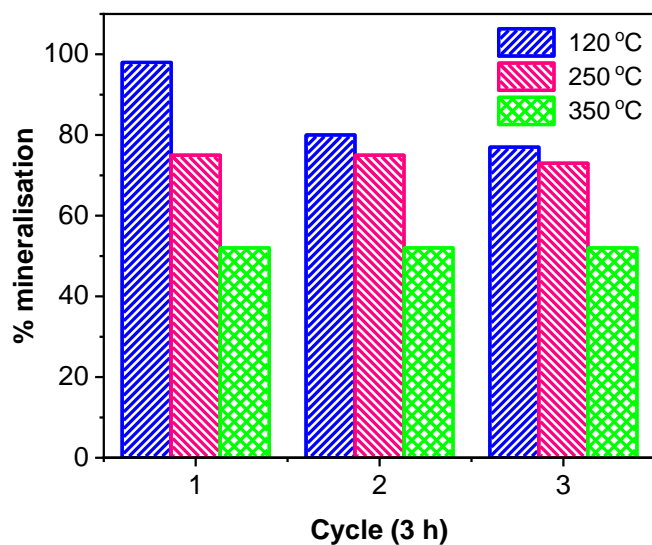
Figure 4-34 Recycling performance of 0.14 wt.% Fe/TiO$_2$ samples at different calcination temperatures with normalisation when taking TiO$_2$ as a reference.

Conditions: 2,4,6-TCP (50 mg/L, 200 mL, pH$_{nat}$ = 6, catalyst concentration = 2.5 g/L, λ > 320 nm).
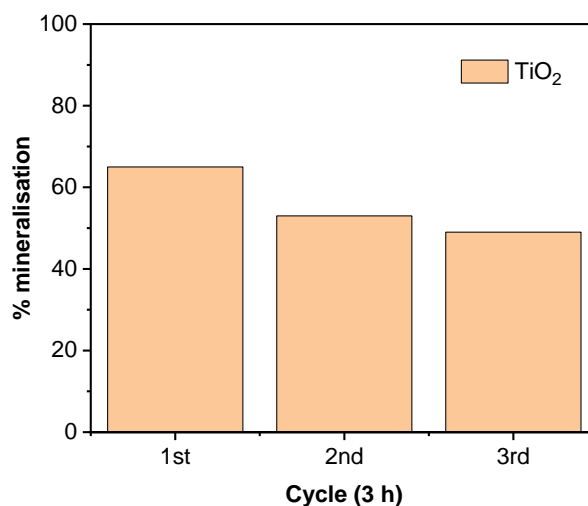
Figure 4-35 Recycling performance of pristine PC50 TiO$_2$.

Conditions: 2,4,6-TCP (50 mg/L, 200 mL, pH$_{nat}$ = 6, catalyst concentration = 2.5 g/L, λ > 320 nm).

The photocatalytic recyclability performance follows the order: 350 ^{o}C $\approx$ 250 ^{o}C > 120 ^{o}C. This implies that at higher calcination temperature, more stable photocatalysts were produced, which might be due to a more intimate contact between the Fe(III) species and TiO_2 particles. The sample prepared at 250 ^{o}C (FeOOH/TiO_2) is quite stable unlike the sample prepared at 120 ^{o}C (FeOOH + $Fe_4NO_3(OH)_{11}$/TiO_2). This could likely be due to the presence of iron nitrate hydroxide impurities that could help catalytic effect of FeOOH but is not as stable as FeOOH. The lower photocatalytic degradation efficiency recorded for the 350 ^{o}C calcined sample, compared to others, is likely due to the conversion of FeOOH to Fe_2O_3 on TiO_2 surface.[179] Therefore, the best in terms of activity is 0.14 wt.% Fe/TiO_2 prepared at 120 ^{o}C, while taking into account both stability and activity, the optimised sample is the one prepared at 250 ^{o}C (0.14 wt.% Fe/TiO_2), which represents FeOOH/TiO_2.

It is generally accepted that the reaction pathways for photocatalytic degradation of organic water contaminants are dominated by several active species (e.g. holes, superoxide radicals and hydroxyl radicals).[180,181] Herein, some scavengers were utilised to confirm the active species, which will further assist in understanding the photocatalytic degradation mechanism for 2,4,6-TCP degradation, using the optimised FeOOH/TiO_2 (0.14 wt.% Fe) sample prepared at 250 ^{o}C. EDTA was used as hole (h^+) scavenger, isopropanol (IPA) as hydroxyl radical ($^{\cdot}$OH) scavenger and 1,4-benzoquinone as superoxide radical ($^{\cdot}O_2^-$) scavenger.[155] As shown in **Fig. 4-36**, about 97% 2,4,6-TCP degradation is recorded in 4 h without any

additive. The degradation rate drops to about 70% in the presence of hole scavenger and about 20% with superoxide radical ($^{\cdot}O_2^{-}$) scavenger, while virtually no activity is recorded with hydroxyl radical scavenger. This implies that the degradation of 2,4,6-TCP was mostly dominated by hydroxyl radicals and superoxide radicals, since the degradation of 2,4,6-TCP is drastically reduced in their absence. This observation is somewhat consistent with results reported in the literature.[136,155,180]
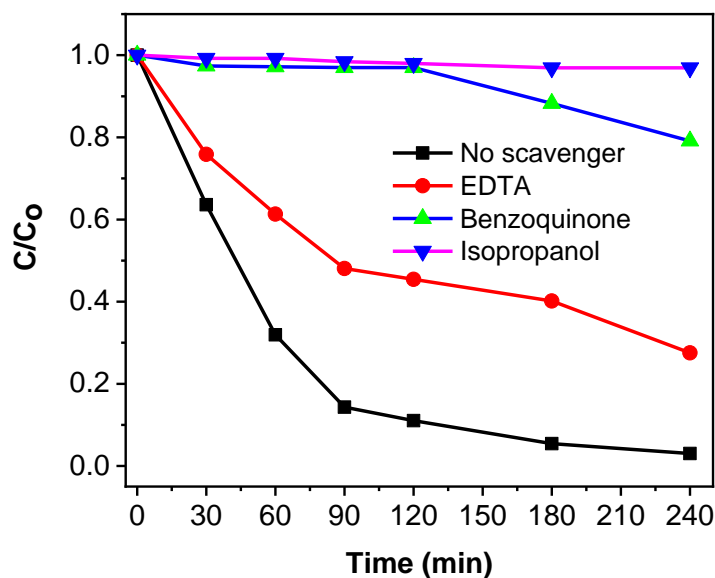
Figure 4-36 Effect of different scavengers/additives on 2,4,6-TCP degradation efficiency of FeOOH/TiO$_2$ (0.14 wt.% Fe).

Conditions: 2,4,6-TCP (50 mg/L, 200 mL, pH$_{nat}$ = 6, catalyst concentration = 0.5 g/L, λ > 320 nm), EDTA (10 mg/L), Benzoquinone (10 mg/L), Isopropanol (10% v/v).

In situ ESR technique was employed to monitor the enhancement in generation of these reactive oxygen species (ROS) with DMPO as spin-trapping agent and results are shown in **Figs. 4-37** and **4-38**. No ESR signals are detected when the reaction is carried out in the dark. Under full arc light irradiation ($\lambda > 320$ nm), the characteristic peaks of DMPO-$^{\cdot}$OH and DMPO-$^{\cdot}O_2^{-}$ adducts could be observed.[155,182,183] There is a significant improvement in the generation of hydroxyl radicals, while generation of superoxide radicals is not enhanced by the optimised FeOOH/TiO$_2$ compared to unmodified TiO$_2$ sample. This indicates that FeOOH enhanced the generation of hydroxyl radicals in the TiO$_2$ composite for complete mineralisation of 2,4,6-TCP.
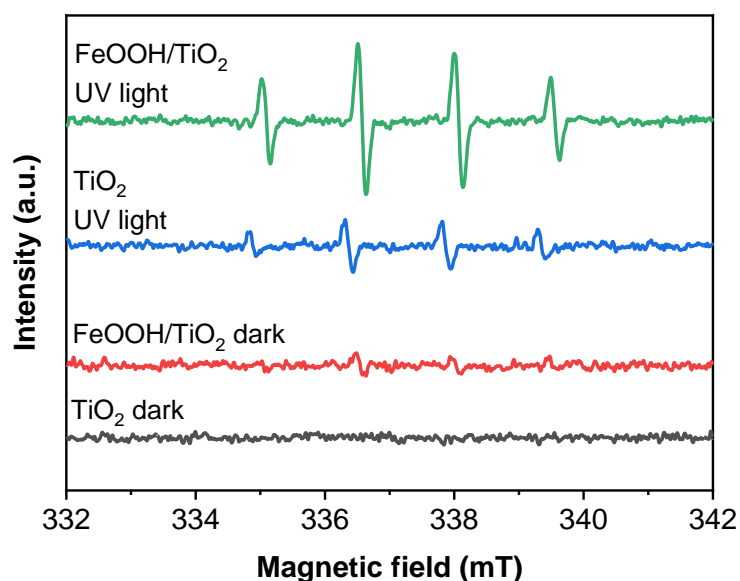
Figure 4-37 DMPO-$^{\cdot}$OH spin-trapping ESR spectra using PC50 TiO$_2$ and FeOOH/TiO$_2$ (0.14 wt.% Fe).

Conditions: 20 µL 20 mM DMPO, 0.5 mg/mL catalyst in aqueous dispersion and under light irradiation ($\lambda > 320$ nm) for 40 secs.
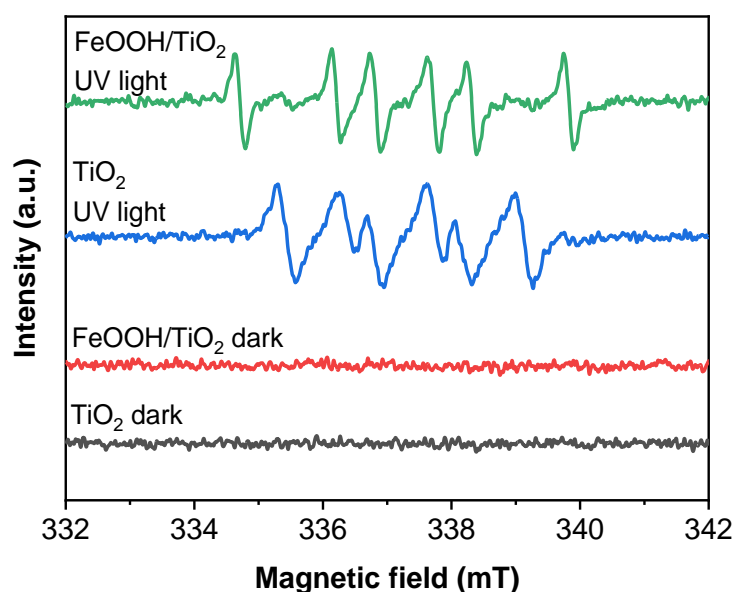
Figure 4-38 DMPO-$\cdot O_2^-$ spin-trapping ESR spectra using PC50 TiO_2 and FeOOH/TiO_2 (0.14 wt.% Fe).

Conditions: 20 μL 20 mM DMPO, 0.5 mg/mL catalyst in methanol dispersion and under light irradiation (λ > 320 nm) for 40 secs.

4.3.5 2,4,6-TCP degradation pathway

During 2,4,6-TCP oxidative degradation, most researchers reported the generation of 2,6-dichloro-1,4-benzoquinone (2,6-DCBQ) as the first intermediate product, which is a light sensitive compound that can easily transform into a mixture of 2,6-dichlorohydroquinone (2,6-DCHQ) and 2,6-dichloro-3-hydroxy-1,4-benzoquinone (2,6-DCHBQ) under light irradiation.[136,184] These intermediate products can be further degraded via

the aromatic ring cleavage[185] and finally mineralised to give small molecules (aliphatic carboxylic acids).[186]

In the project, the degradation intermediates of 2,4,6-TCP were analysed by HPLC in tandem with MS (HPLC-MS) using ESI negative mode. Six intermediate products were detected based on analysis of HPLC chromatograms, corresponding ESI chromatograms and ESI spectra as shown in **Figs. 4-39** to **4-43**. Peak 1 with retention time of 5.1 min in both HPLC and ESI-MS chromatograms (**Fig. 4-39 and 4-40**), and ESI-MS spectra with m/z values at 191, 193 (**Fig. 4-43a**) could be assigned to 2,6-dichloro-3-hydroxy-1,4-benzoquinone (2,6-DCHBQ). Peak 2 with retention time of 5.8 min in both HPLC and ESI-MS chromatograms (**Fig. 4-39 and 4-40**), and ESI-MS spectra with m/z values at 193, 195 (**Fig. 4-43b**) could be assigned to 2,6-dichlorobenzene-1,3,4-triol (2,6-DCBT). Peak 3 with retention time of 7.3 min in both HPLC and ESI-MS chromatograms (**Fig. 4-41 and 4-42**), and ESI-MS spectra with m/z values at 177, 179 (**Fig. 4-43c**) could be assigned to 2,6-dichlorohydroquinone (2,6-DCHQ). Peak 4 with retention time of 9.1 min in both HPLC and ESI-MS chromatograms (**Fig. 4-41 and 4-42**), and ESI-MS spectra with m/z values at 211, 213 (**Fig. 4-43d**) could be assigned to 2,4,6-trichlororesorcinol (2,4,6-TCR). Peak 5 with retention time of 9.3 min in both HPLC and ESI-MS chromatograms (**Fig. 4-41 and 4-42**), and ESI-MS spectra with m/z values at 177, 179 (**Fig. 4-43e**) could be assigned to 3,5-dichlorocatechol (3,5-DCC). Since 2,6-DCHQ and 3,5-DCC have similar m/z values, their assignment is in order of elution time as reported in literature. Peak 6 with retention time of 9.7 min in HPLC

128

chromatogram (**Fig. 4-39**) could be assigned to 2,6-dichloro-1,4-benzoquinone (2,6-DCBQ). This intermediate product could not be detected with ESI-MS technique (**Fig. 4-40**) due to ionisation problems as reported in literature.[187] Finally, peak 7 with retention time of 11.5 min in both HPLC and ESI-MS chromatograms (**Fig. 4-39 and 4-40**), and ESI-MS spectra with m/z values at 195, 197 (**Fig. 4-43f**) could be assigned to the model pollutant under investigation (2,4,6-TCP).
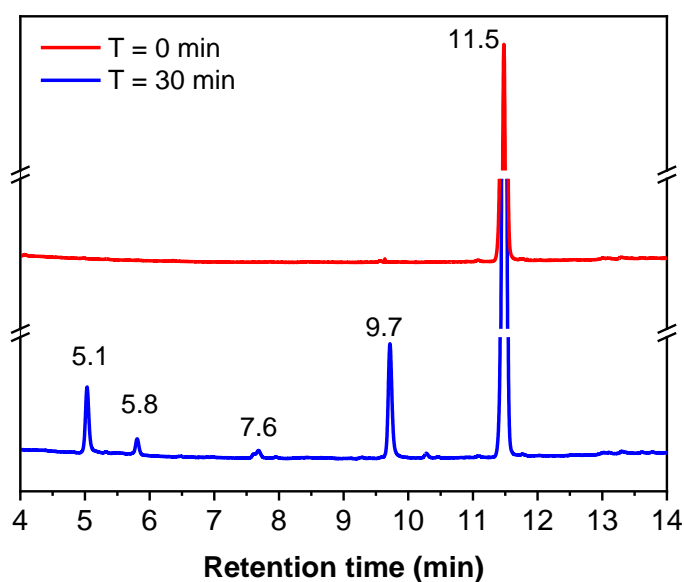
Figure 4-39 HPLC chromatograms showing the degradation of 2,4,6-TCP using FeOOH/TiO$_2$ (0.14 wt.% Fe) within 30 min.
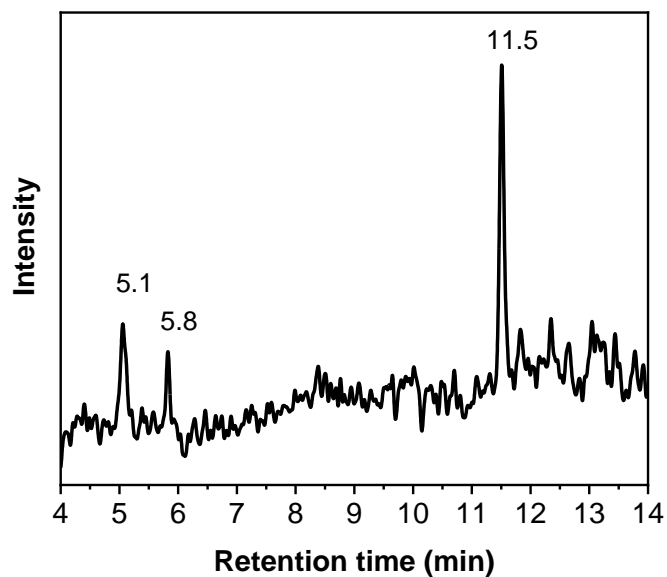
Figure 4-40 Corresponding ESI-MS chromatogram at 30 min.
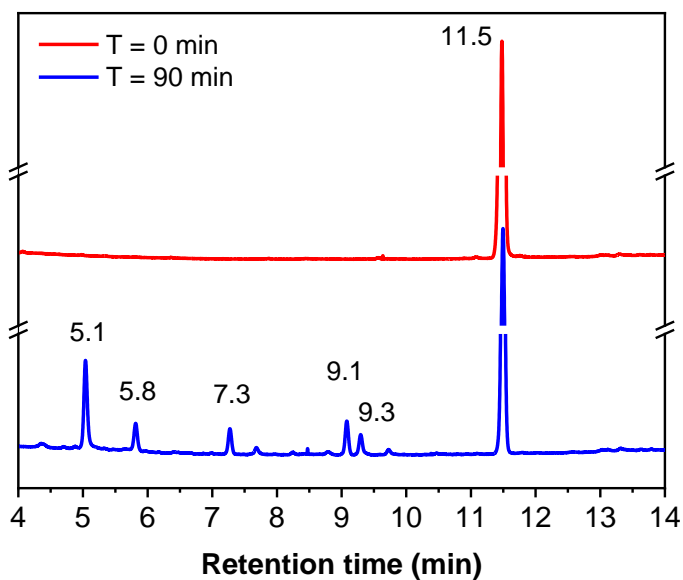
Figure 4-41 HPLC chromatograms showing the degradation of 2,4,6-TCP using FeOOH/TiO$_2$ (0.14 wt.% Fe) within 90 min.
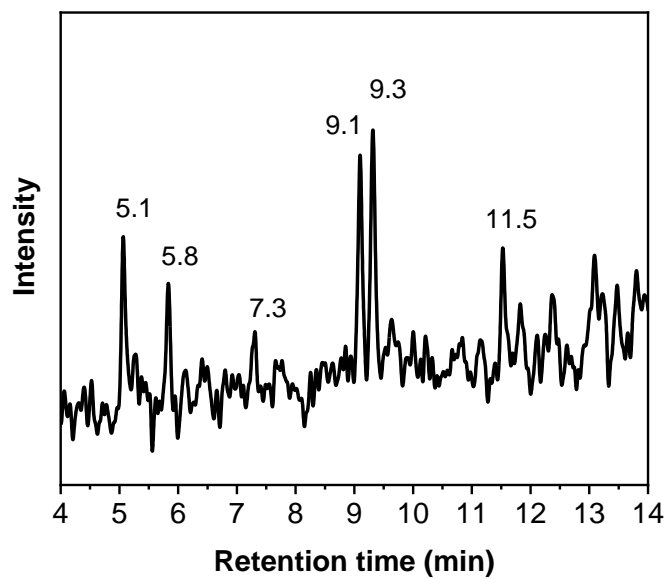
Figure 4-42 Corresponding ESI-MS chromatogram at 90 min.
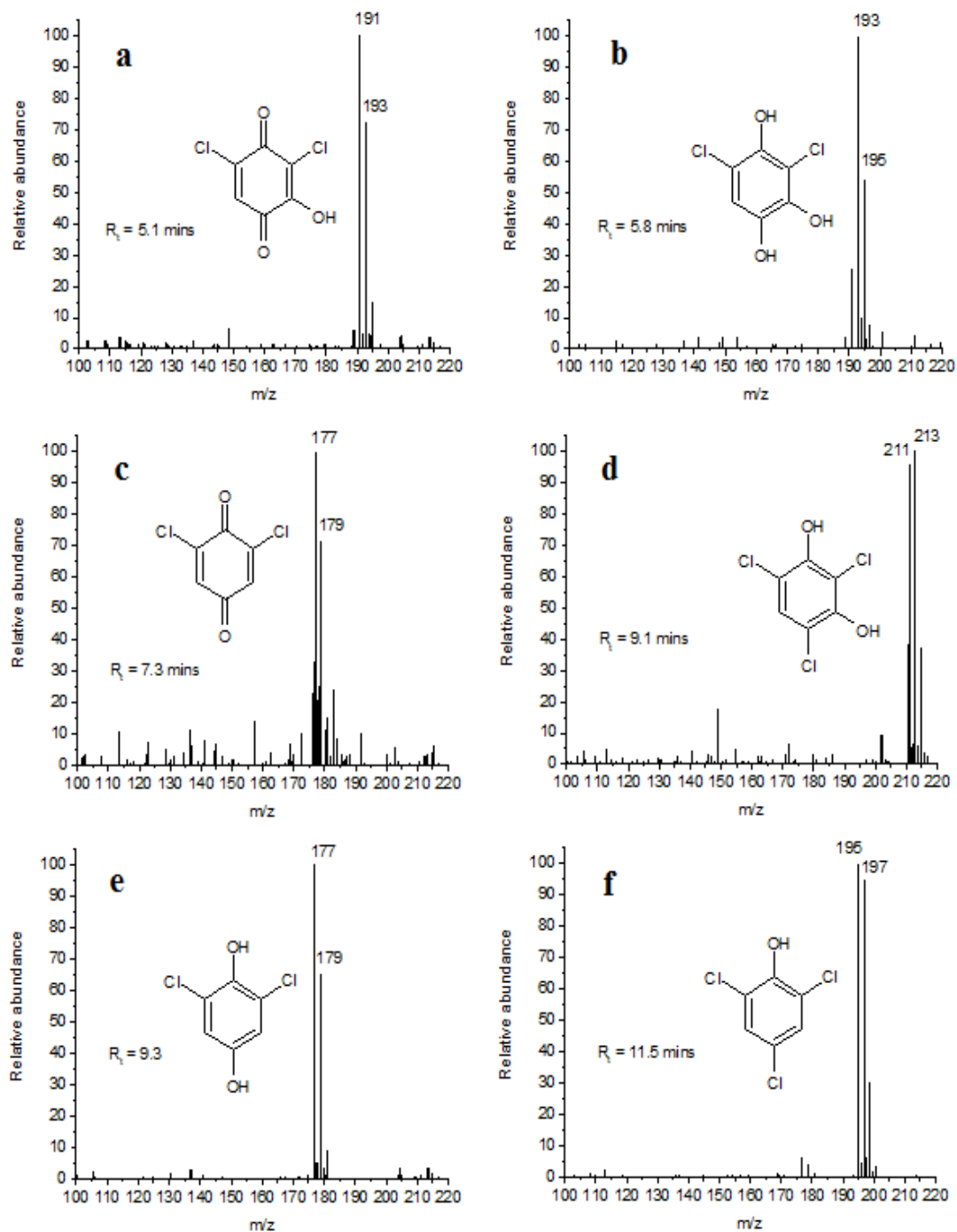
Figure 4-43 (a – f) ESI-MS spectra of detected intermediate products during 2,4,6-TCP degradation.

Based on the detailed HPLC-MS analysis for structural elucidation of the detected intermediate products, the possible pathway for 2,4,6-TCP degradation and intermediates formation is shown in **Fig. 4-44**. This is consistent with the order in which the intermediate products were detected regarding reaction time as shown in **Figs. 4-39** and **4-41**. Furthermore, it is well similar to reported degradation pathway for 2,4,6-TCP in the literature.[136,187]
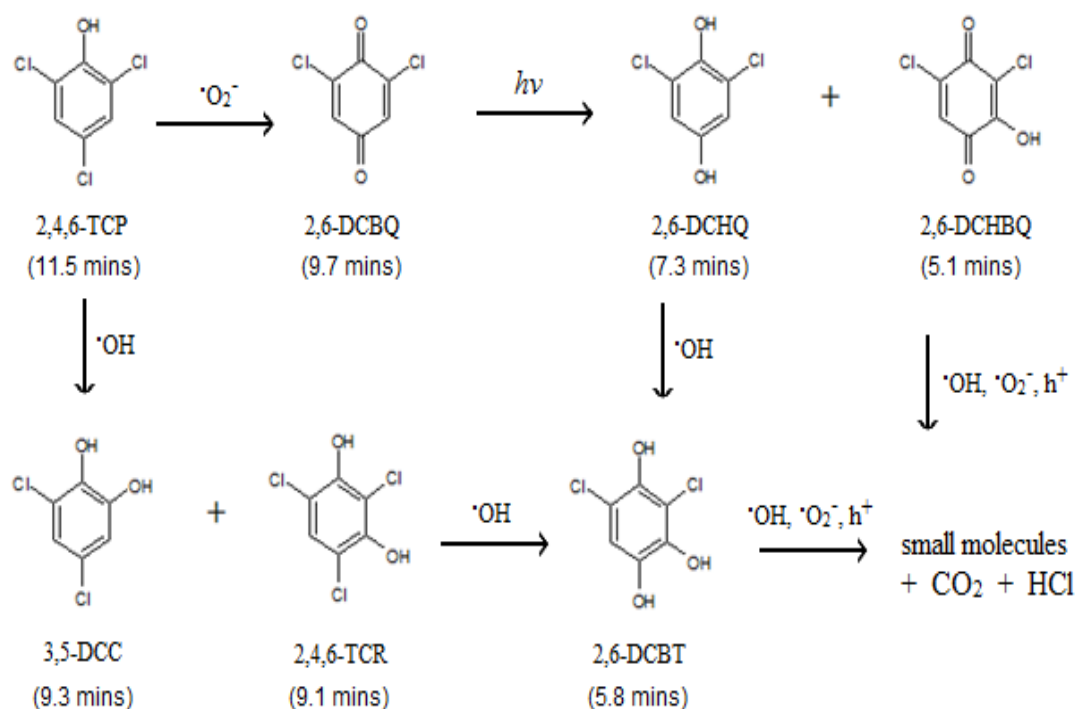
Figure 4-44 Proposed reaction scheme for 2,4,6-TCP degradation.

4.3.6 2,4,6-TCP degradation mechanism

The 2,4,6-TCP degradation mechanism by FeOOH/TiO$_2$ is illustrated in **Fig. 4-45**. When the photocatalyst is exposed to light, photo-generated electrons are excited from the valence band (VB) to the conduction band (CB) of TiO$_2$. The VB holes are transferred to the surface FeOOH sites and subsequently react with hydroxyl ions (OH$^-$) in water to produce OH radicals, which oxidises 2,4,6-TCP to intermediate products before its mineralisation. The 2,4,6-TCP degradation mechanism by Fe$_2$O$_3$/TiO$_2$ is illustrated in **Fig. 4-46.** This involves the transfer of electrons (generated in TiO$_2$) to the Fe$_2$O$_3$ conduction band for oxygen reduction reaction.[23] When Fe$_2$O$_3$ content is dominating over FeOOH, such as in the 0.14 wt.% Fe/TiO$_2$ (450 °C) sample, part of the Fe$_2$O$_3$ sites may become electron-hole recombination centers, leading to poor photocatalytic activity.[171] The photocatalytic degradation of 2,4,6-TCP on bare FeOOH is quite negligible, and the poor photocatalytic activity of FeOOH/TiO$_2$ (2.8 wt.% Fe) is observed compared to unmodified TiO$_2$ (**Figs. 4-15** and **4-26**). Although there is visible light absorption originating from FeOOH (**Fig. 4-3**), FeOOH cannot be regarded as a good photocatalyst for the degradation of 2,4,6-TCP.
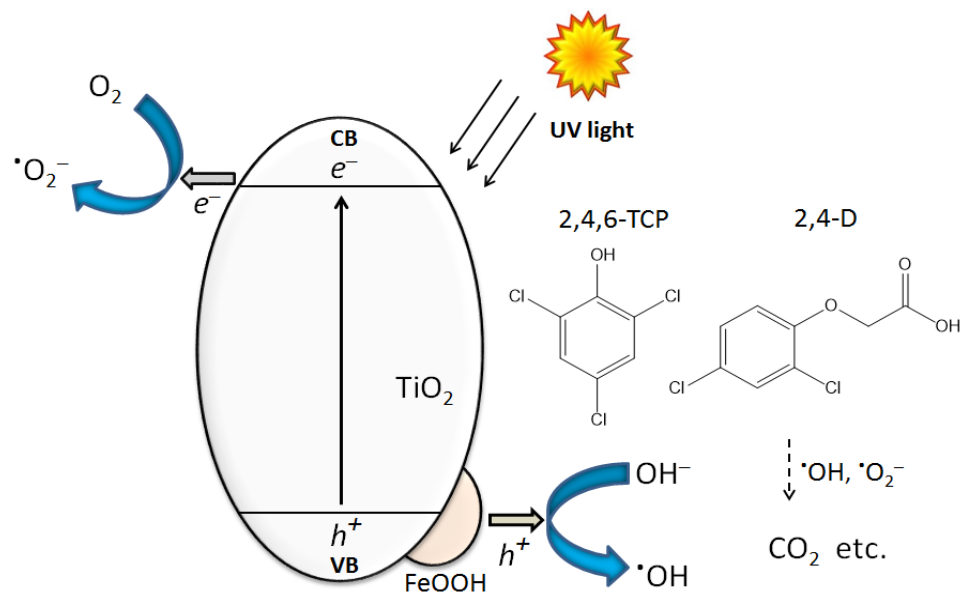
Figure 4-45 Proposed mechanism for major charge transfer pathways on FeOOH/TiO$_2$ for mineralisation of 2,4,6-TCP and 2,4-D.
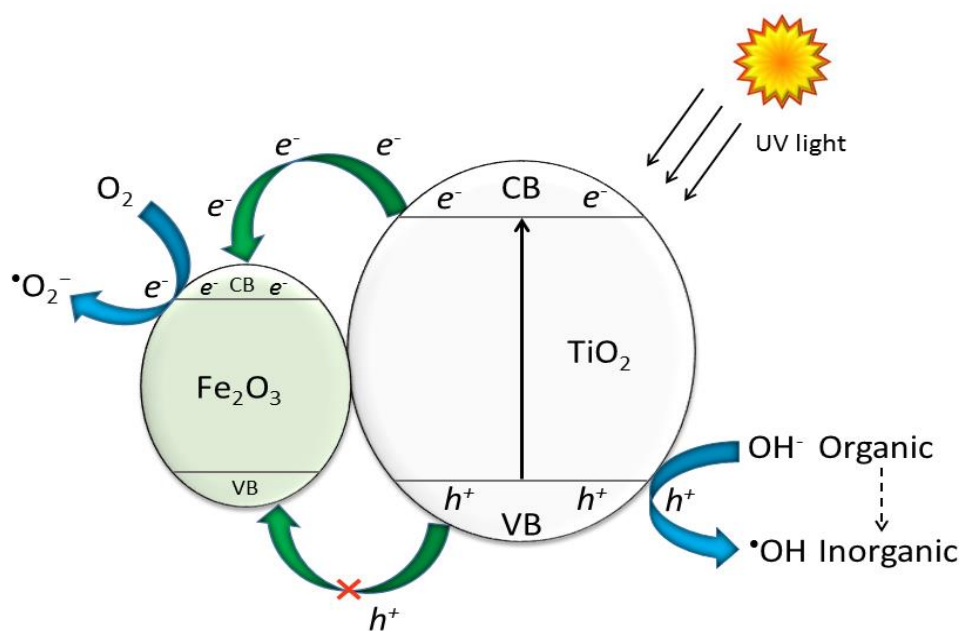
Figure 4-46 Proposed mechanism for major charge transfer pathways on Fe$_2$O$_3$/TiO$_2$ for mineralisation of 2,4,6-TCP and 2,4-D.

4.4   Conclusion

In summary, facile and robust synthesis procedure was successfully used in decorating PC50 TiO_2 nanoparticles with highly dispersed FeOOH, which plays a key role for efficient photocatalytic herbicide decomposition. The Fe loading and properties in the composites were thoroughly controlled by varying the Fe concentrations from 0.07 to 2.8 wt.% Fe and calcination temperatures from 120 to 450 ^oC, respectively. At 120 ^oC, iron nitrate hydroxyl impurities and FeOOH were impregnated on surface of TiO_2. FeOOH nanoparticles were the only decorating species at 250 ^oC, while at temperatures higher than 250 °C, Fe_2O_3 species dominated.

The highest photocatalytic 2,4,6-TCP mineralisation efficiency was achieved with the composite (0.14 wt.% Fe/TiO_2) calcined at 120 ^oC, which is more than two times higher than the unmodified PC50 TiO_2, indicating that the $Fe_4NO_3(OH)_{11}$ impurities could aid FeOOH/TiO_2 towards 2,4,6-TCP degradation. The sample calcined at 250 ^oC (FeOOH/TiO_2) displayed both excellent photocatalytic mineralisation efficiency (nearly double activity of PC50) and better photocatalytic stability after three successive degradation cycles than the 120 ^oC calcined sample. About 100% TOC removal was also achieved in 3 h during the photocatalytic mineralisation of other herbicide 2,4-D by optimised FeOOH/TiO_2 sample. The widely reported Fe_2O_3 decorated TiO_2 sample exhibited worse performances than that decorated by FeOOH. The enhanced photo-generated electron-hole separation and the catalytic effect of FeOOH on TiO_2, for enhanced

generation of hydroxyl radicals, led to high photocatalytic degradation performance. The mechanistic studies demonstrate that the degradation of the herbicides was primarily controlled by hydroxyl radicals and superoxide radicals. Overall, this work is of importance in the fabrication of low-cost, efficient and robust photocatalysts for water treatment.

The next chapter will focus on further optimisation of the $FeOOH/TiO_2$ nanocomposite by preparing earth-abundant binary cocatalyst alloys (FeOx-CuOx and FeOx-CoOx) on TiO_2 surface for complete mineralisation of 2,4,6-TCP and other herbicides under similar operating conditions.

5 Bimetallic FeO_x-MO_x loaded TiO_2 (M = Cu, Co) nanocomposite photocatalysts for complete mineralisation of herbicides

5.1 Introduction

Based on the results of Chapter 4, FeOOH with a concentration of 0.14 wt.% Fe was approved to be the optimised condition. This chapter presents the use of novel nano-architecture comprising binary metal oxides/hydroxides as cheap/earth-abundant cocatalysts on PC50 (commercial anatase TiO_2), in which 0.1 wt.% Fe was the major component. The Fe(III), Cu(II) and Co(II) species were characterised in order to clarify their individual functionality and actual active species. Due to the low signal-to-noise ratio obtained during characterisation of optimised nanocomposite photocatalysts with 0.1 wt.% cocatalyst loading, only the 0.5 wt.% cocatalyst decorated samples were comprehensively characterised. The photocatalytic degradation of 2,4,6-TCP and 2,4-D in water were carried out under UV/Vis light irradiation. The effects of single cocatalysts, dual cocatalyst coupling containing FeOOH (denoted as FeOx in this chapter), nature of herbicide and light wavelength were investigated. Photocatalytic mineralisation ability of the optimised catalyst was also evaluated with other widely used herbicides, 2,4-dichlorophenol (2,4-DCP) and 2,4,5-trichlorophenoxyacetic acid (2,4,5-T) to demonstrate its wide feasibility. The charge transfer mechanism was also discussed.

5.2 Experimental section

5.2.1 Chemicals

PC50 TiO_2 (purely anatase) was purchased from Millennium chemicals. 2,4,6-TCP (98%) was purchased from Alfa Aesar. 2,4-D was purchased from Cayman Chemical Company. 2,4-DCP (99%) and coumarin were purchased from Acros Organics. 2,4,5-T, $Fe(NO_3)_3.9H_2O$, $Cu(NO_3)_2.2.5H_2O$ and $Co(NO_3)_2.6H_2O$ were purchased from Sigma-Aldrich. Isopropanol (HPLC grade) and Acetonitrile (HPLC grade) were purchased from Fischer Scientific. All reagents were used as received without further purification.

5.2.2 Fabrication of photocatalysts

A modified surface impregnation and drying technique was used to prepare dual cocatalyst-decorated TiO_2 composites.[128,135] In a typical experiment,[135] the appropriate percentage weight of the nitrate precursors of Fe(III), Cu(II) and Co(II) was separately added to an aqueous suspension of 1.0 g of commercial PC50 TiO_2 under mild stirring, with M/TiO_2 composition (M is the metal with a weight percentage of 0.05, 0.1 and 0.5, respectively). The cocatalyst concentration was narrowed to between 0.05 and 0.5 wt.% based on previous results in Chapter 4 and performances of similar cocatalyst-decorated TiO_2 in literature.[128,135,188] The obtained slurry was continuously stirred with a magnetic stirrer bar and dried slowly at 80 ^{o}C on a hotplate. The resultant dried powder was hand-milled and calcined in a muffle furnace under air atmosphere at 250 ^{o}C for 4 hours. It was collected after cooling down to room temperature, washed, dried and hand-milled again,

and stored for photocatalytic activity tests and characterisations. Subsequent studies on dual cocatalyst coupling (FeOx-CuOx/TiO$_2$ and FeOx-CoOx/TiO$_2$) were evaluated using optimum cocatalyst loading (0.1 wt.% for each of the three cocatalysts), followed by a study on the photocatalytic performance of optimised FeOx-CoOx/TiO$_2$photocatalyst for the mineralisation of four herbicides (2,4-DCP, 2,4,6-TCP, 2,4-D and 2,4,5-T), individually under similar operating conditions.

5.2.3 Characterisation

High resolution XPS was performed by a Thermo Scientific K-alpha/NEXSA photoelectron spectrometer using monochromatic Al kα radiation (1486.6 eV); peak positions were calibrated to carbon (C 1s = 284.5 eV) and plotted using the CasaXPS software. UV-vis absorption spectra measurements of powdered samples were performed using a Shimadzu UV-2550 spectrophotometer fitted with an integrating sphere. Hydroxyl radicals generated were quantified using aqueous coumarin solution and Shimadzu RF-6000 Spectrofluorometer.

5.2.4 Photocatalytic activity test

A 300 W Xe lamp (Newport) was used as the light source with a plain glass window (λ > 320 nm) as a cut-off filter. In a typical measurement,[135] similar to that used in Chapter 4, 0.1 g of photocatalyst was dispersed in 200 mL 50 mg/L aqueous solution of 2,4,6-TCP at natural solution pH of 6 or 200 mL 25 mg/L aqueous solution of 2,4-D at natural solution pH of 4 in D.I. water. The suspension was sonicated in an ultrasonic water-bath for 15 min and

then magnetically stirred in the dark for 1 h to achieve adsorption/desorption equilibrium of organic pollutant molecules on the photocatalyst. Thereafter, the suspension was irradiated with UV/visible light under continuous magnetic stirring for 3 h, while the reaction vessel was immersed in a water-bath to regulate temperature (T ≤ 30 ^{o}C). The distance between the lamp head and the top of the solution was also maintained at 8 cm to achieve similar light intensities. Upon light irradiation, a 3 mL sample portion was taken from the bottom of the suspension at regular time intervals and filtered through a micropore syringe filter (PTFE, 0.2 μm) before further analysis.

Similar experimental setup was used in the control test (photolysis) for 3 h. However, photolysis of 2,4,6-TCP and 2,4-D were carried out without photocatalyst and sonication. Stability test was carried out on the best sample under similar operational conditions during photocatalytic 2,4,6-TCP mineralisation experiments, except for the increase in amount of photocatalyst powder to 0.5 g and light irradiation (λ > 260 nm). The cycle tests were performed at two hours intervals. The photocatalyst was recovered from solution via centrifugation method and re-used immediately for subsequent cycles without any pre-treatment or make-up.

Further studies with the best cocatalyst-decorated TiO$_2$ sample were carried out using 25 mg/L 200 mL solution of four (4) different herbicides: 2,4,6-TCP, 2,4-DCP, 2,4-D and 2,4,5-T. The four herbicides were tested individually and not mixed.

5.2.5   Activity analysis

The change in herbicide concentration was measured using HPLC (LC-2030C, Shimadzu) consisting of a binary pump, an autosampler, a PDA detector and an ACE-5 C18 (5μm × 150 mm × 4.6 mm) reverse phase column maintained at 40 $^{\circ}$C. The HPLC used a 5–95% gradient (Acetonitrile/H_2O with 0.1% formic acid) as the mobile phase. A UV-vis spectrophotometer was also used to monitor herbicides degradation with the optimised sample. The further herbicides mineralisation by photocatalysis was investigated primarily using a Shimadzu TOC-L analyser.

5.3   Results and discussion

5.3.1   Materials characterisations

The absorption spectra of PC50 TiO_2 and some as-prepared cocatalyst-decorated TiO_2 nanocomposites are shown in **Fig. 5-1**. Since the PC50 TiO_2 is white in colour, it does not show any absorption in the visible region. On the other hand, iron oxide-modified PC50 TiO_2 samples have light-yellow colour that indicates the presence of Fe (III) oxide species,[128,171] which becomes reddish-brown with increase in FeO_x loading. The cobalt oxide-modified PC50 TiO_2 samples have olive-green or gray colour that indicates the presence of CoO,[189] which also becomes darker with increase in CoO loading. The copper oxide-modified PC50 TiO_2 samples have light blue-green colour, indicating the presence of CuO,[190] which also becomes grey and finally black with increase in CuO loading.
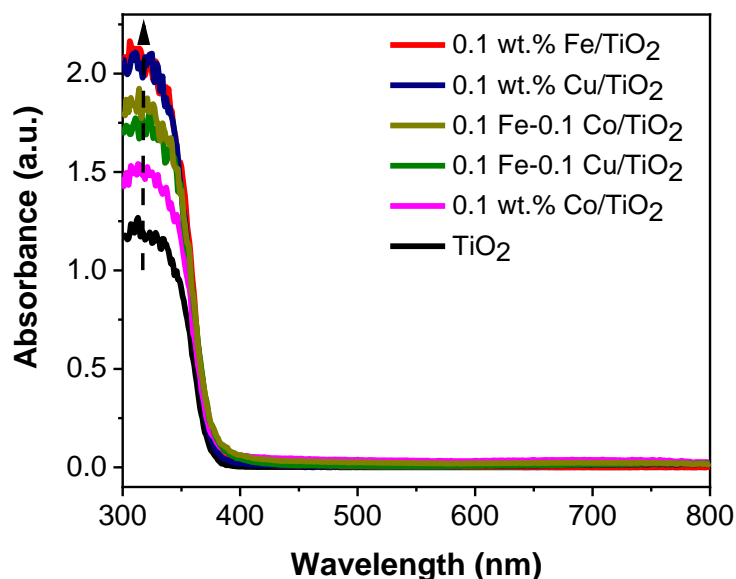
Figure 5-1 UV/vis absorption spectra of some prepared cocatalyst-decorated PC50 TiO_2 catalysts.

High resolution XPS was used to identify the Fe, Cu and Co oxide species present in the FeO_x-CuO_x/TiO_2 and FeO_x-CoO_x/TiO_2 samples. Fe 2p, Cu 2p and Co 2p peaks are not clearly observed in the full XPS survey spectrum of both samples (**Fig. 5-2**), which is likely due to the low amount of cocatalysts loading and high dispersion on TiO_2 surface.[188,189] From the deconvulated high resolution Cu 2p XPS spectrum of FeO_x-CuO_x/TiO_2 in **Fig. 5-3**, peaks corresponding to Cu^{2+} are confirmed at 934 eV (Cu $2p_{3/2}$) and 954 eV (Cu $2p_{1/2}$).[191,192] A satellite peak characteristic of the presence of Cu^{2+} is clearly observed between 939–945 eV.[191] Apart from the Cu^{2+} satellite, the peak at binding energy of 931.6 eV is assigned to Cu/Cu^+.[192,193] However, it is difficult to differentiate between Cu_2O and Cu metal from the Cu 2p XPS peaks as their binding energies are too close and it is also

difficult to identify them by other techniques due to very low amount loaded.[193,194]
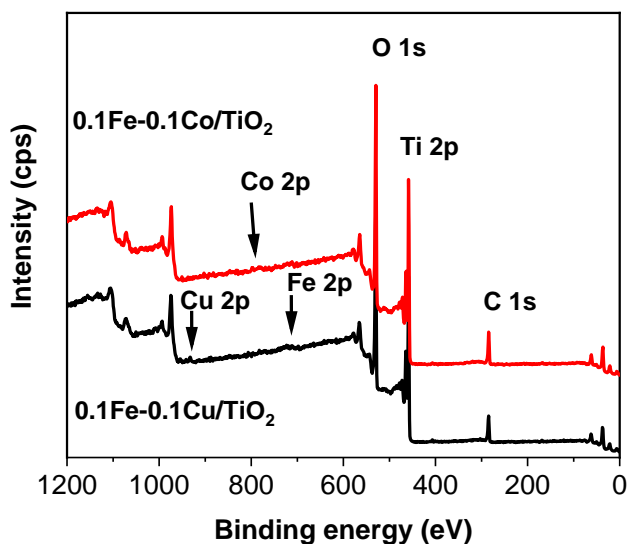
Figure 5-2 Full XPS survey spectra of FeOx-CuOx/TiO$_2$ and FeOx-CoOx/TiO$_2$ samples with optimum cocatalyst loading (0.1 wt.% for each metal).
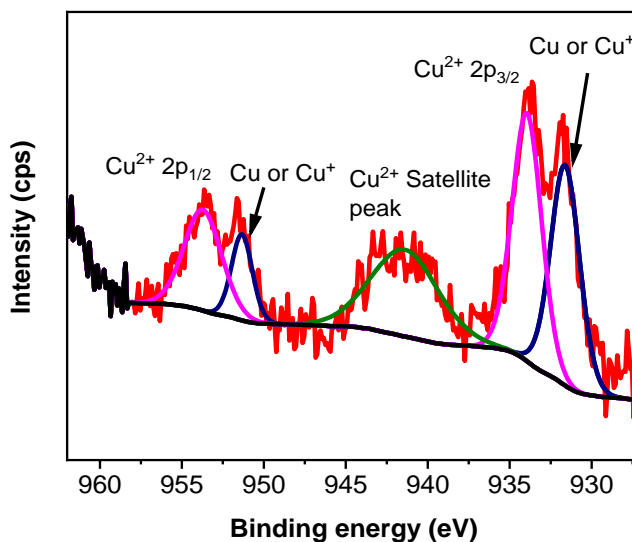
Figure 5-3 High resolution Cu 2p XPS spectra of FeOx-CuOx/TiO$_2$ sample with optimum Cu loading (0.1 wt.% Cu and 0.1 wt.% Fe).

The Co 2p XPS spectrum of FeOx-CoOx/TiO$_2$ is of weak intensity due to low Co concentration in the sample as shown in **Fig. 5-4**. Based on the high resolution deconvulated Co 2p XPS spectrum of FeOx-CoOx/TiO$_2$ (with high Co loading, 0.5 wt.%) in **Fig. 5-5**, peaks corresponding to Co^{2+} are confirmed at 781 eV (Co 2p$_{3/2}$) and 796 eV (Co 2p$_{1/2}$).[192,195] The shake-up satellite features of Co^{2+} at 787 eV and 802 eV are very strong in intensity, which rules out the presence of Co^{3+}, whose satellite features are very weak in intensity at similar binding energies.[196,197]
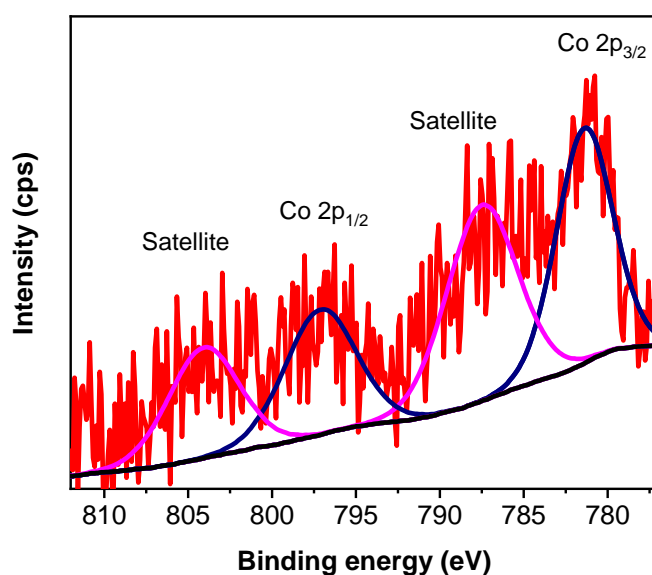
Figure 5-4 High resolution Co 2p XPS spectra of FeOx-CoOx/TiO$_2$ sample with optimum Co loading (0.1 wt.% Co and 0.1 wt.% Fe).
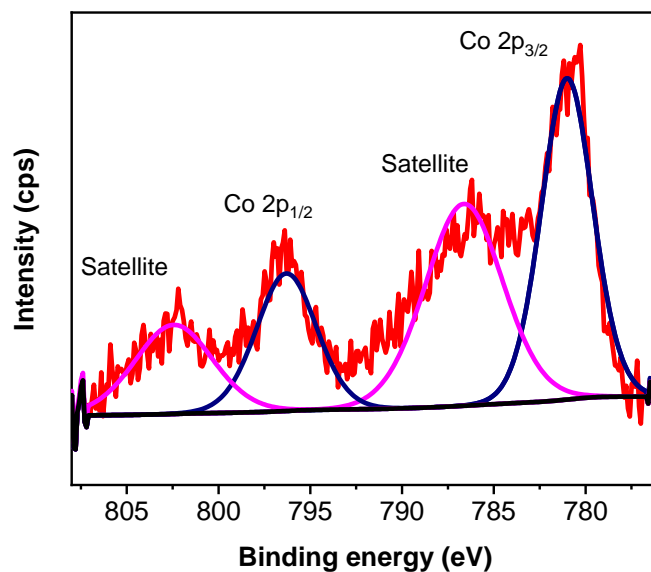
Figure 5-5 High resolution Co 2p XPS spectra of FeOx-CoOx/TiO$_2$ sample with high Co loading (0.5 wt.% Co and 0.5 wt.% Fe).

Also, the high resolution Fe 2p XPS spectrum of FeOx-CoOx/TiO$_2$ is of weak intensity due to low Fe concentration in the sample as shown in **Fig. 5-6**. Based on the deconvulated high resolution Fe 2p XPS spectrum of FeOx-CoOx/TiO$_2$ (with high Fe loading, 0.5 wt.%) in **Fig. 5-7**, peaks corresponding to Fe^{3+} are confirmed at 710 eV (Fe 2p$_{3/2}$) and 724 eV (Fe 2p$_{1/2}$).[23,192,198,199] The satellite peaks at 719 eV and 733 eV are associated with the fingerprint of Fe(III) oxidation state.[198,199] The extra peaks at 713 eV and 728 eV are related to the influence of hydroxide groups.[198,199] Absence of a peak at 709 eV rules out the presence of Fe^{2+} in the sample.[23,165]
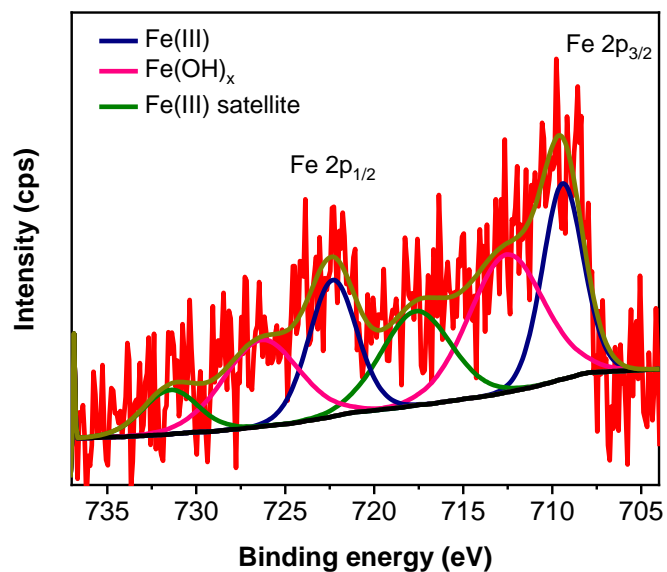
Figure 5-6 High resolution Fe 2p XPS spectra of FeOx-CoOx/TiO$_2$ sample with optimum Fe loading (0.1 wt.% Fe and 0.1 wt.% Co).
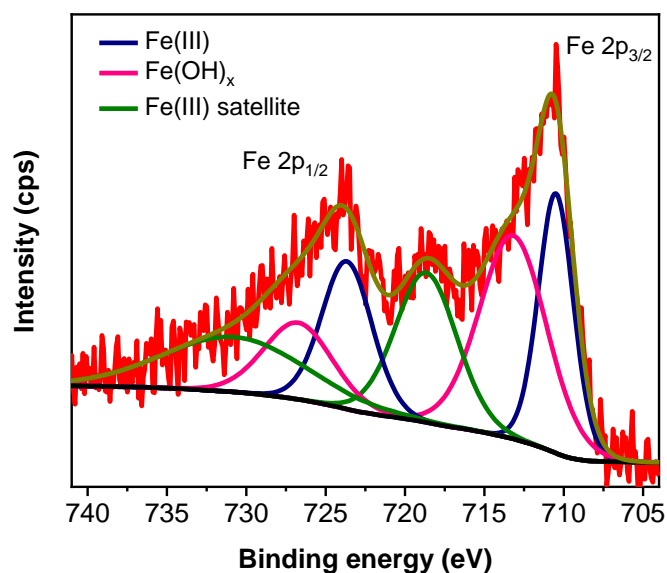
Figure 5-7 High resolution Fe 2p XPS spectra of FeOx-CoOx/TiO$_2$ sample with high Fe loading (0.5 wt.% Fe and 0.5 wt.% Co).

Based on the high resolution Ti 2p XPS spectra of TiO_2, $FeOx/TiO_2$, FeOx-$CuOx/TiO_2$ and FeOx-$CoOx/TiO_2$ in **Fig. 5-8**, peaks corresponding to Ti^{4+} are confirmed around 458 eV (Ti $2p_{3/2}$) and 464 eV (Ti $2p_{1/2}$).[23,191] A slight peak shift to lower energy is observed with $FeOx/TiO_2$, while a slight shift to higher energy is observed with FeOx-$CuOx/TiO_2$ and FeOx-$CoOx/TiO_2$ compared to pristine TiO_2. The observation suggests that there is a form of interaction between TiO_2 and the cocatalysts, which is neither Ti^{4+} reduction nor oxidation.[198]
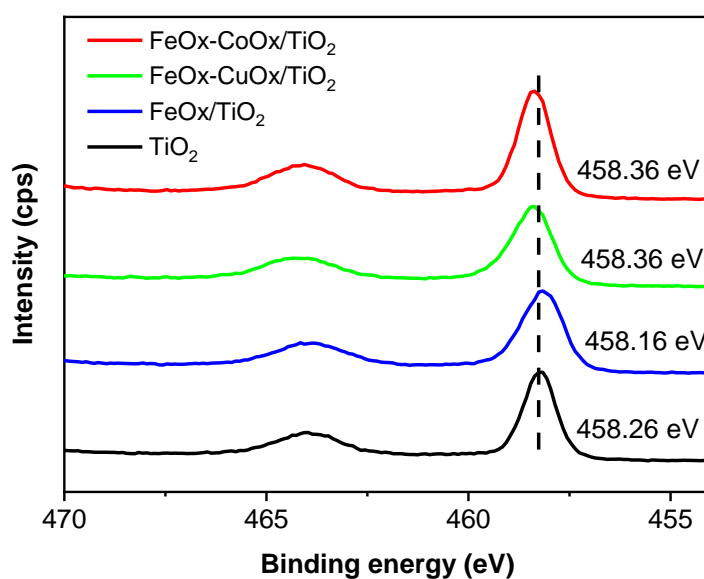
Figure 5-8 High resolution Ti 2p XPS spectra of metal-loaded TiO_2.

5.3.2 Photocatalytic mineralisation of herbicides

First, the control experiment was carried out with only 2,4,6-TCP solution in the absence of photocatalyst. Virtually 0% TOC removal is observed after 3 h of light irradiation as shown in **Fig. 5-9**. Photocatalytic activities of the as-prepared mono and dual cocatalyst-decorated TiO_2 composites were then evaluated by the mineralisation of 2,4,6-TCP under full arc light irradiation (λ > 320 nm). The 2,4,6-TCP mineralisation rate recorded by PC50 TiO_2 is nearly 35% after 3 hours. Approximately 52% TOC removal is achieved with the 0.05 wt.% Fe/TiO_2 sample after 3 h. An increase in Fe concentration up to 0.1 wt.% Fe leads to a further increase in photocatalytic activity, while lower 2,4,6-TCP mineralisation rate is observed with 0.5 wt.% Fe-loaded sample. The optimum condition for the preparation of FeOx/TiO_2 nanocomposites is found to be 0.1 wt.% Fe with ca. 62% TOC removal after 3 h, similar to the optimised 0.14 wt.% FeOOH/TiO_2 sample in Chapter 4 and reported optimum Fe loading (0.13 wt.%) in Fe/TiO_2, prepared using similar method for 4-CP degradation in literature.[128] Similar trends were observed for Co and Cu concentrations as shown in **Fig. 5-10** and **Fig. 5-11**. The optimum condition for the preparation of CuOx/TiO_2 and CoOx/TiO_2 nanocomposites are found also to be 0.1 wt.% Cu and 0.1 wt.% Co, with about 73% and 64% TOC removal after 3 h, respectively. The optimium Cu loading is also similar to reported optimum Cu loading (0.12 wt.%) in Cu/TiO_2, prepared using similar method for 4-CP degradation in literature.[128] For the mono cocatalyst-loaded TiO_2 samples, the order of photocatalyst activity is: CuOx > CoOx $\approx$ FeOx.
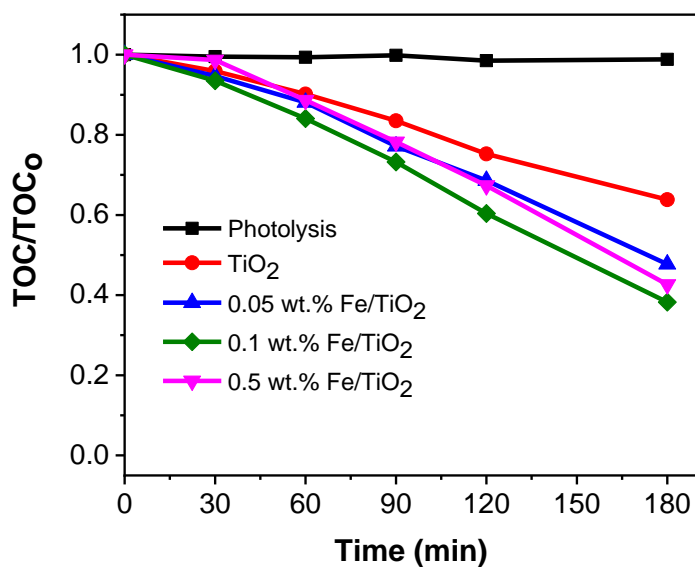
Figure 5-9 Mineralisation profiles of 2,4,6-TCP using FeOx/TiO$_2$ with different Fe loading and control experiment.

Conditions: 2,4,6-TCP (50 mg/L, 200 mL, pH$_{nat}$ = 6, catalyst concentration = 0.5 g/L, λ > 320 nm).
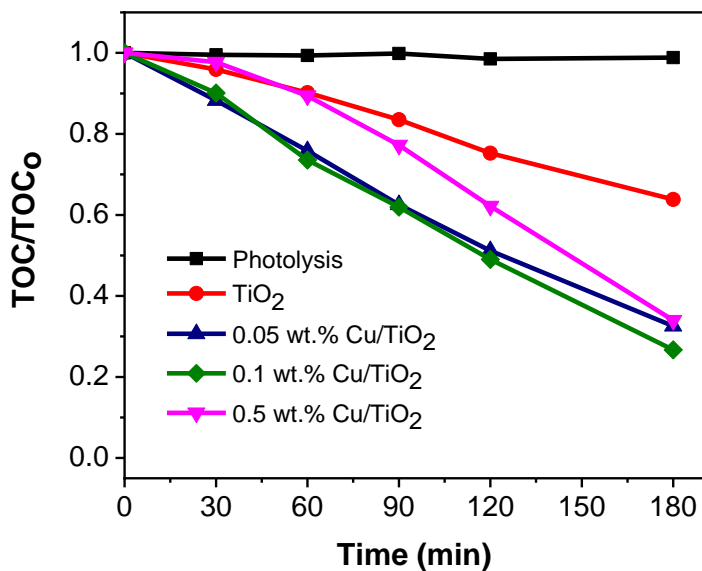
Figure 5-10 Mineralisation profiles of 2,4,6-TCP using CuOx/TiO$_2$ with different Cu loading and control experiment.

Conditions: 2,4,6-TCP (50 mg/L, 200 mL, pH$_{nat}$ = 6, catalyst concentration = 0.5 g/L, λ > 320 nm).
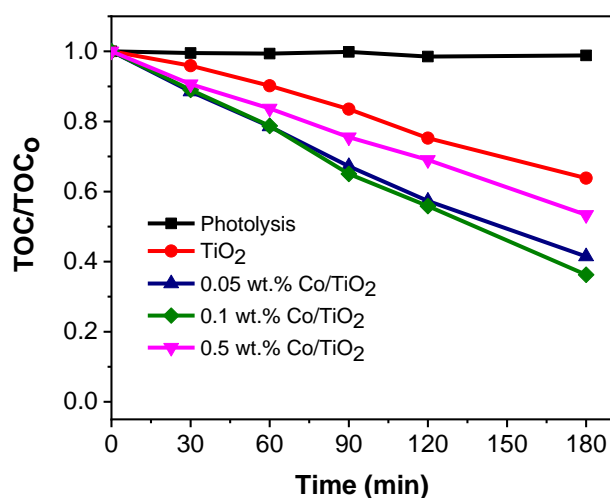
Figure 5-11 Mineralisation profiles of 2,4,6-TCP using CoO_x/TiO_2 with different Co loading and control experiment.

Conditions: 2,4,6-TCP (50 mg/L, 200 mL, pH_{nat} = 6, catalyst concentration = 0.5 g/L, λ > 320 nm).

Next, the effect of dual cocatalyst loading, e.g. FeO_x-CuO_x and FeO_x-CoO_x was investigated based on optimum loading amount for individual cocatalyst (0.1 wt.%). A graphical summary showing the influence of CuO_x on pristine TiO_2 and FeO_x/TiO_2 is displayed in **Fig. 5-12**. The presence of CuO_x enhances the photocatalytic activity of both samples. About 73% and 75% TOC removal in 3 h are recorded with CuO_x/TiO_2 and FeO_x-CuO_x/TiO_2 samples, respectively for 2,4,6-TCP decomposition. A graphical summary showing the influence of CoO_x on pristine TiO_2 and FeO_x/TiO_2 is displayed in **Fig. 5-13**. CoO_x also enhances the photocatalytic activity of both samples as observed with CuO_x. However, there is a remarkable enhancement in 2,4,6-TCP mineralisation efficiency with the FeO_x-CoO_x/TiO_2 sample as it records about 92% TOC removal in 3 h.

Figure 5-12 Mineralisation profiles of 2,4,6-TCP on different cocatalysts, including CuOx as second cocatalyst.

Conditions: 2,4,6-TCP (50 mg/L, 200 mL, pH_{nat} = 6, catalyst concentration = 0.5 g/L, λ > 320 nm).
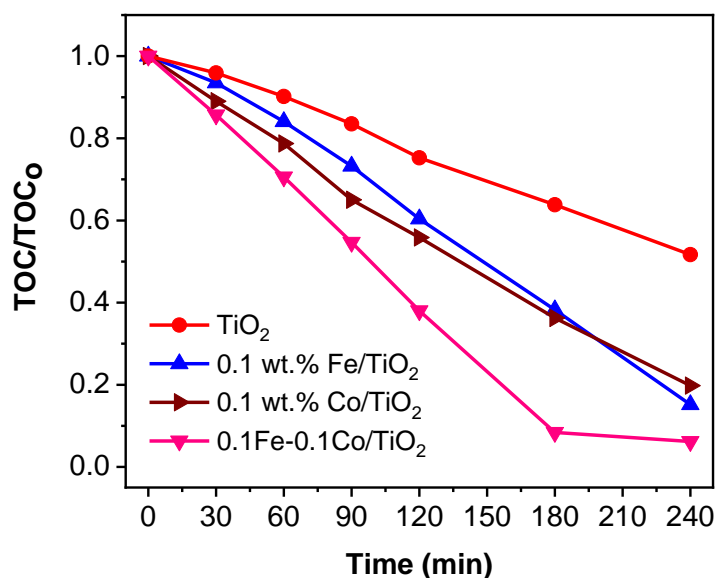
Figure 5-13 Mineralisation profiles of 2,4,6-TCP on different cocatalysts, including CoOx as second cocatalyst.

Conditions: 2,4,6-TCP (50 mg/L, 200 mL, pH_{nat} = 6, catalyst concentration = 0.5 g/L, λ > 320 nm).

The influence of CuOx and CoOx on FeOx/TiO$_2$ is clearly compared in **Fig. 5-14**. The photocatalytic 2,4,6-TCP mineralisation efficiencies in 3 h follow the order: TiO$_2$ (36%) < FeOx/TiO$_2$ (62%) < FeOx-CuOx/TiO$_2$ (75%) < FeOx-CoOx/TiO$_2$ (92%). The significant improvement in 2,4,6-TCP mineralisation efficiency by FeOx-CoOx compared to FeOx-CuOx as bi-cocatalysts, as shown in **Fig. 5-14**, is likely due to a high synergistic effect between FeOx and CoOx as good oxidation cocatalysts,[135,188] thus resulting in improved electron/hole charge separation and generation of hydroxyl radicals for 2,4,6-TCP mineralisation.
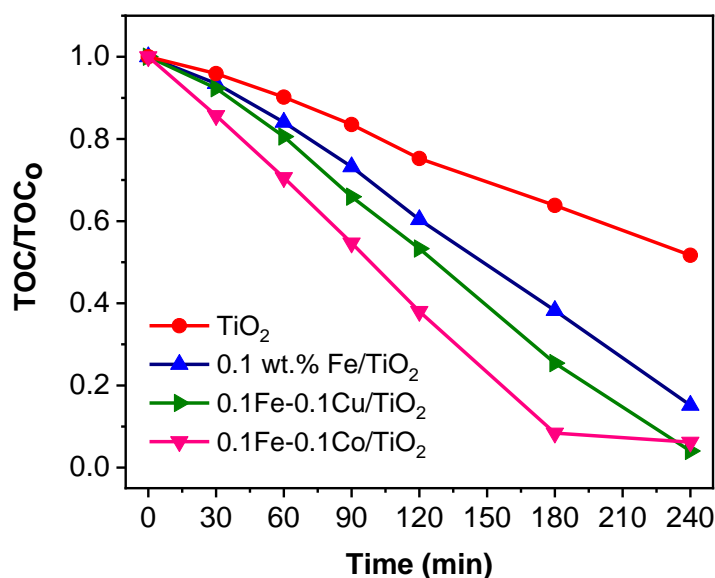
Figure 5-14 Mineralisation profiles of 2,4,6-TCP when using FeOx as primary cocatalyst and CuOx or CoOx as a second cocatalyst.

Conditions: 2,4,6-TCP (50 mg/L, 200 mL, pH$_{nat}$ = 6, catalyst concentration = 0.5 g/L, λ > 320 nm).

Fig. 5-15 shows the 2,4,6-TCP degradation rates with TiO_2, $FeOx/TiO_2$, $FeOx$-$CuOx/TiO_2$ and $FeOx$-$CoOx/TiO_2$ from HPLC measurements. The 2,4,6-TCP degradation rates well agree with the 2,4,6-TCP mineralisation rates, with the exception of $FeOx$-$CuOx/TiO_2$, as it performed less than $FeOx/TiO_2$ in the first 90 minutes. The photocatalytic 2,4,6-TCP degradation efficiencies in 180 minutes follow the order: TiO_2 (71%) < $FeOx/TiO_2$ (95%) < $FeOx$-$CuOx/TiO_2$ (99%) < $FeOx$-$CoOx/TiO_2$ (100%). The 2,4,6-TCP degradation process (monitored by HPLC) is very fast over FeOx, FeOx-CuOx and FeOx-CoOx-decorated TiO_2 samples, since it starts with partial oxidation of the benzene ring to form other organic products as intermediates, unlike the slow mineralisation process as the final step, which involves the breaking of the benzene ring to liberate carbon dioxide (CO_2).[45,200,201] An increase in the photocatalytic activities, of the bi-cocatalysts-decorated TiO_2 samples compared to FeOx-decorated TiO_2, is likely due to some synergistic effect from the cocatalyst alloys, which favours efficient separation of photo-generated electrons and holes during photocatalytic degradation of 2,4,6-TCP.
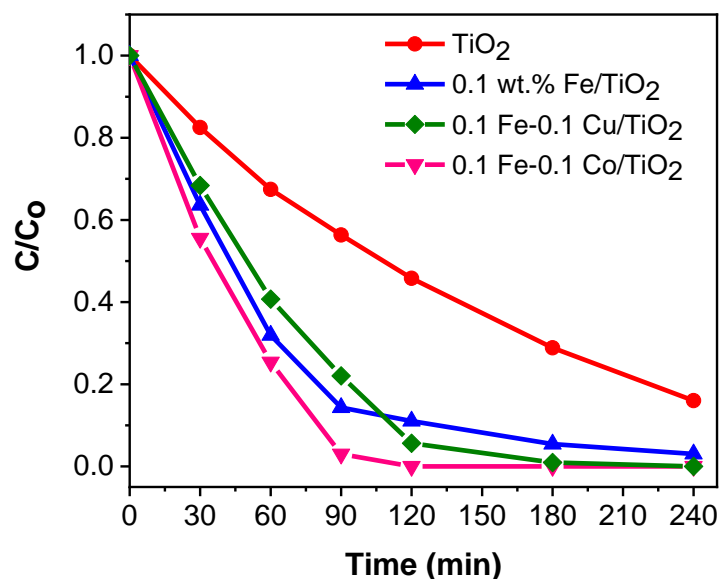
Figure 5-15 Conversion profiles of 2,4,6-TCP using TiO_2, $FeOx/TiO_2$, $FeOx$-$CuOx/TiO_2$ and $FeOx$-$CoOx/TiO_2$ samples monitored by HPLC.

Conditions: 2,4,6-TCP (50 mg/L, 200 mL, pH_{nat} = 6, catalyst concentration = 0.5 g/L, λ > 320 nm).

Fe(III) oxide species (mainly FeOOH as characterised in the previous chapter) have been reported to favour the improved generation of hydroxyl radicals as a hole acceptor in the literature.[155,202,203] It has been reported that Cu(II) oxide species facilitate the transfer of photo-generated electrons on surface of TiO_2 by enhancing oxygen reduction to generate superoxide radicals.[188,191] CoOx has been reported to be a very good oxidation cocatalyst in photo-oxidation of organic compounds[204,205] and oxygen evolution in photocatalytic water splitting by improving the lifetime of photo-generated holes.[206–208]

Surface decoration of TiO_2 with FeOx-CuOx or FeOx-CoOx alloys in photocatalytic water treatment is scarcely reported in the literature. A bi-cocatalyst alloy involving CuO and CoO (1 wt.% Cu and 1 wt.% Co) has been reported to improve the hydrogen evolution rate of SnO_2@TiO_2 in photocatalytic water splitting under UV light irradiation.[209] Also, CuO exhibited higher activity than CoO regarding single cocatalyst-decorated samples. The enhancement in H_2 evolution rate by CuO-CoO/SnO_2@TiO_2 was attributed to the synergistic improvement in the transfer of photo-generated electrons by CuO for reduction reaction and holes by CoO for oxidation reaction on the catalyst's surface.[209] In another study involving single cocatalysts comparison, CuOx was reported to display higher activity compared to FeOx for the photocatalytic degradation of 4-chlorophenol (4-CP) in aqueous solution with TiO_2 under UV light irradiation.[188]

The FeOx cocatalyst facilitates hole transfer for the generation of hydroxyl radicals as reported in previous chapter. The detailed functions of CuOx and CoOx has to be investigated by ESR technique, using the spin trap agent, DMPO and studies on the effect of additives (electron, hole and hydroxyl radical scavengers) on 2,4,6-TCP mineralisation efficiency. However, these characterisations could not be carried out due to the unavailability of equipment, caused by the covid-19 pandemic over the past twelve (12) months.

The experimental error bar plot of the optimised FeOx-CoOx/TiO_2 is shown in **Fig. 5-16** after carrying out the 2,4,6-TCP mineralisation experiment in

triplicates. The result signifies that the experiment is repeatable to a large extent.
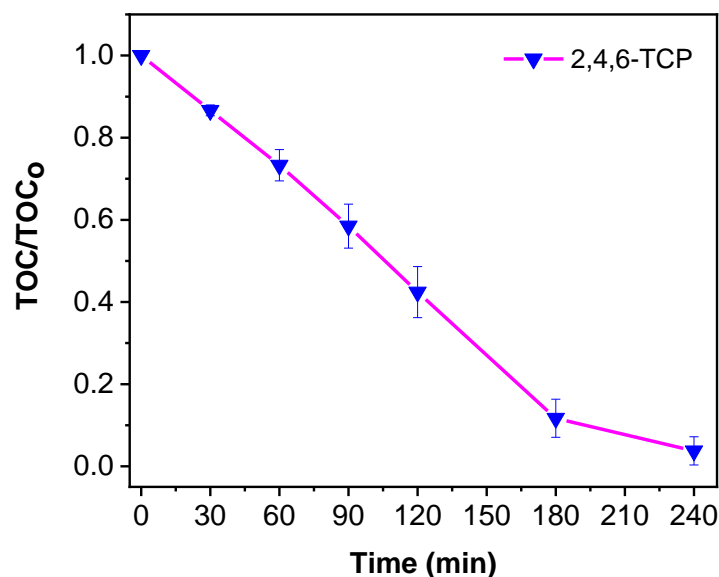
Figure 5-16 TOC measurement with experimental error bar on FeOx-CoOx/TiO$_2$ for 2,4,6-TCP mineralisation after conducting triple experiments.

The photocatalytic activity of the optimised sample (FeOx-CoOx/TiO$_2$) was further evaluated under different light wavelengths and results are displayed in **Fig. 5-17**. Virtually 0% TOC removal was observed after 3 h of light irradiation with a 395 nm cut-off filter. The outcome was not surprising, since surface impregnation of TiO$_2$ with cocatalysts did not reduce the band gap energy of the PC50 TiO$_2$ (ca. 3.2 eV), which corresponds to light wavelength of around 390 nm. This further implies that the pristine and modified TiO$_2$ samples cannot absorb light of wavelength above 390 nm, which results into negligible 2,4,6-TCP degradation activity. However, with

light irradiation of wavelength (λ > 260 nm), there is a remarkable enhancement in the 2,4,6-TCP mineralisation rate in the first 2 h, compared to that of light irradiation of wavelength (λ > 320 nm). This is due to the availability of stronger UV light (UV-B) irradiation and contributions from 2,4,6-TCP photodegradation, since 2,4,6-TCP absorbs UV light below 320 nm. Around 62% TOC removal was achieved with λ > 320 nm, while about 93% TOC removal was achieved with λ > 260 nm in 2 h.
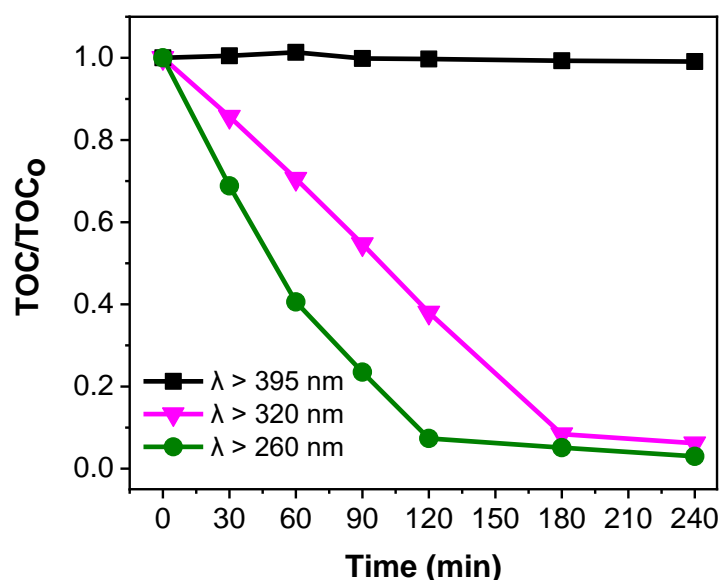
Figure 5-17 Mineralisation profiles of 2,4,6-TCP using FeOx-CoOx/TiO$_2$ sample under different light wavelength (λ) ranges.

Conditions: 2,4,6-TCP (50 mg/L, 200 mL, pH$_{nat}$ = 6, catalyst concentration = 0.5 g/L).

Further studies on photocatalytic mineralisation ability of the optimised FeOx-CoOx/TiO$_2$ sample was evaluated with a widely used herbicide, 2,4-

dichlorophenoxyacetic acid (2,4-D) and results are displayed in **Fig. 5-18**.
0% TOC removal was observed after 3 h of light irradiation in the absence
of a photocatalyst. Nearly 60%, 95% and 100% TOC removal are achieved
with the unmodified TiO_2, $FeOx/TiO_2$ and $FeOx-CoOx/TiO_2$ samples in 3 h,
respectively. 2,4-D removal by the optimised $FeOx-CoOx/TiO_2$ was also
analysed with HPLC and results are shown in **Fig. 5-19**. The 2,4-D
degradation rates well agree with the corresponding mineralisation rates in
the first 60 minutes. The photocatalytic 2,4-D degradation efficiencies in 60
minutes follow the order: TiO_2 (85%) < $FeOx/TiO_2$ (91%) < $FeOx-CoOx/TiO_2$
(95%). Beyond 60 minutes, the three samples recorded approximately
similar photocatalytic activity for 2,4-D degradation. This is likely due to the
presence of very low concentration of 2,4-D in solution and on surface of the
photocatalyst. Also, the 2,4-D degradation process is very fast over FeOx
and FeOx-CoOx-decorated TiO_2 samples compared to the slow
mineralisation process, since partial oxidation precedes the cleavage of the
aromatic benzene ring to liberate carbon dioxide (CO_2).[45,200,201] The FeOx-
$CoOx/TiO_2$ sample also shows the highest 2,4-D mineralisation efficiency
but similar 2,4-D degradation performance compared to $FeOx/TiO_2$ and
TiO_2. The experimental error bar plot of the optimised $FeOx-CoOx/TiO_2$ is
also shown in **Fig. 5-20** after carrying out the 2,4-D mineralisation
experiment in triplicates. The result shows that the experiment is highly
reproducible.
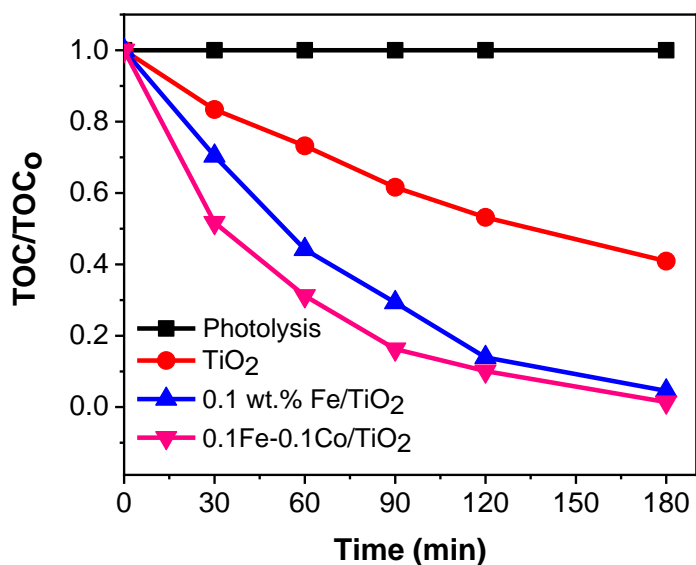
Figure 5-18 Mineralisation profiles of 2,4-D using PC50 TiO_2, $FeOx/TiO_2$ and $FeOx-CoOx/TiO_2$ samples.
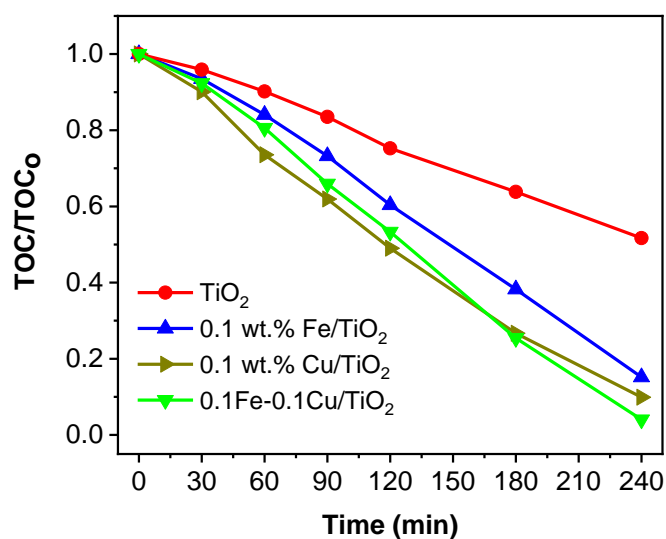
Conditions: 2,4-D (25 mg/L, 200 mL, pH_{nat} = 4, catalyst concentration = 0.5 g/L, λ > 320 nm).
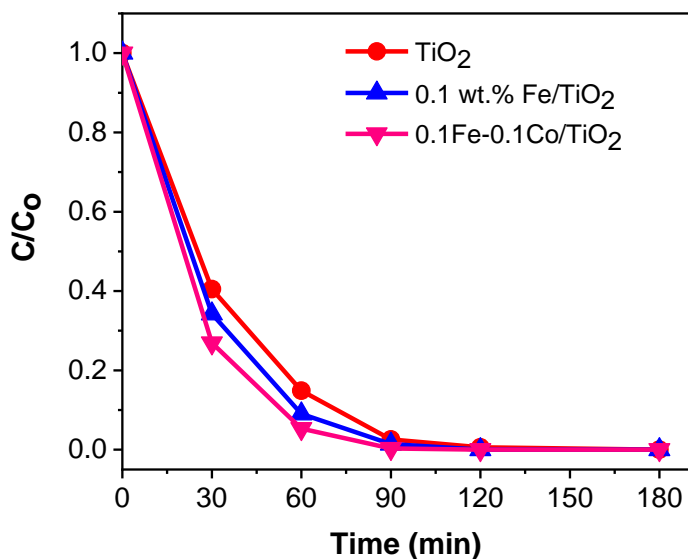
Figure 5-19 Conversion profiles of 2,4-D using PC50 TiO_2, $FeOx/TiO_2$ and $FeOx-CoOx/TiO_2$ samples monitored by HPLC.

Conditions: 2,4-D (25 mg/L, 200 mL, pH_{nat} = 4, catalyst concentration = 0.5 g/L, λ > 320 nm).
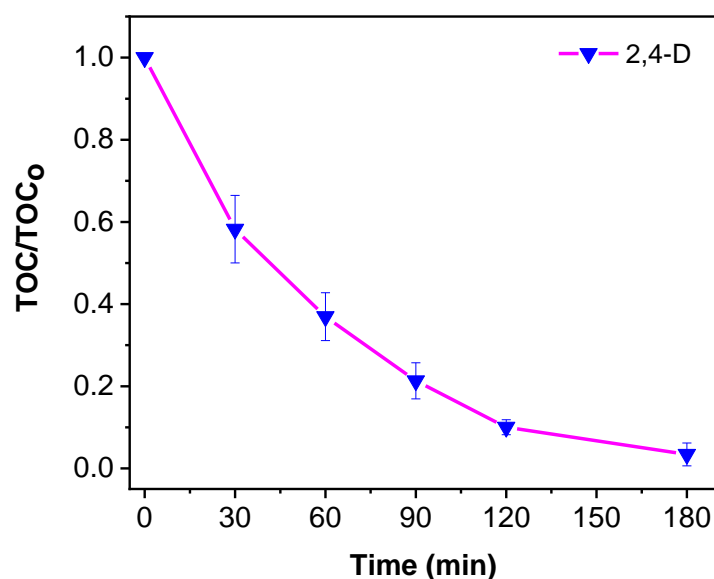
Figure 5-20 TOC measurement with error bar on FeOx-CoOx/TiO$_2$ for 2,4-D mineralisation after conducting triple experiments.

In order to investigate how the chlorine substituents and other functional groups on the aromatic benzene ring influence photocatalytic degradation activity, two chlorophenols (2,4-DCP and 2,4,6-TCP) and two chlorinated herbicides (2,4-D and 2,4,5-T) were evaluated using the optimised photocatalyst composite. It was reported that the number and positions of the chlorine substituents play vital roles in predicting the level of toxicity and degradation rate of each members of the chlorinated phenols group.[13,99,210–212] Based on the results in **Fig. 5-21**, the two chlorophenols are more difficult to mineralise compared to their phenoxyacetic acid counterparts. This could be due to the difference in the oxygen functional groups (hydroxyl and acetic acid) on the aromatic ring for both classes of

chlorinated herbicides, and likely the acetic acid group can be readily degraded. It is widely reported that 2,4,6-TCP degrades faster than 2,4-DCP during photocatalytic water treatment.[99,211,212] However, there is no clear relationship between the degradation rate of chlorophenols and number of chlorine substituents on the aromatic ring but the position of Cl atoms was reported to highly determine the order of initial degradation rates.[213,214]. In the first 90 min, 2,4-DCP is the most difficult to mineralise, while 2,4-D and 2,4,5-T (with similar trend) are the easiest to mineralise. The temporal UV-vis absorption spectra of the four herbicides at 90 minutes of photocatalytic degradation are shown in **Figs. 5-22 a-d.** The results corroborate the earlier observation with TOC removal rates as 2,4-DCP remains the most difficult to degrade, while 2,4-D and 2,4,5-T are easiest to degrade.
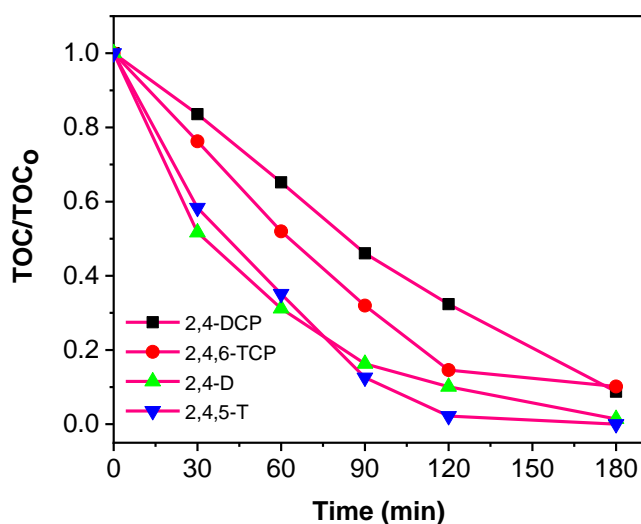
Figure 5-21 Mineralisation profiles of selected herbicides using FeOx-CoOx/TiO$_2$ sample under similar operating conditions.

Conditions: Herbicides (25 mg/L, 200 mL, pH$_{nat}$ = 4, catalyst concentration = 0.5 g/L, λ > 320 nm).
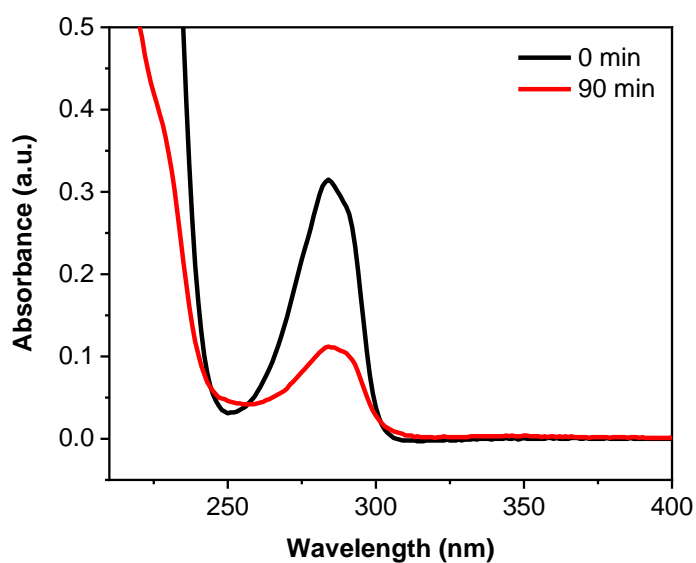
Figure 5-22a Temporal UV-vis absorption spectra of 2,4-dichlorophenol (2,4-DCP) at 90 minutes of photocatalytic degradation.
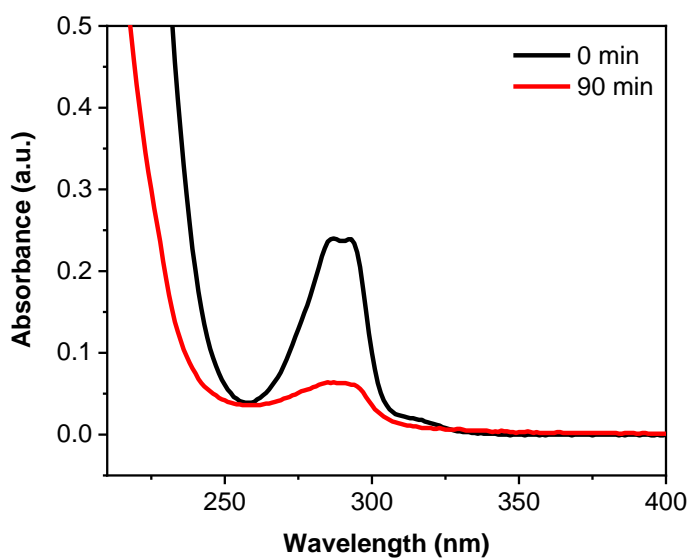
Figure 5-22b Temporal UV-vis absorption spectra of 2,4,6-trichlorophenol (2,4,6-TCP) at 90 minutes of photocatalytic degradation.
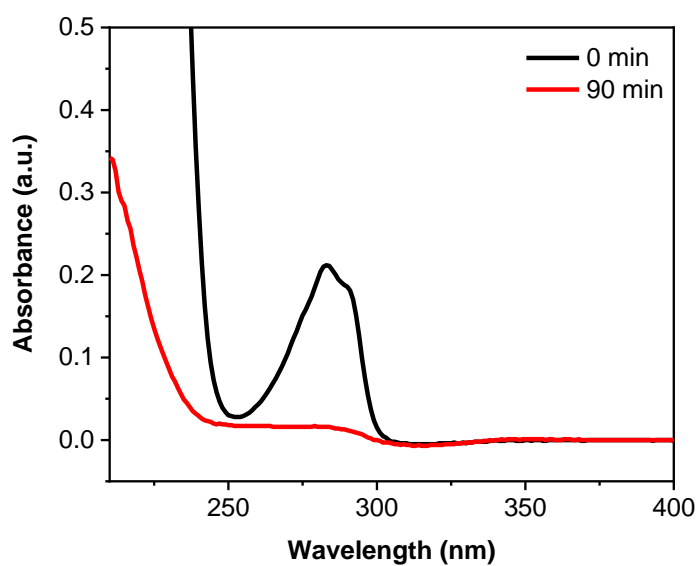
Figure 5-22c Temporal UV-vis absorption spectra of 2,4-dichlorophenoxyacetic acid (2,4-D) at 90 minutes of photocatalytic degradation.
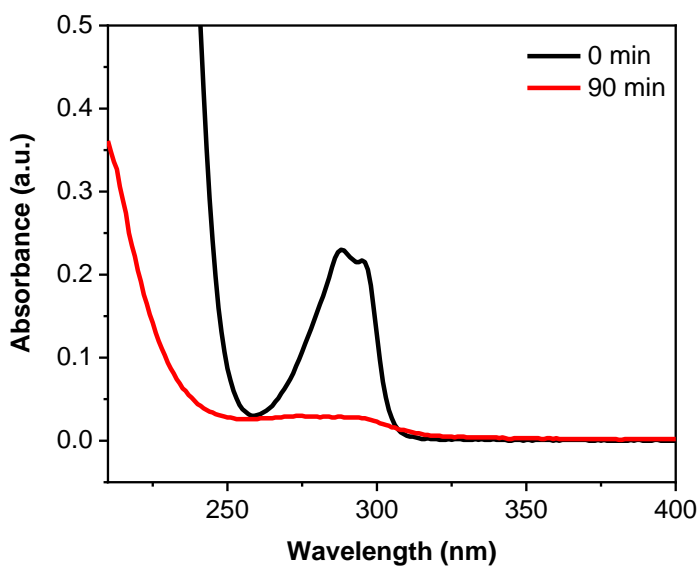
Figure 5-22d Temporal UV-vis absorption spectra of 2,4,5-trichlorophenoxyacetic acid (2,4,5-T) at 90 minutes of photocatalytic degradation.

5.3.3 Catalyst recycling and reactive oxygen species tests

The stability of the best FeOx-CoOx/TiO$_2$ composite photocatalyst was evaluated for 2,4,6-TCP mineralisation under full arc light irradiation ($\lambda >$ 260 nm) as shown in **Fig. 5-23**. It can be seen that the photocatalytic activity of composite did not decrease conspicuously after four successive cycles (2 hours) of 2,4,6-TCP mineralisation test, indicating that the composite is fairly stable. However, XPS analysis of the FeOx-CoOx/TiO$_2$ sample, after catalyst recycling test, shows only the presence of FeOx as seen in the Fe 2p XPS spectra (**Fig. 5-24**), while CoOx is not clearly detected as shown in the Co 2p XPS spectra (**Fig. 5-25**). This could be due to leaching of CoOx cocatalyst from surface of TiO$_2$ during photocatalytic mineralisation of 2,4,6-TCP, or catalyst fouling as a result of organic residues from degradation intermediates. The fair stability of FeOx-CoOx/TiO$_2$ after four successive activity cycles suggests that a small amount of CoOx is required in the FeOx-CoOx/TiO$_2$ composite to improve its performance.
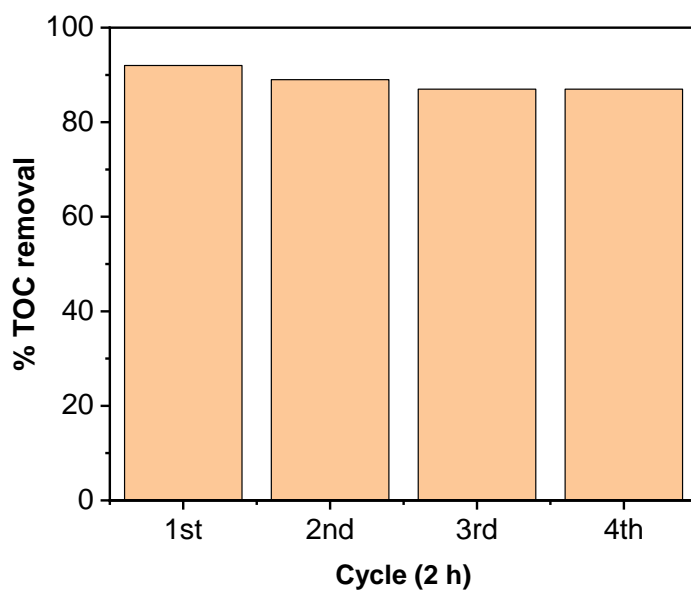
Figure 5-23 Recycling performance of FeOx-CoOx/TiO$_2$ for 2,4,6-TCP mineralisation.

Conditions: 2,4,6-TCP (50 mg/L, 200 mL, pH$_{nat}$ = 6, catalyst concentration = 2.5 g/L, λ > 260 nm).
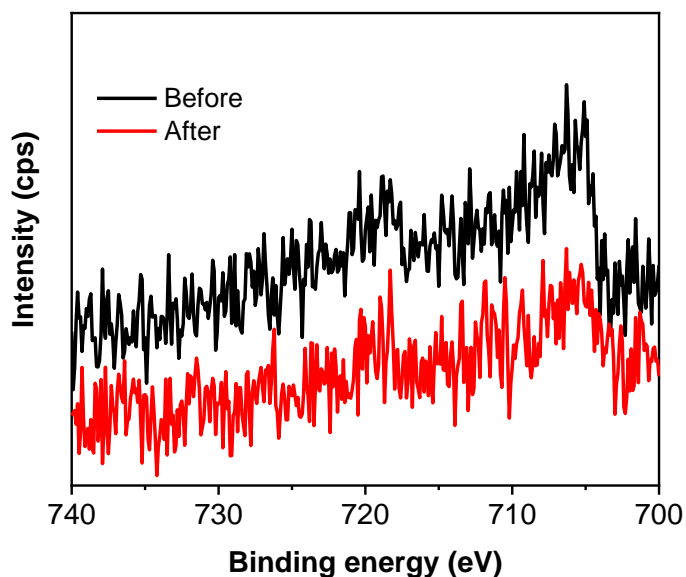
Figure 5-24 Fe 2p XPS spectra of FeOx-CoOx/TiO$_2$ sample before and after four successive cycles of catalyst recycling.
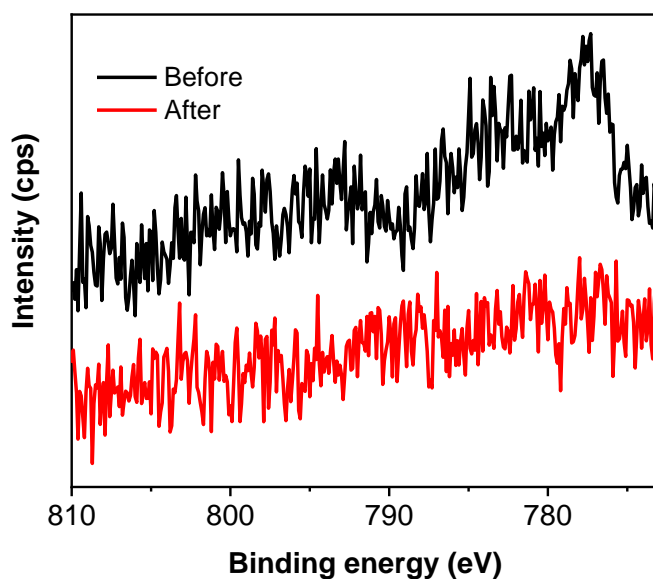
Figure 5-25 Co 2p XPS spectra of FeOx-CoOx/TiO$_2$ sample before and after four successive cycles of catalyst recycling.

Hydroxyl radicals ($^\bullet$OH) are considered the major active species during photocatalytic degradation of organic water pollutants, while the short lifetime (~ 10^{-9} s) and high reactivity of the hydroxyl radicals hinder its direct detection [96,158]. Fluorescence spectroscopy was used to investigate the presence of $^\bullet$OH with coumarin (COU) as a probe molecule (poor fluorescent dye). The COU can react with $^\bullet$OH to give a highly fluorescent 7-hydroxycoumarin (7-HC).[158] A very low concentration (10^{-3} – 10^{-4} M) of the probe molecule is often used during spectrofluorometric analysis to limit contributions from the valence band holes of TiO$_2$ during illumination with UV light.[159] Lower concentrations of the probe molecule usually favours hydroxylation reaction with $^\bullet$OH. [159,215] **Fig. 5-26** shows the fluorescence spectra of COU solutions (0.001 M) containing 0.6 mg/mL of PC50 TiO$_2$,

FeOx/TiO$_2$, FeOx-CuOx/TiO$_2$ and FeOx-CoOx/TiO$_2$ under 5 min irradiation from a multi-channel 300 W UV LED (365 nm). No signal was observed without a photocatalyst. The fluorescent intensities at around 455 nm follow the order: PC50 TiO$_2$ < FeOx-CuOx/TiO$_2$ < FeOx/TiO$_2$ < FeOx-CoOx/TiO$_2$. The highest fluorescence intensity obtained from FeOx-CoOx/ TiO$_2$ implies a high concentration of 7-HC, as a result of high generation rate of $^\bullet$OH radical, which is very beneficial for the degradation of these herbicides. This indicates that FeOx-CoOx/TiO$_2$ facilitates charge separation via hole transfer from TiO$_2$ as highlighted in the proposed semiconductor charge separation mechanism (**Fig. 5-27**). When the FeOx-CoOx/TiO$_2$ photocatalyst is exposed to ultraviolet light, photo-generated electrons are excited from the valence band (VB) to the conduction band (CB) of TiO$_2$. The VB holes are transferred to the surface FeOx/CoOx sites and subsequently react with hydroxyl ions (OH$^-$) in water to produce OH radicals, which oxidises 2,4,6-TCP and other herbicides to intermediate products before their mineralisation. At the same time, photoelectrons are consumed by oxygen to produce superoxide radicals that react with the intermediates to form the final CO$_2$ and water.
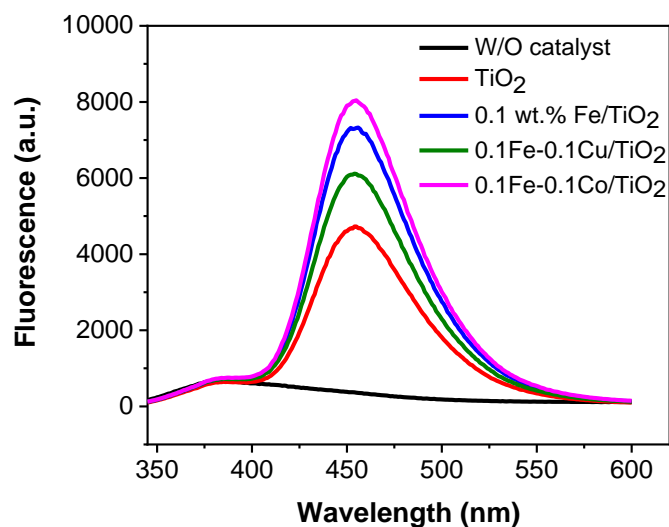
Figure 5-26 Fluorescence spectral changes observed during illumination of prepared TiO_2 samples in 0.001 M aqueous solution of coumarin (excitation at 332 nm).

Each fluorescence spectrum was recorded after 5 minutes of light illumination with 300 W UV 365 nm LED.
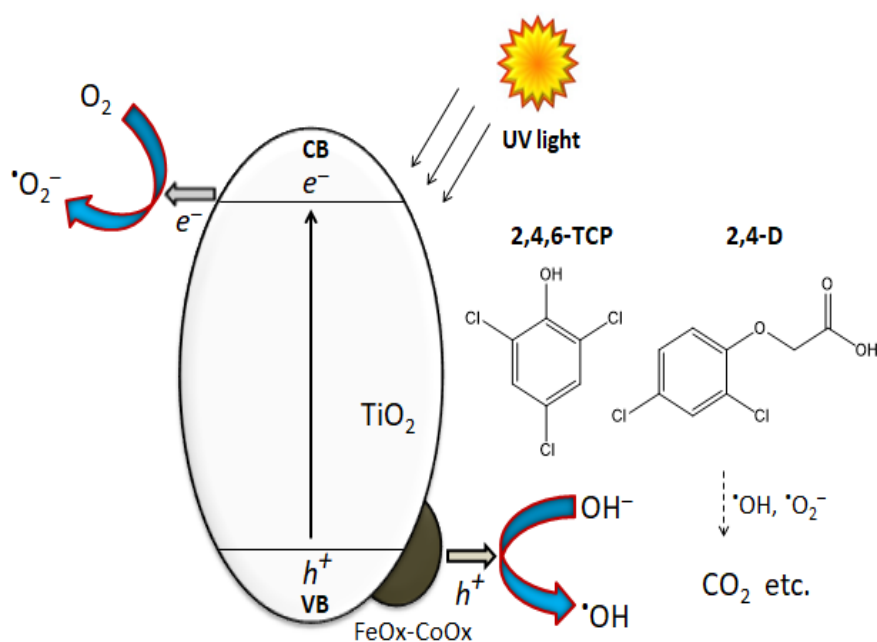
Figure 5-27 Proposed mechanism for major charge transfer pathways on $FeOx\text{-}CoOx/TiO_2$ for mineralisation of 2,4,6-TCP and 2,4-D.

5.3.4 Future work

A few more experiments would be carried out in this chapter in order to fully understand the active species of these cocatalysts, reaction pathway and disappearance of Co species after reactions, which cannot be carried out due to unavailability of equipment as a result of covid-19 pandemic over the past twelve (12) months.

1. Effect of scavengers e.g. EDTA (for h+), isopropanol (for $^\bullet OH$) and 1,4-benzoquinone (for $^\bullet O_2^-$) on the photocatalytic activity of the prepared catalysts for 2,4,6-TCP and 2,4-DCP degradation monitored by using HPLC. This study will provide a fundamental understanding on the underlying photocatalytic reaction mechanism of $FeOx$-$CuOx/TiO_2$ and $FeOx$-$CoOx/TiO_2$ during photoactivity tests.

2. Further material characterisation to complement previous XPS results in the detailed identification of the cocatalyst species on TiO_2. XPS analysis will be carried out on the single cocatalyst-modified TiO_2 samples to see if there is any similarity or difference with the cocatalyst species in $FeOx$-$CuOx/TiO_2$ and $FeOx$-$CoOx/TiO_2$. HRTEM-EDS analysis will be carried out to image the cocatalyst species on TiO_2, their dispersity and also observe if there is any form of interaction between the cocatalysts (Fe-Cu and Fe-Co) to give an alloy.

3. Further studies on the degradation of the four investigated herbicides using optimised $FeOx$-$CoOx/TiO_2$ and monitored by HPLC. This study will help to complement previous TOC removal results and

compare the order of degradation rates for the four selected herbicides.

4. Other studies, e.g. ICP-MS analysis to investigate the stability of FeOx and CoOx nanoparticles on TiO_2 during photocatalytic water treatment and characterisation of sample before and after recycling.

5.4   Conclusion

In summary, facile and robust synthesis procedure was successfully used in decorating PC50 TiO_2 nanoparticles with highly dispersed mono and dual cocatalysts (FeOx, CuOx, CoOx, FeOx-CuOx and FeOx-CoOx). The binary cocatalyst comprising FeOx-CoOx plays a key role for efficient decomposition of widely used four chlorinated herbicides. FeOOH (denoted as FeOx in this chapter), CuO and CoO nanoparticles were determined to be the only decorating species. The highest photocatalytic 2,4,6-TCP mineralisation efficiency was achieved by the FeOx-CoOx/TiO_2. About 92% 2,4,6-TCP mineralisation and 100% 2,4,6-TCP degradation efficiencies in 3 h, were achieved over the optimised FeOx-CoOx/TiO_2 sample, which is about three times higher than the benchmark reference PC50 TiO_2 and about two times higher than optimised FeOOH/TiO_2 (0.14 wt.% Fe) composite previously reported in Chapter 4. The photocatalytic 2,4,6-TCP mineralisation efficiencies in 3 h followed the order: TiO_2 (36%) < FeOx/TiO_2 (62%) < CoOx/TiO_2 (64%) < CuOx/TiO_2 (73%) < FeOx-CuOx/TiO_2 (75%) <

FeOx-CoOx/TiO$_2$ (92%). The results showed that a synergistic improvement in photocatalytic activity was achieved with the novel bimetallic FeOx-CoOx/TiO$_2$ when compared with the monometallic samples (FeOx/TiO$_2$ and CoOx/TiO$_2$). The optimised FeOx-CoOx/TiO$_2$ sample also exhibited 150% activity enhancement for another herbicide (2,4-D) degradation compared to unmodified TiO$_2$. However, the FeOx-CoOx/TiO$_2$ sample showed negligible activity for 2,4,6-TCP degradation under visible light ($\lambda > 395$ nm) irradiation. This is primarily due to the UV absorption bandgap energy of PC50 TiO$_2$ (3.2 eV or 390 nm), since the low concentration surface cocatalysts did not alter its bandgap based on the UV absorption spectra of the prepared photocatalysts. Under similar operating conditions, the mineralisation rates with 2,4-D and 2,4,5-T were higher compared to 2,4-DCP and 2,4,6-TCP. 2,4-DCP was the most difficult to mineralise. The observation is likely due to the nature of oxygen functional groups and the relative position of Cl substituents on the aromatic ring. The enhancement in photocatalytic degradation of 2,4,6-TCP and 2,4-D over the optimised FeOx-CoOx/TiO$_2$ sample, is likely due to the improved charge separation, hole accumulation on FeOx-CoOx and the enhanced hydroxyl radicals generation as FeOx-CoOx clusters are an excellent hole acceptor.The optimised photocatalyst was proved to be stable for these herbicides' mineralisation. A few more important studies were also proposed to fully understand the active species of these cocatalysts, reaction mechanism and disappearance of Co species after reactions.

The next chapter will focus on the immobilisation of optimised TiO_2 samples on polymer substrate and application in photocatalytic oxidation of MB dye and reduction of Cr (VI) ions in aqueous solution. The TiO_2/polymer composites could not be tested for the herbicides due to non-availability of HPLC as a result of covid-19 pandemic.

6 Fabrication of FeO$_x$-CoO$_x$/TiO$_2$/polymer composite for the photocatalytic oxidation of MB and reduction of Cr (VI) in aqueous solution

6.1 Introduction

One of the major challenges of TiO$_2$ application in photocatalytic water treatment technology is the recovery of TiO$_2$ nanoparticles from solution in slurry/suspension systems. Most of the reports in literatures used the conventional slurry/suspension method, which involves the dispersion of TiO$_2$ powder in contaminated water.[216–220] Although, the suspension/slurry method maximises UV light absorption and mass transfer of pollutants, and nanoparticles of TiO$_2$ can also maximise the reaction surface area, major challenges confronting the suspension system include, high turbidity, which may enhance light scattering, and limited prospect of catalyst reuse due to difficulty of the separation of nanoparticle catalyst from the solution and high filtration cost at industrial scale. [221,222]

In order to avoid the drawbacks of slurry-suspension method, there is a trend to immobilise TiO$_2$ nanoparticles on both organic and inorganic substrates. For example, TiO$_2$ has been reported to be immobilised in different types of polymer [223–228], paints [222,229–231], cement [232–237], glass [238,239], cellulose [240–244], ceramics [245–248], silica beads [249,250], clay [251–255], carbon fiber [256–258] and metallic materials.[259–261] Though the photocatalyst support may be selected from a wide range of materials, the following are

very essential.[262–265] (a) the immobilising agent should strongly bind the TiO$_2$ nanoparticles, (b) the photocatalyst activity should not drastically reduce upon immobilisation, (c) the immobilising agent should be highly stable against TiO$_2$ photocatalytic degradation and (d) the immobilising agent should possess high surface area and enhance adsorption of pollutants.

Most of the photocatalyst immobilisation techniques are limited to a particular type of substrate/matrix, requiring sophisticated procedure, instrumentations, hazardous chemicals, thus may suffer from scalability and industrial adaptability.[222] The development of a photocatalytic TiO$_2$ paint using a commercial UV polymer was recently reported for the degradation of MB, methyl orange and indole under both UV and sunlight irradiation.[222] The paint was applied and polymerised/solidified on plastic petri dishes by ultraviolet light irradiation. Under UV-B light irradiation, about 80 and 40% MB got degraded after 120 min by 10 wt.% TiO$_2$/polymer and 0 wt.% TiO$_2$/polymer composites, respectively. From hydroxyl radical generation measurement using sodium terephthalate solution and spectrofluorometer, It was reported that bare polymer generated some amount of •OH under light irradiation. This was believed to be due to the presence of some fluorescent compounds (photo initiator) in the polymer resin.

Following the success of the best modified TiO$_2$ photocatalyst nanoparticles earlier reported in the previous chapters, TiO$_2$/polymer composites were further developed and tested for the real application in this chapter.

Compared with the conventional method which mainly involves the initial mixing of both TiO_2 nanoparticles and the acrylate-based polymer resin before UV light irradiation,[222] the modified recipe includes that TiO_2 nanoparticles are firstly carefully dispersed on surface of polymer resin in a plastic petri dish before UV light irradiation. The modified method not only improves the interaction between TiO_2 nanoparticles and the adsorbed water pollutants but also avoids the embodied TiO_2 in the bulk polymer, so as to provide a higher degree of utilisation of TiO_2 photocatalysis and better photocatalytic performance. The prepared TiO_2/polymer composites were evaluated for the photocatalytic oxidation of MB dye and reduction of Cr (VI) ions to less toxic Cr (III) in an aqueous solution. MB and Cr (VI) ions are widely used as the model water pollutants because they are known to be toxic and carcinogenic to both aquatic and human life.[266,267]

6.2   Experimental section

6.2.1 Chemicals

PC50 TiO_2 (purely anatase) was purchased from Millennium chemicals. Degussa P25 TiO_2 (80% Anatase : 20% Rutile) was purchased from Evonik. MB trihydrate was purchased from Alfa Aesar. UV curable polymer resin (polymer precursor), $Fe(NO_3)_3.9H_2O$, $Co(NO_3)_2.6H_2O$, 1,5-Diphenylcarbazide and $K_2Cr_2O_7$ were purchased from Sigma-Aldrich. All reagents were used as received without further purification.

6.2.2 Fabrication of photocatalysts

The conventional photocatalytic paints (consisting of a mixture of TiO_2 nanoparticles and polymer resin/precursor) were prepared separately using 5, 10 and 20 wt.% commercial PC50 TiO_2 in clean plastic petri dishes as the reference.[222] The weighed amounts of both materials (polymer precursor and catalyst) were thoroughly mixed with a spatula and ultra-sonicated for 10 min to achieve uniform milky suspension. The overall weight of TiO_2 and polymer resin was 1 g in every petri dish. Subsequently, the mixture was photo-polymerised in a UV-B photo-reactor for 3 h to obtain a rigid nanocomposite. In the modified two-step method, The bottom of the plastic petri dish was firstly painted using 0.5 g of the polymer resin/precursor and a spatula to generate about 1 mm thickness. Subsequently, 1 g of newly prepared photocatalyst powder (TiO_2, $FeOx/TiO_2$ and $FeOx$-$CoOx/TiO_2$) based on synthesis procedure reported in Chapter 5 (representing ~ 67 wt.% of the composite) was carefully distributed on the polymer resin, leaving room for photo-polymerisation to still occur under UV light irradiation for 4 h. Then it was scrubbed to remove free catalyst particles and thoroughly washed with distilled water. The percentage weights of pristine TiO_2 and modified TiO_2 in the modified two-step method are over 60 wt.% after surface cleaning and air-drying of the prepared TiO_2/polymer composites.

A schematic diagram, representing the procedure for the preparation of TiO_2/polymer composites via the conventional (one-step) and modified (two-step) methods is shown in **Fig. 6-1**.

177
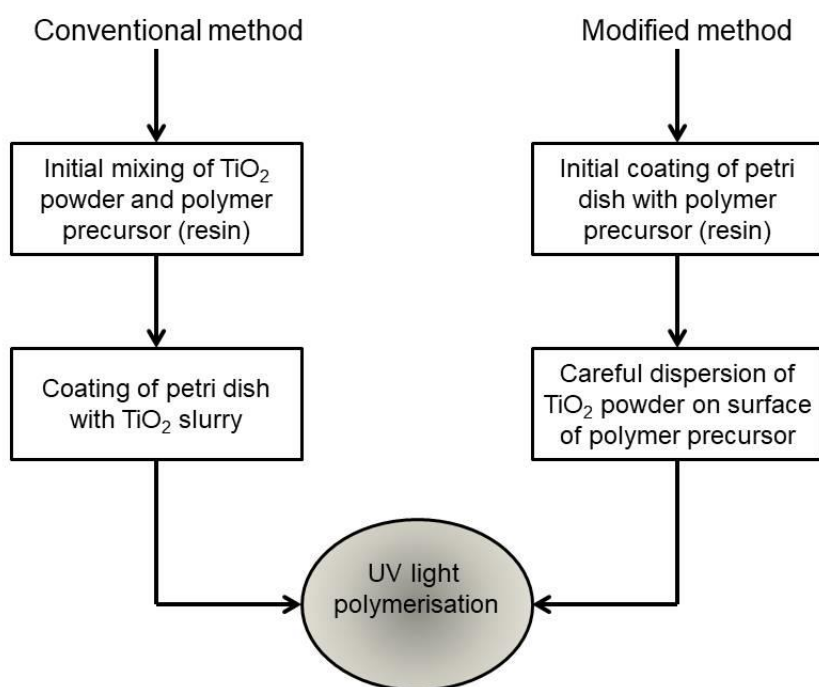
Figure 6-1 Schematic diagram of the synthesis procedure for TiO_2/polymer composites.

6.2.3 Characterisation

Attenuated total reflection Fourier-transform infrared spectroscopy (ATR-FTIR) data of the photopolymer was collected using Shimadzu IRAffinity-1s spectrometer with a Specac Quest (Germanium) ATR accessory at a range of 700-2600 cm^{-1}.

6.2.4 Photocatalytic activity test

UVP Ultraviolet Crosslinker (Analytik Jena, CL-3000M, USA) having UV-B fluorescent tube lamps (6 x 8 W), was used as the source of UV light of about 302 nm wavelength, as per the specification of the vendor. In a typical measurement, TiO_2/polymer petri dishes containing 10 mL of either 10 mg/L

MB or 25 mg/L Cr (VI) solution at natural solution pH of 6 and 5.5, respectively were used during the photocatalytic experiments and without stirring as shown in **Fig. 6-2**.[222] The dimension of the inner chamber is 35 cm x 27 cm x 16 cm for length, width and height, respectively. The temperature in the sample chamber did not rise above 30 ^{o}C during light irradiation and is in agreement with the vendor's specification. The light intensity of the UV lamp is 2.704 mW/cm^2 as measured by a Newport power meter (1908-R) after calibration to 302 nm.

The samples were left in the dark for 30 min to achieve adsorption/desorption equilibrium of tested water pollutants on the TiO$_2$/polymer composite. Subsequently, the solutions were illuminated in the UV photo-reactor and about 2 mL sample was withdrawn for UV–visible spectroscopic analysis at a regular interval of 30 min and immediately restored during the 2 h test for MB degradation. The MB dye solution was put back into the petri dish after the UV–vis spectrophotometric studies followed by further light irradiation. The Cr (VI) samples were only analysed after 1 h of UV light irradiation using 1,5-diphenylcarbazide colorimetric method. The influence of FeOx and FeOx-CoOx cocatalysts on TiO$_2$/polymer was also investigated. The TiO$_2$/polymer composites had negligible effect on the overall pH of the solution before photocatalysis

Similar experimental setup was used in the control tests (photolysis and dark adsorption) during MB degradation and Cr (VI) redution. However, photolysis of MB in 2 h and Cr (VI) in 1 h were carried out in clean plastic

petri dishes without polymer or TiO_2/polymer composites. Dark adsorption studies on MB and Cr (VI) in 1 h were carried out without light irradiation.

Stability test was carried out on the best sample under similar operational conditions during photocatalytic MB oxidation and Cr (VI) reduction experiments. The cycle tests were performed at one hour intervals. The surface of the optimised TiO_2/polymer composite was cleaned by rinsing the plastic petri dish after each cycle with D.I. water, and subjecting the plastic petri dish containing D.I. water to light irradiation for over one hour, in order to present a clean catalyst surface for subsequent cycles.

Figure 6-2 UV lamp used for preparation and photocatalytic test of polymer/TiO_2 composites.

6.2.5 Calibration of MB and Cr (VI) standard solutions

The calibration solutions with concentrations between 1 mg/L and 12 mg/L for MB and between 3 mg/L and 35 mg/L for Cr (VI) were prepared by serial dilution of one standard stock solution. The absorption measurements for Cr (VI) were obtained using the standard 1,5-diphenylcarbazide colorimetric method with 540 nm as monitored wavelength for the derived purple complex.[268–270] In a typical measurement, 8 mL 0.2 M H_2SO_4 aqueous solution was added to 1 mL of Cr (VI) sample in a glass test tube, followed by addition of 0.2 mL 0.25% (w/v) 1,5-diphenylcarbazide (1,5-DPC) in acetone as chromogenic agent. The resultant solution was shaken for 10 – 30 secs and left to stand for 10 min before analysis. The MB absorption measurements were monitored at 664 nm.[271,272]

6.3 Results and discussion

6.3.1 Materials characterisations

The image of some TiO_2/polymer composites prepared by one-step conventional mixing of TiO_2 powder and polymer precursor (acrylate-based resin) is shown in **Fig. 6-3a**. The polymer resin alone took about 30 min to completely polymerise/solidify. The complete polymerisation/solidification of the TiO_2/polymer resin varied from 30 min to 4 h during UV light irradiation due to the presence of TiO_2 nanoparticles in the resin.
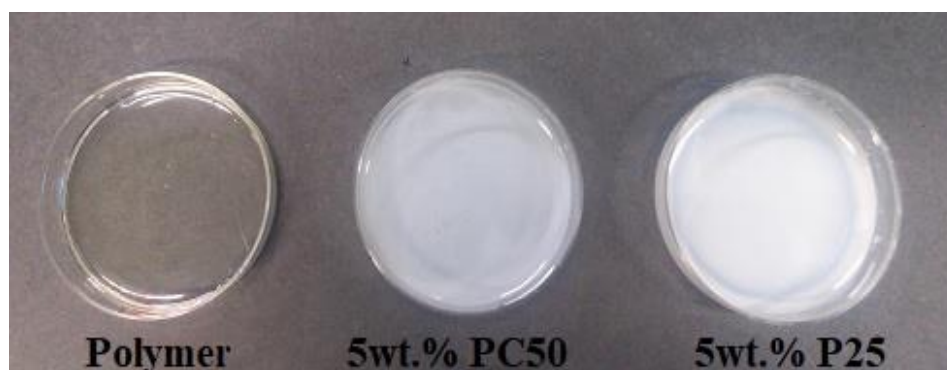
Figure 6-3a Polymer/TiO$_2$ composites prepared by conventional one-step method.

Fig. 6-3b shows the image of some TiO$_2$/polymer composites prepared by a two-step modified method, which involves the initial coating of the plastic petri dish with polymer resin (precursor) before carefully dispersing a weighed amount of TiO$_2$, FeOx/TiO$_2$ and FeOx-CoOx/TiO$_2$ separately on the polymer precursor before light irradiation. The TiO$_2$/polymer composites prepared by two-step method were all irradiated for 4 h to achieve complete polymerisation/solidification. **Fig. 6-4** shows the FT-IR spectra of the polymer resin (without TiO$_2$) before and after polymerisation process. Generally, the intensities of the observed peaks reduced after curing (e.g. at 1700 and 1450 cm^{-1}), while some peaks were absent in the solidified polymer (e.g. between 1100 and 900 cm^{-1}).
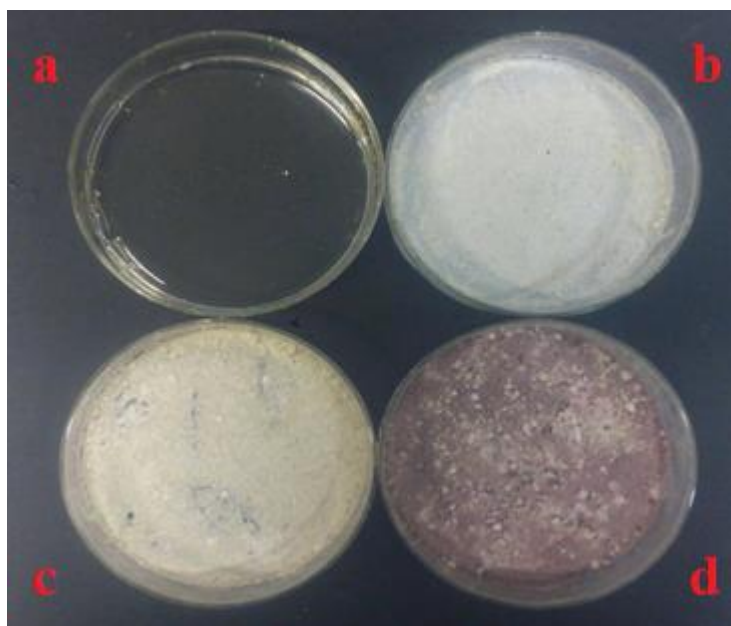
Figure 6-3b Polymer/TiO$_2$ composites prepared by modified two-step method.

Where, **a** represents polymer, **b** is TiO$_2$/polymer, **c** is FeOx/TiO$_2$/polymer and **d** is FeOx-CoOx/TiO$_2$/polymer.
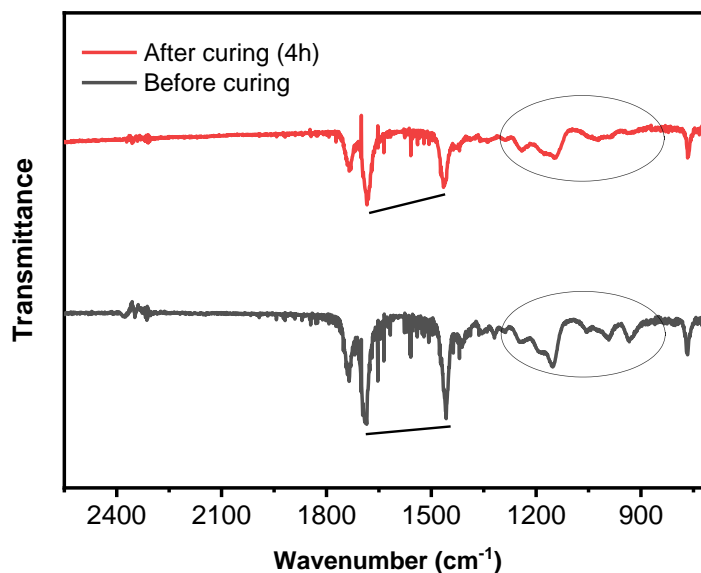
Figure 6-4 FT-IR spectra of polymer before and after curing of polymer precursor.

6.3.2 Photocatalytic activity test

In order to evaluate the photocatalytic degradation rate of MB and conversion rate of Cr (VI), the calibration curves (**Fig. 6-5 and Fig. 6-6**) were first made, respectively with measurements obtained from a UV-vis spectrophotometer. Both measurements show a linear working range and the correlation coefficients of MB and Cr (VI) calibration curves are 0.997 and 0.999, respectively. Photocatalytic efficiency was determined by time-dependent C/C_o, where C is the remaining MB or Cr (VI) concentration and C_o is the initial MB or Cr (VI) concentration.
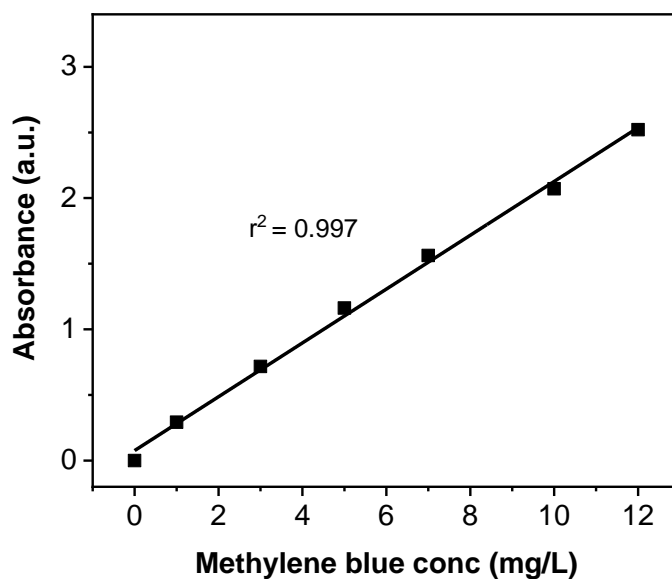
Figure 6-5 Calibration curve for MB standards at 664 nm as λ_{max}.
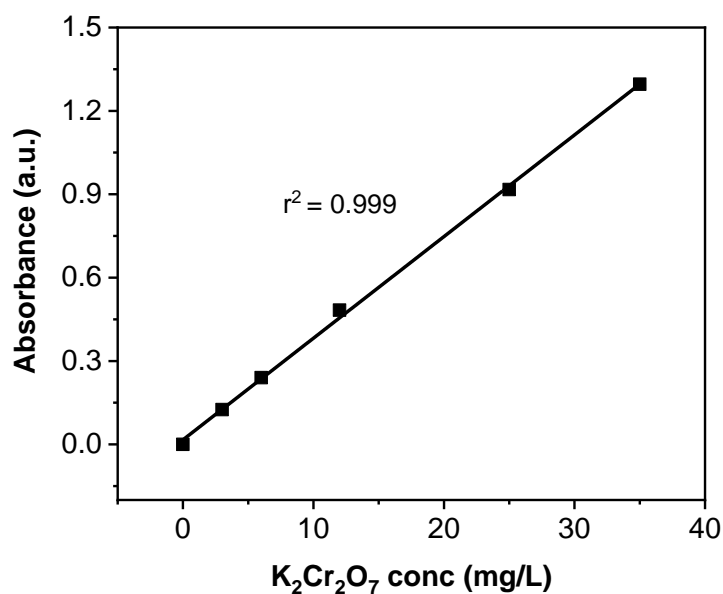
Figure 6-6 Calibration curve for $K_2Cr_2O_7$ standards at 540 nm as λ_{max}.

Photocatalytic activities of the as-prepared TiO_2/polymer composites were first evaluated by the photo-degradation of MB under UV light irradiation (302 nm), as shown in **Fig. 6-7**. There is no MB decomposition in the absence of both photocatalyst and polymer. Virtually 0% MB removal is observed after 2 h of light irradiation. The MB removal results in **Fig. 6-8a**, using TiO_2/polymer composites (5, 10 and 20 wt.% TiO_2) prepared by conventional one-step method, show negligible activities compared to sample containing only polymer (55% MB removal in 2 h). The MB removal in the absence of TiO_2 is likely due to the generation of a small amount of •OH radical by the bare polymer to degrade MB dye.[222]

TiO_2/polymer composites containing above 20 wt.% TiO_2 could not be prepared due to very low viscosity and difficulty in spreading the thick slurry

uniformly inside the petri dishes. The TiO_2/polymer composites prepared by one step conventional method did not show improved photocatalytic activities compared to the polymer sample (**Fig. 6-8a**). The observation could be due to complete trapping of the TiO_2 nanoparticles in the polymer matrix, thus preventing the TiO_2 nanoparticles from participating in photocatalytic MB decomposition.
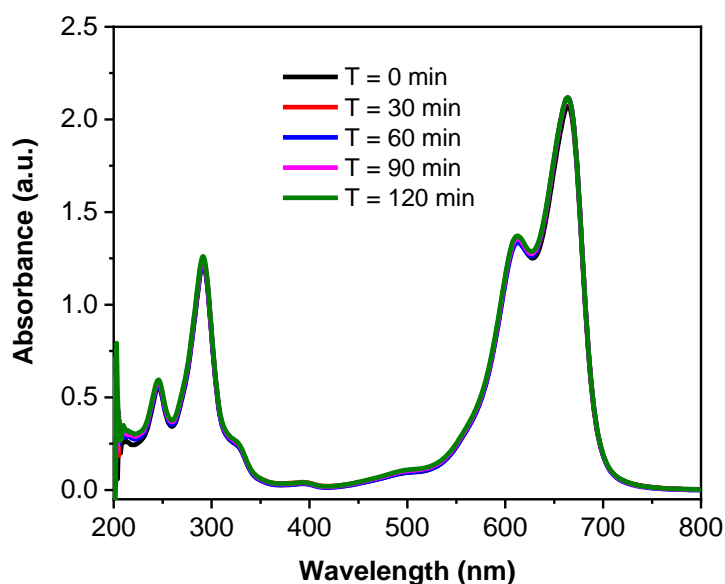
Figure 6-7 Temporal UV-vis absorption spectra of 10 mL, 10 mg/L MB solution in a plastic petri dish during photolysis.

Conditions: MB dye (10 mg/L, 10 mL, pH_{nat} = 6, light λ = 302 nm, temperature ≤ 30 ^{o}C, sample replaced after each analysis).
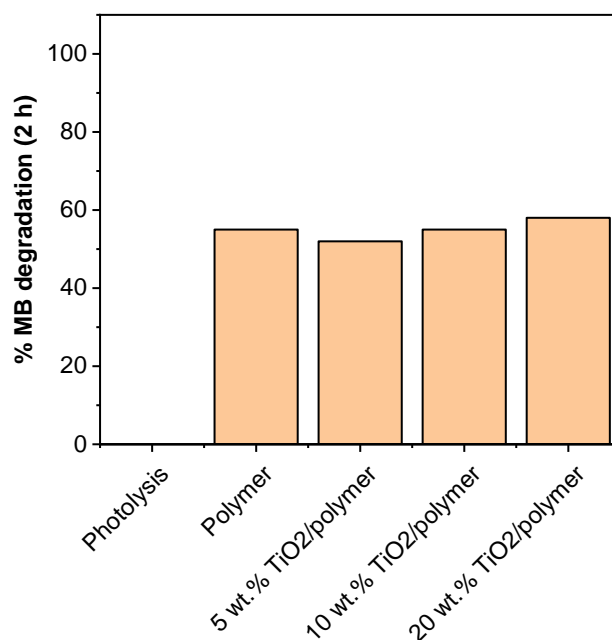
Figure 6-8a MB degradation in 2 h using various TiO_2/polymer composites prepared by conventional (one-step) method.

Conditions: MB dye (10 mg/L, 10 mL, pH_{nat} = 6, light λ = 302 nm, temperature ≤ 30 °C, sample replaced after each analysis).

The MB decomposition results in **Fig. 6-8b**, using TiO_2/polymer composites prepared by modified two-step method, shows that the highest photocatalytic degradation activity is achieved by the FeOx-CoOx/TiO_2/polymer composite, resulting in about 95% MB removal in 1 h. The photocatalytic MB degradation efficiencies in 60 minutes follow the order: polymer (32%) < TiO_2/polymer (44%) < FeOx/TiO_2/polymer (72%) < FeOx-CoOx/TiO_2/polymer (95%).
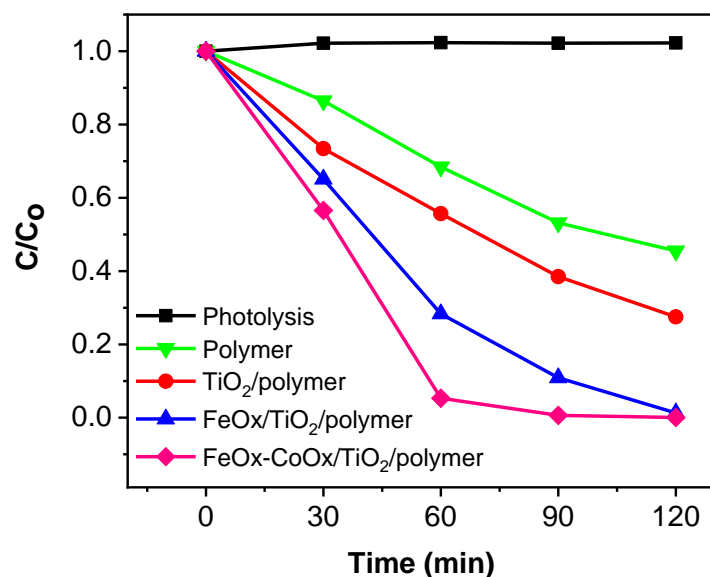
Figure 6-8b Conversion profiles of MB using various TiO_2/polymer composites prepared by modified (two-step) method.

Conditions: MB dye (10 mg/L, 10 mL, pH_{nat} = 6, light λ = 302 nm, in air, temperature $\leq$ 30 $^{\circ}$C, sample replaced after each analysis). The average amount of TiO_2 in the composites prepared by modified two-step method is over 60 wt.%.

The corresponding temporal UV-vis absorption spectra measurements obtained by using the FeOx-CoOx/TiO_2/polymer composite, prepared by modified (two-step) method, are shown in **Fig. 6-9**. The percentage amounts of MB adsorbed in 1 h on surface of the prepared TiO_2/polymer composites are shown in **Fig. 6-10**. All the samples adsorbed more than 10% of MB solution and the highest adsorption (~ 25%) was achieved with the FeOx/TiO_2/polymer sample.
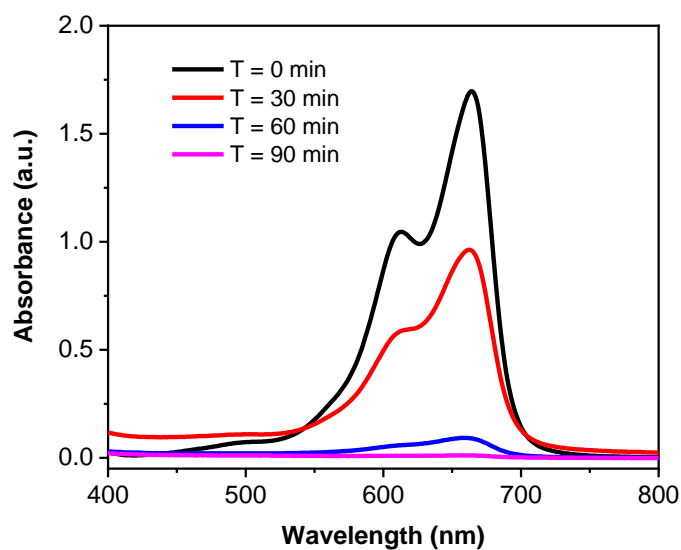
Figure 6-9 Temporal UV-vis absorption spectra of MB dye (10 mg/L, 10 mL, pH_{nat} = 6) during photocatalytic degradation by the FeOx-CoOx/TiO$_2$/polymer (sample replaced after each analysis).
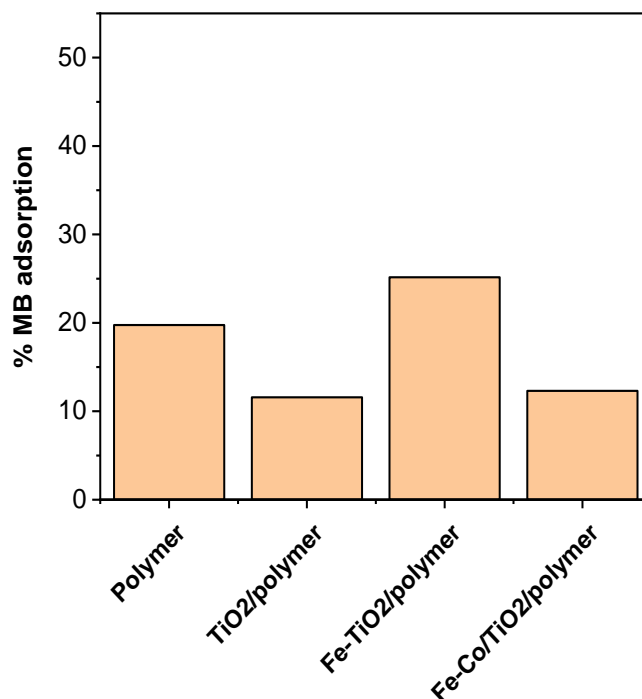
Figure 6-10 Percentage MB adsorptions in aqueous solution (10 mg/L, 10 mL, pH_{nat} = 6) in 1 h with various TiO$_2$/polymer composites prepared by modified (two-step) method.

The photocatalytic reduction abilities of the various TiO_2/polymer samples, prepared via the modified two-step method, were then evaluated by the conversion of Cr (VI) in the form of $K_2Cr_2O_7$. **Fig. 6-11** shows the UV-vis absorption spectra of Cr (VI) after photocatalytic Cr (VI) reduction experiments in 1 h. The corresponding sample vials containing residual Cr (VI) with 1,5-DPC dye after 1 h photocatalytic activity test are shown in **Fig. 6-12**. Relative to the initial Cr (VI) ion concentration, about 2% Cr (VI) reduction is achieved in the absence of polymer and photocatalyst, while about 7% Cr (VI) reduction is recorded by only the polymer as shown in **Fig. 6-13**. The highest photocatalytic Cr (VI) reduction is achieved with the FeOx-CoOx/TiO_2/polymer composite; recording nearly 100% Cr (VI) removal in 1 h. The Cr (VI) ions are reported to exist mainly in the form of CrO_4^{2-}, $Cr_2O_7^{2-}$ and $HCrO_4^{-}$ at low pH values < 6.5.[273,274] After complete photocatalytic Cr (VI) reduction, the formation of a green precipitate on drop-wise addition of a small amount of 1 M NaOH aqueous solution indicates the production of Cr (III) ions in solution as $Cr(OH)_3$.[275]
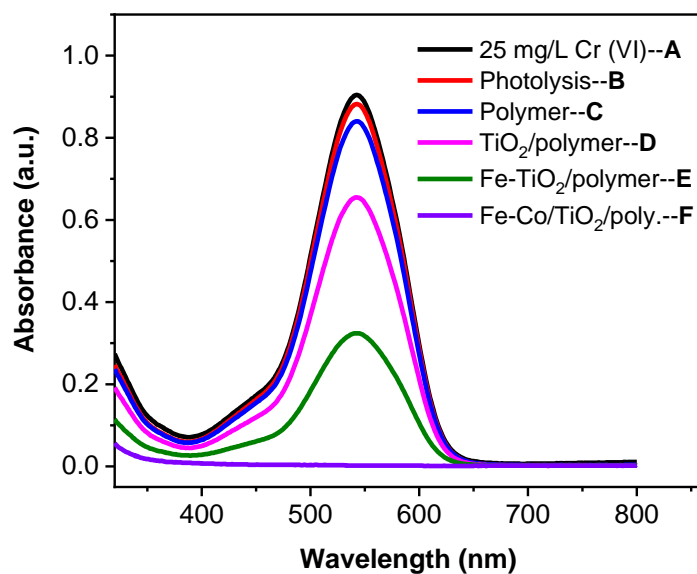
Figure 6-11 UV-vis absorption spectra of Cr (VI) solution in 1 h after photocatalytic conversion by various TiO_2/polymer composites prepared by modified (two-step) method.

Conditions: Cr (VI) solution (25 mg/L, 10 mL, pH_{nat} = 5.5, light λ = 302 nm, temperature ≤ 30 ^{o}C).
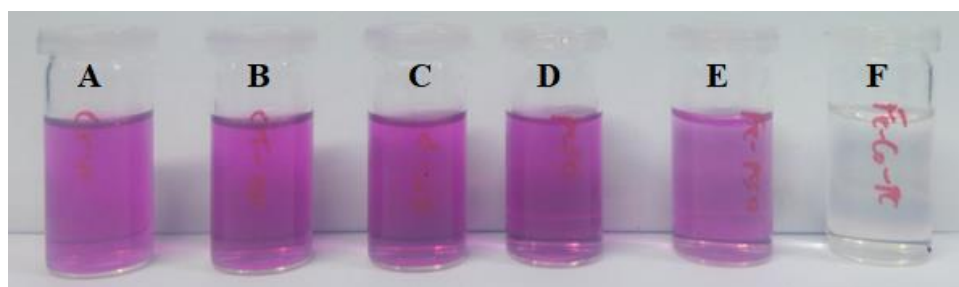
Figure 6-12 Image of Cr (VI) solutions after photocatalytic conversion by various TiO_2/polymer composites prepared by modified (two-step) method, and control experiment in 1 h (colorimetric determination with 1,5-DPC).

A is 25 mg/L Cr (VI) solution, B is photolysis, C is polymer, D is TiO_2/polymer, E is $FeOx$/TiO_2/polymer and F is $FeOx$-$CoOx$/TiO_2/polymer.
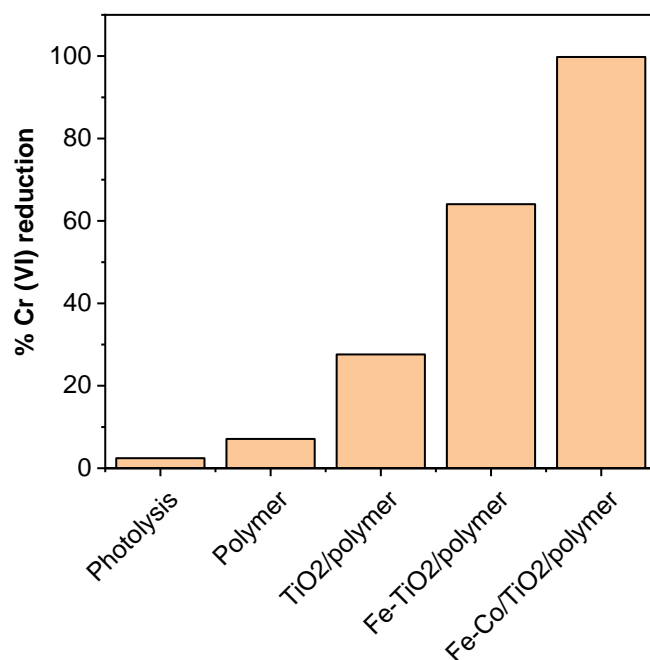
Figure 6-13 Percentage Cr (VI) reduction by various TiO_2/polymer composites in 1 h, prepared by modified (two-step) method.

Conditions: Cr (VI) solution (25 mg/L, 10 mL, pH_{nat} = 5.5, light λ = 302 nm, temperature ≤ 30 ^{o}C).

The percentage amounts of Cr (VI) adsorbed in 1 h on surface of the prepared TiO_2/polymer composites are shown in **Fig. 6-14**. The lowest adsorption is achieved by only the polymer (< 1%) and the highest adsorption (~ 15%) is achieved by the $FeOx$-$CoOx$/TiO_2/polymer sample. The 5 wt.% TiO_2/polymer composites, prepared by one step conventional method using two commercial TiO_2 powders (PC50 and P25), show minimal (< 10%) photocatalytic activity for Cr (VI) reduction as displayed in **Fig. 6-15**. Similar to the observation in MB degradation, this could be due to complete trapping of the TiO_2 nanoparticles in the polymer matrix, thus preventing the TiO_2 nanoparticles from participating in photocatalytic Cr (VI) reduction.
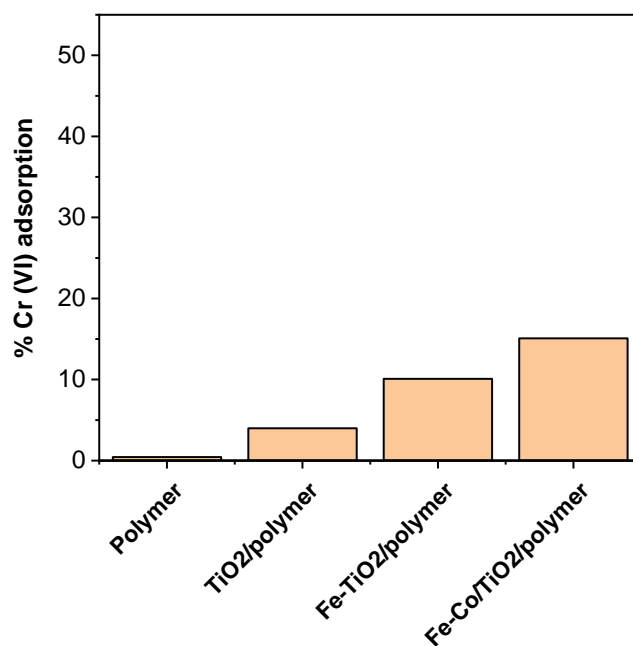
Figure 6-14 Percentage Cr (VI) ions adsorption in aqueous solution (25 mg/L, 10 mL, pH_{nat} = 5.5) in 1 h by various TiO_2/polymer composites (modified method).
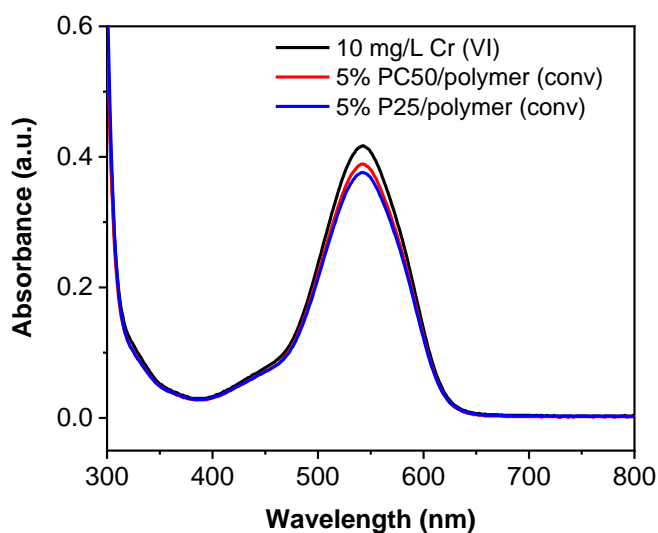
Figure 6-15 UV-vis absorption spectra of Cr (VI) solution in 1 h after photocatalytic conversion by prepared TiO_2/polymer composites (conventional method).

Conditions: Cr (VI) solution (10 mg/L, 10 mL, pH_{nat} = 5.5, light λ = 302 nm, temperature $\leq$ 30 ^{o}C).

6.3.3 Catalyst recycling

The stability of as-prepared FeOx-CoOx/TiO$_2$/polymer composite was evaluated for MB decomposition and Cr (VI) reduction as shown in **Figs. 6-16** and **6-17**, respectively. It can be seen that the photocatalytic activity of the composite did not decrease conspicuously after four successive cycles (4 x 1 hour) of photo-activity test, indicating that the composite is fairly stable. The catalyst recycling performance for MB decomposition ranges from 94 to 97% in 1 h, while it ranges from 97 to 100% in 1 h for Cr (VI) reduction.
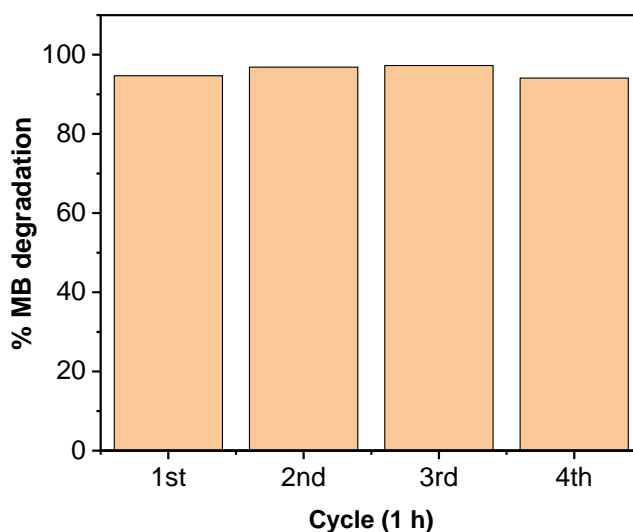
Figure 6-16 Recycling performance of FeOx-CoOx/TiO$_2$/polymer for MB degradation.
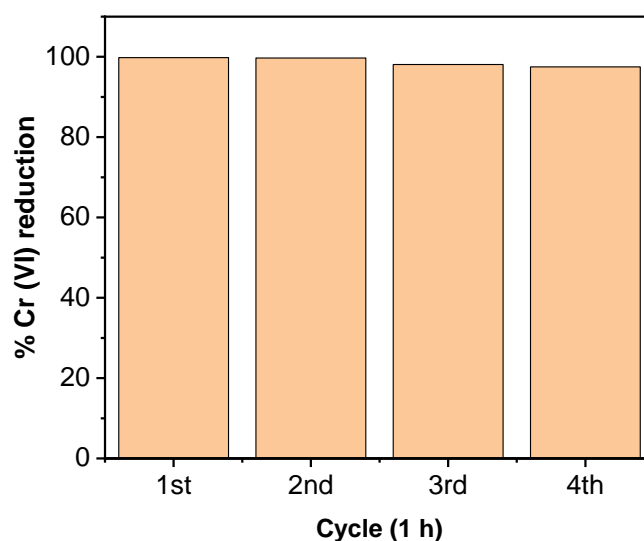
Figure 6-17 Recycling performance of FeOx-CoOx/TiO$_2$/polymer for Cr (VI) reduction.

Similar trends are observed during the photocatalytic degradation of MB dye and reduction of Cr (VI) in solution over the photocatalyst/polymer film prepared by the modified two-step method in the first 60 minutes. The polymer alone decomposes over 30% MB in 1 h, while it achieves less than 10% Cr (VI) conversion in 1 h. The TiO$_2$/polymer decomposes nearly 45% MB and about 30% Cr (VI) conversion in 1 h. The FeOx/TiO$_2$/polymer performs better than TiO$_2$/polymer with over 70% MB decomposition and nearly 65% Cr (VI) conversion. The optimised FeOx-CoOx/TiO$_2$/polymer sample performs best, with 95% MB decomposition and nearly 100% Cr (VI) conversion in 1 h. The obtained activity trends for the immobilised photocatalyst system are consistent with those obtained in slurry batch reactor system reported in Chapter 5.

6.3.4 Future work

A few more experiments would be carried out in this chapter in order to fully examine the surface and stability of prepared TiO_2/polymer composites, which cannot be carried out due to unavailability of equipment as a result of covid-19 pandemic over the past twelve (12) months.

1. Spectrofluorometric analysis for quantification of •OH radicals by using coumarin as a probe molecule. This study will provide insight into the degradation of MB dye over bare polymer.

2. Material characterisation using SEM-EDS to image the photocatalyst nanoparticles and show their dispersity in the polymer matrix before and after activity test. Also, XPS analysis to investigate the chemical state of elements in the FeOx-CoOx/TiO_2/polymer composite before and after immobilisation in polymer or activity test.

3. Quantitative analysis to confirm the production of Cr (III) from Cr (VI) ions using atomic absorption spectrometry (AAS).

4. Investigate the presence of photocatalyst particles in solution using ICP-MS to prove photocatalyst stability on polymer.

5. Investigate the effect of solution pH on the stability and activity of optimised TiO_2/polymer composite.

6. Investigate the polymer/TiO_2 composites for herbicides degradation.

7. Scale up the reactor vessel for wider application.

6.4   Conclusion

In summary, a facile two-step method was successfully used in immobilising cocatalyst-modified TiO_2 nanoparticles on plastic petri dishes with the help of a photo-curable polymer as a binder. The polymer resin/precursor was photo-polymerised by UV-B light irradiation. The photocatalytic performances of the TiO_2/polymer composites were evaluated for the decomposition of MB dye and the reduction of Cr (VI) to Cr (III) ions in aqueous solution. The highest photocatalytic MB degradation efficiency (97%) was achieved with FeOx-CoOx/TiO_2/polymer in 1 h, which is nearly two and half times higher than that of unmodified PC50 TiO_2/polymer sample. Also, nearly 100% Cr (VI) reduction was achieved in 1 h, whereas 28% Cr (VI) reduction was achieved with PC50/polymer, indicating more than a three-fold increase. The enhanced photo-generated electron-hole separation and the catalytic effect of FeOx-CoOx could have led to the efficient photocatalytic activity of the FeOx-CoOx/TiO_2/polymer composite towards MB and Cr (VI) decomposition. The satisfactory recycling performance of the optimised TiO_2/polymer composite indicates that the developed immobilisation technique could find application in pilot scale water treatment plants, self-cleaning surfaces and air purification.

7 Conclusions and Future work

7.1 Contribution to knowledge

Novel $FeOx-CoOx/TiO_2$ and $FeOx-CoOx/TiO_2$/polymer composites were successfully prepared and applied for the removal of herbicides and Cr (VI) from aqueous solution, respectively. The novel and optimised photocatalyst composites have not been reported in literature for photocatalytic water treatment.

7.2 Main findings

Preparation and application of $FeOOH/TiO_2$ in photocatalytic mineralisation of herbicides.

- The optimised and most efficient photocatalyst contained Fe (III) loading amount of 0.14 wt.% on TiO_2 prepared by a reliable wet impregnation method.

- Based on PXRD analysis, $Fe_4NO_3(OH)_{11}$ impurities and FeOOH were impregnated on surface of unmodified TiO_2 at 120 ^{o}C. FeOOH nanoparticles were the only decorating species at 250 ^{o}C, while at temperatures higher than 250 °C, Fe_2O_3 species dominated.

- No activity was observed during 2,4,6-TCP and 2,4-D photolysis in the absence of a photocatalyst.

- Unmodified TiO_2 was found to mineralise nearly 50% of 2,4,6-TCP in 4 h.

- Studies on the effect of calcination temperature on photocatalytic activity of the Fe(III)-decorated TiO_2 (0.14 wt.% Fe) samples showed that, ~ 100%, 85%, 62 % and 40% TOC removal were achieved in 4 h reaction by samples calcined at 120, 250, 350 and 450 ^oC, respectively.

- The sample calcined at 250 ^oC (FeOOH/TiO_2) displayed both excellent photocatalytic mineralisation efficiency (nearly double activity of unmodified PC50 TiO_2) and better photocatalytic stability after three successive degradation cycles than the sample calcined at 120 ^oC. This was due to the instability of $Fe_4NO_3(OH)_{11}$ as the primary decorating cocatalyst on TiO_2 calcined at 120 ^oC.

- The 2,4,6-TCP degradation process followed pseudo-first-order kinetics model on both TiO_2 and optimised FeOOH/TiO_2 with initial rate constants of 0.00647 and 0.0193 min^{-1}, respectively, indicating a three-fold enhancement.

- The adsorption-desorption equilibrium of 2,4,6-TCP aqueous solution on optimised FeOOH/TiO_2 was achieved in the first 30 min with about 10% 2,4,6-TCP removal in 4 h.

- The FeOOH/TiO_2 sample recorded 95% TOC removal in 3 h run for another widely used herbicide, 2,4-D, while 60% TOC removal was achieved by the unmodified TiO_2 sample.

- The mechanistic studies with reactive oxygen species scavengers demonstrated that the degradation of 2,4,6-TCP was primarily controlled by hydroxyl radicals and superoxide radicals.

- PL measurements confirmed the enhanced photo-generated electron-hole separation, while in situ ESR confirmed the catalytic effect of FeOOH for improved generation of hydroxyl radicals, thus led to high photocatalytic activity.

- Six different intermediate products were successfully identified from HPLC-MS analysis of partially degraded 2,4,6-TCP solution, and a possible degradation pathway of 2,4,6-TCP was proposed.

Based upon the success of the optimised Fe(III)-decorated TiO_2 sample, the influence of binary cocatalyst alloying was investigated. The studies on the effect of individual cocatalysts (Fe, Cu and Co) and concentrations (0.05, 0.1 and 0.5 wt.%), towards complete 2,4,6-TCP mineralisation were carried out under similar operating conditions.

- The optimised loading amount was found to be 0.1 wt.% metal for the three cocatalysts (FeOx, CuOx and CoOx).

- XPS analysis indicated that FeOOH, CuO and CoO were impregnated on the surface of TiO_2.

- The TOC removal rates for 2,4,6-TCP mineralisation by the individual cocatalyst-decorated TiO_2 samples indicated that CuOx cocatalyst performed best, then, CoOx and the last FeOx.

- CuOx showed around 73% TOC removal efficiency, while FeOx and CoOx showed around 62% and 64% TOC removal efficiencies in 3 h, respectively.

- The investigation on the effect of binary cocatalyst loading (FeOx-CuOx and FeOx-CoOx) on TiO_2 surface were carried out by fixing loading concentration (0.1 wt.%) for each cocatalyst, the novel FeOx-CoOx alloy exhibited the highest photocatalytic activity for 2,4,6-TCP mineralisation.

- About 92% TOC removal was achieved in 3 h by the novel FeOx-CoOx/TiO_2 (nearly 50% higher than the FeOOH/TiO_2 reported before), while about 75% TOC removal efficiency was achieved by FeOx-CuOx/TiO_2.

- The 2,4,6-TCP mineralisation efficiency achieved by FeOx-CoOx/TiO_2 in 3 h was about two and half times higher than the unmodified PC50 TiO_2.

- HPLC analysis showed that the 2,4,6-TCP degradation rate by FeOx-CoOx/TiO_2 was about 100% in 3 h . This indicated that the 2,4,6-TCP degradation rate was faster compared to mineralisation rate, which is consistent with results reported in the literature.

- Studies on effect of light irradiation wavelength indicated that no 2,4,6-TCP degradation activity was recorded above 395 nm, while about 60% and 93% TOC removal in 2 h were achieved at above 320 nm and above 260 nm, respectively by the FeOx-CoOx/TiO_2 sample.

- For another widely used herbicide (2,4-D), the FeOx-CoOx/TiO$_2$ sample recorded nearly 100% TOC removal in 3 h and about 95% degradation in 60 min. The 2,4-D mineralisation efficiency achieved by FeOx-CoOx/TiO$_2$ in 3 h was about one and half times (150%) compared to unmodified PC50 TiO$_2$.

- Spectrofluorometric analysis for $^\bullet$OH radical generation, with coumarin as a probe molecule, confirmed the catalytic effect of FeOx-CoOx on TiO$_2$ for improved generation of hydroxyl radicals, thus higher photocatalytic activity for mineralisation of selected organic compounds.

Based upon the success of the optimised FeOx-CoOx-decorated TiO$_2$ nanoparticle sample, the prepared TiO$_2$-based photocatalysts (TiO$_2$, FeOx/TiO$_2$ and FeOx-CoOx/TiO$_2$) were immobilised on an acrylate-based polymer to generate a film for real application. The TiO$_2$/polymer composites were evaluated for the photocatalytic oxidation of MB dye and reduction of hexavalent chromium (Cr^{6+}) ions in aqueous solution to the less toxic Cr^{3+} ions.

- The FeOx-CoOx-TiO$_2$/polymer was found to show the highest photocatalytic activity in both MB oxidation and Cr (VI) reduction studies.

- About 97% MB got degraded in 1 h by the optimised FeOx-CoOx/TiO$_2$-based polymer composite, while TiO$_2$/polymer and

$FeOx/TiO_2$/polymer recorded 40 and 70% MB oxidation, respectively.

- About 99% Cr (VI) was reduced to Cr (III) ions in 1 h by the optimised $FeOx\text{-}CoOx/TiO_2$/polymer sample, while TiO_2/polymer and $FeOx/TiO_2$/polymer achieved 28 and 64% Cr (VI) reduction efficiency, respectively.

- The $FeOx\text{-}CoOx/TiO_2$ sample was found to maintain its outstanding photocatalytic efficiency in both suspension and fixed-bed water treatment set-ups.

- The results of catalyst recycling performance showed that the $FeOx\text{-}CoOx/TiO_2$/polymer was highly stable after four successive cycles, indicating its strong potential for the real application of photocatalytic oxidation of organic compounds and reduction of heavy metal ions in water.

7.3 Future work

The main goals of the thesis have been achieved, including the enhancement of the photocatalytic activity of commercial PC50 TiO_2 by novel binary cocatalysts, in the complete mineralisation of persistent organic water pollutants in both suspension and fixed-bed systems. Despite these achievements, more work still need to be performed in the area of photocatalysts characterisation and fundamental understanding of the reaction mechanism, which is significant while can not be investigated so far

due to the unavailability of the related facility caused by the lockdown related to the pandemic since March 2020. Also, other limitations confronting this water treatment technology need to be fully addressed for standalone applications or integrated with conventional water treatment technologies.

As mentioned in Chapter 5, XPS analysis was carried out to identify the decorated cocatalyst species, which were indicated to be FeOOH, CuO and CoO. However, more work still need to be done using PXRD to further confirm the three cocatalyst species and possibility of forming binary alloys. This will be carried out by substituting TiO_2 with silica or alumina as the substrate, for easy identification, due to the high background signals obtained with TiO_2 as reported in literature. Also, high resolution TEM-EDS analysis will further confirm the presence of either cocatalysts' islands or formation of binary alloys on TiO_2.

Apart from the spectrofluorometric analysis reported for generation of $^{\bullet}OH$ radicals by the optimised FeOx-CoOx/TiO_2 sample in Chapter 5, there is a need to use a more advanced method, ESR, to investigate the production rate of both hydroxyl and superoxide radicals as reported in Chapter 4. Also, studies on the effect of radical scavengers on 2,4,6-TCP mineralisation need to be carried out as did in Chapter 4. This will assist in fundamental understanding of the photocatalytic reaction mechanism of the FeOx-CoOx/TiO_2. There is also a need for in-depth investigation of charge kinetics, which involves charge separations' transport and recombination in

semiconductor photocatalysts. This will help in rational photocatalyst design strategy to enhance the photo-activity for water treatment. Transient absorption spectroscopy (TAS) is a very sensitive technique used in investigating charge carrier dynamics. The transient absorption spectra can assist in probing the lifetime of photo-generated holes and electrons, in semiconductors as well as their recombination rate (within the nanoseconds to milliseconds timescale).

More studies need to be carried out in Chapter 6 on the FeOx-CoOx/TiO$_2$/polymer sample to investigate the potential release of TiO$_2$ during exposure to UV irradiation by Inductively coupled plasma mass spectrometry (ICP-MS) analysis of the solution. SEM analysis of the sample, before and after photocatalytic degradation experiments, will confirm the stability of the optimised TiO$_2$/polymer composite. There is a need to repeat the photocatalytic activity results of FeOx-CoOx/TiO$_2$/polymer sample in Chapter 6 with the degradation of herbicides, so as to compare with results obtained in Chapter 4 and 5. This could not be completed due to covid-19 pandemic and faulty HPLC. Also, the technology will be tested using natural water, in order to investigate the influence of dissolved ions on the photocatalytic degradation rates of herbicides by the optimised FeOx-CoOx/TiO$_2$/polymer composite.

As mentioned in Chapter 6, the TiO$_2$/polymer composites prepared via conventional one-step mixing method, displayed lower activities for the degradation of MB and reduction of Cr (VI), unlike the TiO$_2$/polymer

composites prepared via two-step modified method. More work needs to be done (e.g. effect of solution pH, polymer degradation and toxicity tests) to fully investigate polymers as a potential substrate, unlike conventional ones (glass beads, carbon fibres, aluminium plate, cement/concrete etc.), which have their individual drawbacks.

Finally, in this project, lab simulated wastewater was used against natural water (i.e. industrial effluents, stream, pond, river, groundwater etc). For practical application, natural water samples that include dissolved natural organic matter (NOM) and inorganic salts should be used to investigate herbicide mineralisation efficiency and kinetics. Also, testing of a mixed solution of contaminants using natural water such as treated secondary wastewater or river/lake water should be investigated. The effect of initial herbicide concentration on degradation rate should be investigated, especially more realistic concentrations at µg/L found in water and wastewater. Tests at pilot scale will inform the water industry about the application of the technology in practice and how this technology will be recovered once the system is not effective.

8 References

(1) Ahmed, S.; Rasul, M. G.; Martens, W. N.; Brown, R.; Hashib, M. A. Heterogeneous Photocatalytic Degradation of Phenols in Wastewater: A Review on Current Status and Developments. *Desalination* **2010**, *261* (1–2), 3–18.

(2) Kolpin, D. W.; Meyer, M. T. Pharmaceuticals , Hormones , and Other Organic Wastewater Contaminants in U . S . Streams, 1999 - 2000 : A National Reconnaissance. *Environ. Sci. Technol.* **2002**, *36* (6), 1202–1211.

(3) Schriks, M.; Leerdam, J. a Van; Linden, S. C. Van Der; Burg, B. Van Der; Wezel, a P. Van; Voogt, P. De. High-Resolution Mass Spectrometric Identification and Quantification of Glucucorticoid Compounds in Various Wastewaters in the Netherlands. *Environ. Sci. Technol.* **2010**, *44* (12), 4766–4774.

(4) ATSDR. Comprehensive Environmental Response, Compensation, and Liability Act (CERCLA) Priority List of Hazardous Substances. **2007**.

(5) Häggblom, M. M.; Bossert, I. D. *Halogenated Organic Compounds – a Global Perspective*; Kluwer Academic Publishers: Boston, Mass, **2003**.

(6) The Water Supply (Water Quality) Regulations*, Wales Statutory Instruments, (W. 121) SCHEDULE 1*; United Kingdom, **2018**; p 647.

(7)   Al-Asheh, S.; Banat, F.; Abu-Aitah, L. Adsorption of Phenol Using Different Types of Activated Bentonites. *Sep. Purif. Technol.* **2003**, *33* (1), 1–10.

(8)   Murcia, J. J.; Hidalgo, M. C.; Navío, J. A.; Araña, J.; Doña-Rodríguez, J. M. Study of the Phenol Photocatalytic Degradation over TiO_2 Modified by Sulfation, Fluorination, and Platinum Nanoparticles Photodeposition. *Appl. Catal. B Environ.* **2015**, *179*, 305–312.

(9)   Yang, C. F.; Lee, C. M. Pentachlorophenol Contaminated Groundwater Bioremediation Using Immobilized Sphingomonas Cells Inoculation in the Bioreactor System. *J. Hazard. Mater.* **2008**, *152* (1), 159–165.

(10)   Murcia, M.D., Gomez, M., Gomez, E., Gomez, J.L., Sinada, F.A., Christofi, N. Degradation of 4-Chlorophenol Using Pseudomonas Putida. *Chem. Eng.* **2007**, *10*, 2–4.

(11)   Olaniran, A. O.; Igbinosa, E. O. Chlorophenols and Other Related Derivatives of Environmental Concern: Properties, Distribution and Microbial Degradation Processes. *Chemosphere.* May **2011**, pp 1297–1306.

(12)   ATSDR. Toxicological Profile for Chlorophenols, US Department of Health and Human Services. Atlanta, GA. **1999**.

(13)   Czaplicka, M. Sources and Transformations of Chlorophenols in the Natural Environment. *Sci. Total Environ.* **2004**, *322* (1–3), 21–39.

(14) U.S. EPA. *Edition of the Drinking Water Standards and Health Advisories*; Washington, DC, USA, **2004**.

(15) Karci, A.; Arslan-Alaton, I.; Olmez-Hanci, T.; Bekbölet, M. Transformation of 2,4-Dichlorophenol by H_2O_2/UV-C, Fenton and Photo-Fenton Processes: Oxidation Products and Toxicity Evolution. *J. Photochem. Photobiol. A Chem.* **2012**, *230* (1), 65–73.

(16) Ollis, D. F.; Al-Ekabi, H. Photocatalytic Purification and Treatment of Water and Air. Elsevier, Amsterdam 1993.

(17) Bandara, J.; Mielczarski, J. .; Lopez, A.; Kiwi, J. 2. Sensitized Degradation of Chlorophenols on Iron Oxides Induced by Visible Light. *Appl. Catal. B Environ.* **2001**, *34* (4), 321–333.

(18) Zangeneh, H.; Zinatizadeh, A. A. L.; Habibi, M.; Akia, M.; Isa, M. H. Journal of Industrial and Engineering Chemistry Photocatalytic Oxidation of Organic Dyes and Pollutants in Wastewater Using Different Modified Titanium Dioxides : A Comparative Review. *J. Ind. Eng. Chem.* **2015**, *26*, 1–36.

(19) Gutarra, A.; Litter, M. I. Photodegradation of an Azo Dye of the Textile Industry. *Chemosphere* **2002**, *48*, 393–399.

(20) Konsowa, A. H.; Ossman, M. E.; Chen, Y.; Crittenden, J. C. Decolorization of Industrial Wastewater by Ozonation Followed by Adsorption on Activated Carbon. *J. Hazard. Mater.* **2010**, *176*, 181–185.

(21) Venkatachalam, N.; Palanichamy, M.; Murugesan, V. Sol–Gel Preparation and Characterization of Alkaline Earth Metal Doped Nano TiO$_2$: Efficient Photocatalytic Degradation of 4-Chlorophenol. *J. Mol. Catal. A Chem.* **2007**, *273* (1–2), 177–185.

(22) Ray, A. K.; Beenackers, A. A. C. M. Novel Photocatalytic Reactor for Water Purification. *AIChE J.* **1998**, *44* (2), 477–483.

(23) Moniz, S. J. A.; Shevlin, S. A.; An, X.; Guo, Z.; Tang, J. Fe$_2$O$_3$ -TiO $_2$ Nanocomposites for Enhanced Charge Separation and Photocatalytic Activity. *Chem. - A Eur. J.* **2014**, *20* (47), 15571–15579.

(24) Yang, L.; Yu, L. E.; Ray, M. B. Photocatalytic Oxidation of Paracetamol: Dominant Reactants, Intermediates, and Reaction Mechanisms. *Environ. Sci. Technol.* **2009**, *43* (2), 460–465.

(25) Khataee, A. R.; Kasiri, M. B. Photocatalytic Degradation of Organic Dyes in the Presence of Nanostructured Titanium Dioxide: Influence of the Chemical Structure of Dyes. *J. Mol. Catal. A Chem.* **2010**, *328* (1–2), 8–26.

(26) The Water Project (USA). "Improving Health in Africa." Web accessed July 24, **2021**. https://thewaterproject.org/why-water/health.

(27) Owa, F. D. Water Pollution : Sources, Effects, Control and Management. *Mediterr. J. Soc. Sci.* **2013**, *4* (8), 65–68.

(28) E. & F. Spon. *Water Pollution Control - A Guide to the Use of Water Quality Management Principles Edited by Richard Helmer and*

Ivanildo Hespanhol Published on Behalf of the United Nations Environment Programme, the Water Supply & Sanitation Collaborative Council and Th; WHO/UNEP, **1997**.

(29)   Onekutu, A.; Nnamonu, L. A. Green Pesticides in Nigeria : An Overview. *J. Biol. Agric. Healthc.* **2015**, *5* (9), 48–63.

(30)   Erhunmwunse, N.; Dirisu, A.; Olomukoro, J. Implications of Pesticide Usage in Nigeria. *Trop. Freshw. Biol.* **2013**, *21* (1).

(31)   Dong, H.; Zeng, G.; Tang, L.; Fan, C. An Overview on Limitations of TiO_2 -Based Particles for Photocatalytic Degradation of Organic Pollutants and the Corresponding Countermeasures. *Water Res.* **2015**, *79*, 128–146.

(32)   Park, H.; Park, Y.; Kim, W.; Choi, W. Surface Modification of TiO_2 Photocatalyst for Environmental Applications. *J. Photochem. Photobiol. C Photochem. Rev.* **2013**, *15* (1), 1–20.

(33)   Wu, W.; Roy, V. A. L. Recent Progress in Magnetic Iron Oxide – Semiconductor Composite Nanomaterials as Promising Photocatalysts. **2015**, 38–58.

(34)   R. Vinu; Madras, G. Environmental Remediation by Photocatalysis. *J. Indian Inst. Sci.* **2010**, *90* (2), 189–230.

(35)   Saito, H.; Nosaka, Y. Mechanism of Singlet Oxygen Generation in Visible-Light-Induced Photocatalysis of Gold-Nanoparticle-Deposited Titanium Dioxide. *J. Phys. Chem. C* **2014**, *118* (29), 15656–15663.

(36) Zhang, X.; Chen, Y. L.; Liu, R. S.; Tsai, D. P. Plasmonic Photocatalysis. *Reports Prog. Phys.* **2013**, *76* (4).

(37) Hirakawa, T.; Nosaka, Y. Properties of $O_2^{\bullet-}$ and $OH^{\bullet}$ Formed in TiO_2 Aqueous Suspensions by Photocatalytic Reaction and the Influence of H_2O_2 and Some Ions. *Langmuir* **2002**, *18* (8), 3247–3254.

(38) Etacheri, V.; Seery, M. K.; Hinder, S. J.; Pillai, S. C. Oxygen Rich Titania: A Dopant Free, High Temperature Stable, and Visible-Light Active Anatase Photocatalyst. *Adv. Funct. Mater.* **2011**, *21* (19), 3744–3752.

(39) Nolan, N. T.; Seery, M. K.; Hinder, S. J.; Healy, L. F.; Pillai, S. C. A Systematic Study of the Effect of Silver on the Chelation of Formic Acid to a Titanium Precursor and the Resulting Effect on the Anatase to Rutile Transformation of TiO_2. *J. Phys. Chem. C* **2010**, *114* (30), 13026–13034.

(40) Greenwood, N. N.; Earnshaw, A. *Chemistry of the Elements*; Pergamon Press, Oxford, **1984**.

(41) Dunlop, P. S. M.; Galdi, A.; McMurray, T. A.; Hamilton, J. W. J.; Rizzo, L.; Byrne, J. A. Comparison of Photocatalytic Activities of Commercial Titanium Dioxide Powders Immobilised on Glass Substrates. *J. Adv. Oxid. Technol.* **2010**, *13* (1), 99.

(42) Adamek, E.; Baran, W.; Ziemiańska, J.; Sobczak, A. Effect of $FeCl_3$ on Sulfonamide Removal and Reduction of Antimicrobial Activity of

Wastewater in a Photocatalytic Process with TiO_2. *Appl. Catal. B Environ.* **2012**, *126*, 29–38.

(43) Garcia-Segura, S.; Dosta, S.; Guilemany, J. M.; Brillas, E. Solar Photoelectrocatalytic Degradation of Acid Orange 7 Azo Dye Using a Highly Stable TiO_2 Photoanode Synthesized by Atmospheric Plasma Spray. *Appl. Catal. B Environ.* **2013**, *132–133*, 142–150.

(44) Ortega-Liébana, M. C.; Sánchez-López, E.; Hidalgo-Carrillo, J.; Marinas, A.; Marinas, J. M.; Urbano, F. J. A Comparative Study of Photocatalytic Degradation of 3-Chloropyridine under UV and Solar Light by Homogeneous (Photo-Fenton) and Heterogeneous (TiO_2) Photocatalysis. *Appl. Catal. B Environ.* **2012**, *127*, 316–322.

(45) Legrini, O.; Oliveros, E.; Braun, A. M. Photochemical Processes for Water Treatment. *Chem. Rev.* **1993**, *93* (2), 671–698.

(46) Perkowski, J.; Bzdon, S.; Bulska, A.; Jóźwiak, W. K. Decomposition of Detergents Present in Car-Wash Sewage by Titania Photo-Assisted Oxidation. *Polish J. Environ. Stud.* **2006**, *15* (3), 457–465.

(47) Kozak, A. J.; Wieczorek-Ciurowa, K. THE THERMAL DECOMPOSITION OF $Fe(NO_3)_3 \times 9H_2O$. *J. Therm. Anal. Calorim.* **1999**, *58* (3), 647–651.

(48) Xu, J.; Xu, Z.; Zhang, M.; Xu, J.; Fang, D.; Ran, W. Impregnation Synthesis of TiO_2/Hydroniumjarosite Composite with Enhanced Property in Photocatalytic Reduction of Cr (VI). *Mater. Chem. Phys.*

2015, *152*, 4–8.

(49) Zaleska, A. Doped-TiO$_2$: A Review. *Recent Patents Eng.* **2008**, *2* (3), 157–164.

(50) Han, C.; Likodimos, V.; Khan, J. A.; Nadagouda, M. N.; Andersen, J.; Falaras, P.; Rosales-Lombardi, P.; Dionysiou, D. D. UV–Visible Light-Activated Ag-Decorated, Monodisperse TiO$_2$ Aggregates for Treatment of the Pharmaceutical Oxytetracycline. *Environ. Sci. Pollut. Res.* **2014**, *21* (20), 11781–11793.

(51) Zang, Y.; Farnood, R. Photocatalytic Activity of AgBr/TiO$_2$ in Water under Simulated Sunlight Irradiation. *Appl. Catal. B Environ.* **2008**, *79* (4), 334–340.

(52) Hu, C.; Lan, Y.; Qu, J.; Hu, X.; Wang, A. Ag/AgBr/TiO$_2$ Visible Light Photocatalyst for Destruction of Azodyes and Bacteria. *J. Phys. Chem.* **2006**, *110*, 4066–4072.

(53) Arabatzis, I. M.; Stergiopoulos, T.; Bernard, M. C.; Labou, D.; Neophytides, S. G.; Falaras, P. Silver-Modified Titanium Dioxide Thin Films for Efficient Photodegradation of Methyl Orange. *Appl. Catal. B Environ.* **2003**, *42* (2), 187–201.

(54) Fuerte, A.; Hernández-Alonso, M. D.; Maira, A. J.; Martínez-Arias, A.; Fernández-García, M.; Conesa, J. C.; Soria, J. Visible Light-Activated Nanosized Doped-TiO$_2$ Photocatalysts. *Chem. Commun.* **2001**, No. 24, 2718–2719.

(55) Anpo, M. Use of Visible Light. Second-Generation Titanium Oxide Photocatalysts Prepared by the Application of an Advanced Metal Ion-Implantation Method. *Pure Appl. Chem.* **2000**, *72* (9), 1787–1792.

(56) Soria, J.; Conesa, J. C.; Schiavello, M.; Sclafani, A. Dinitrogen Photoreduction to Ammonia over Titanium Dioxide Powders Doped with Ferric Ions. *J. Phys. Chem.* **1991**, *95* (6), 274–282.

(57) Palmisano, L.; Schiavello, M.; Sclafani, A.; Martin, C.; Martin, I.; Rives, V. Surface Properties of Iron-Titania Photocatalysts Employed for 4-Nitrophenol Photodegradation in Aqueous TiO_2 Dispersion. *Catal. Letters* **1994**, *24* (3–4), 303–315.

(58) Iliev, V.; Tomova, D.; Bilyarska, L.; Eliyas, A.; Petrov, L. Photocatalytic Properties of TiO_2 Modified with Platinum and Silver Nanoparticles in the Degradation of Oxalic Acid in Aqueous Solution. *Appl. Catal. B Environ.* **2006**, *63* (3–4), 266–271.

(59) Chen, D.; Jiang, Z.; Geng, J.; Wang, Q.; Yang, D. Carbon and Nitrogen Co-Doped TiO_2 with Enhanced Visible-Light Photocatalytic Activity. *Ind. Eng. Chem. Res.* **2007**, *46* (9), 2741–2746.

(60) Li, X.; Wang, D.; Cheng, G.; Luo, Q.; An, J.; Wang, Y. Preparation of Polyaniline-Modified TiO_2 Nanoparticles and Their Photocatalytic Activity under Visible Light Illumination. *Appl. Catal. B Environ.* **2008**, *81* (3–4), 267–273.

(61) Dong, F.; Guo, S.; Wang, H.; Li, X.; Wu, Z. Enhancement of the

Visible Light Photocatalytic Activity of C-Doped TiO_2 Nanomaterials Prepared by a Green Synthetic Approach. *J. Phys. Chem. C* **2011**, *115* (27), 13285–13292.

(62)   Chen, X.; Liu, L.; Yu, P. Y.; Mao, S. S. Increasing Solar Absorption for Photocatalysis with Black Hydrogenated Titanium Dioxide Nanocrystals. *Science (80-.).* **2011**, *331* (6018), 746–750.

(63)   Wang, Z.; Yang, C.; Lin, T.; Yin, H.; Chen, P.; Wan, D.; Xu, F.; Huang, F.; Lin, J.; Xie, X.; et al. Visible-Light Photocatalytic, Solar Thermal and Photoelectrochemical Properties of Aluminium-Reduced Black Titania. *Energy Environ. Sci.* **2013**, *6* (10), 3007.

(64)   Zhao, Z.; Tan, H.; Zhao, H.; Lv, Y.; Zhou, L.-J.; Song, Y.; Sun, Z. Reduced TiO_2 Rutile Nanorods with Well-Defined Facets and Their Visible-Light Photocatalytic Activity. *Chem. Commun.* **2014**, *50* (21), 2755–2757.

(65)   Zou, X.; Liu, J.; Su, J.; Zuo, F.; Chen, J.; Feng, P. Facile Synthesis of Thermal- and Photostable Titania with Paramagnetic Oxygen Vacancies for Visible-Light Photocatalysis. *Chem. - A Eur. J.* **2013**, *19* (8), 2866–2873.

(66)   Kang, Q.; Cao, J.; Zhang, Y.; Liu, L.; Xu, H.; Ye, J. Reduced TiO_2 Nanotube Arrays for Photoelectrochemical Water Splitting. *J. Mater. Chem. A* **2013**, *1* (18), 5766–5774.

(67)   Tominaka, S.; Tsujimoto, Y.; Matsushita, Y.; Yamaura, K. Synthesis of

Nanostructured Reduced Titanium Oxide: Crystal Structure Transformation Maintaining Nanomorphology. *Angew. Chemie - Int. Ed.* **2011**, *50* (32), 7418–7421.

(68) Xu, C.; Song, Y.; Lu, L.; Cheng, C.; Liu, D.; Fang, X.; Chen, X.; Zhu, X.; Li, D. Electrochemically Hydrogenated TiO_2 Nanotubes with Improved Photoelectrochemical Water Splitting Performance. *Nanoscale Res. Lett.* **2013**, *8* (1), 1–7.

(69) Diebold, U. The Surface Science of Titanium Dioxide. *Surf. Sci. Rep.* **2003**, *48* (5–8), 53–229.

(70) Chen, X.; Liu, L.; Huang, F. Black Titanium Dioxide (TiO_2) Nanomaterials. *Chem. Soc. Rev.* **2015**, *44* (7), 1861–1885.

(71) Makarova, O. V; Rajh, T.; Thurnauer, M. C.; Martin, A.; Kemme, P. A.; Cropek, D. Surface Modification of TiO_2 Nanoparticles For Photochemical Reduction of Nitrobenzene. *Environ. Sci. Technol.* **2000**, *34* (22), 4797–4803.

(72) Wang, Y.; Zhang, J.; Liu, X.; Gao, S.; Huang, B.; Dai, Y.; Xu, Y. Synthesis and Characterization of Activated Carbon-Coated $SiO_2/TiO_{2-X}C_x$ Nanoporous Composites with High Adsorption Capability and Visible Light Photocatalytic Activity. *Mater. Chem. Phys.* **2012**, *135* (2–3), 579–586.

(73) Nguyen-Phan, T. D.; Pham, V. H.; Shin, E. W.; Pham, H. D.; Kim, S.; Chung, J. S.; Kim, E. J.; Hur, S. H. The Role of Graphene Oxide

Content on the Adsorption-Enhanced Photocatalysis of Titanium Dioxide/Graphene Oxide Composites. *Chem. Eng. J.* **2011**, *170* (1), 226–232.

(74) Carp, O.; Huisman, C. L.; Reller, A. Photoinduced Reactivity of Titanium Dioxide. *Prog. Solid State Chem.* **2004**, *32* (1–2), 33–177.

(75) Liu, K.; Zhu, L.; Jiang, T.; Sun, Y.; Li, H.; Wang, D. Mesoporous TiO_2 Micro-Nanometer Composite Structure: Synthesis, Optoelectric Properties, and Photocatalytic Selectivity. *Int. J. Photoenergy* **2012**, *2012*.

(76) Mascolo, G.; Comparelli, R.; Curri, M. L.; Lovecchio, G.; Lopez, A.; Agostiano, A. Photocatalytic Degradation of Methyl Red by TiO_2: Comparison of the Efficiency of Immobilized Nanoparticles versus Conventional Suspended Catalyst. *J. Hazard. Mater.* **2007**, *142* (1–2), 130–137.

(77) Weng, Y.-X.; Li, L.; Liu, Y.; Wang, L.; Yang, G.-Z. Surface-Binding Forms of Carboxylic Groups on Nanoparticulate TiO_2 Surface Studied by the Interface-Sensitive Transient Triplet-State Molecular Probe. *J. Phys. Chem. B* **2003**, *107* (18), 4356–4363.

(78) Mallakpour, S.; Nikkhoo, E. Surface Modification of Nano-TiO_2 with Trimellitylimido-Amino Acid-Based Diacids for Preventing Aggregation of Nanoparticles. *Adv. Powder Technol.* **2014**, *25* (1), 348–353.

(79) Nakayama, N.; Hayashi, T. Preparation and Characterization of

Poly(l-Lactic Acid)/TiO_2 Nanoparticle Nanocomposite Films with High Transparency and Efficient Photodegradability. *Polym. Degrad. Stab.* **2007**, *92* (7), 1255–1264.

(80) Uyguner, C.; Bekbolet, M. Application of Photocatalysis for the Removal of Natural Organic Matter in Simulated Surface and Ground Waters. *J. Adv. Oxid. Technol.* **2016**, *12* (1), 87–92.

(81) Matthews, R. W. Purification of Water with Near-u.v. Illuminated Suspensions of Titanium Dioxide. *Water Res.* **1990**, *24* (5), 653–660.

(82) Deng, Y.; Qi, D.; Deng, C.; Zhang, X.; Zhao, D. Superparamagnetic High-Magnetization Microspheres with an $Fe_3O_4@SiO_2$ Core and Perpendicularly Aligned Mesoporous SiO_2 Shell for Removal of Microcystins. *J. Am. Chem. Soc.* **2008**, *130* (1), 28–29.

(83) Zhang, X.; Wu, F.; Deng, N. Efficient Photodegradation of Dyes Using Light-Induced Self Assembly TiO_2/β-Cyclodextrin Hybrid Nanoparticles under Visible Light Irradiation. *J. Hazard. Mater.* **2011**, *185* (1), 117–123.

(84) Zhang, H.; Zhu, G. One-Step Hydrothermal Synthesis of Magnetic Fe_3O_4 Nanoparticles Immobilized on Polyamide Fabric. *Appl. Surf. Sci.* **2012**, *258* (11), 4952–4959.

(85) Wang, S.; Zhou, S. Titania Deposited on Soft Magnetic Activated Carbon as a Magnetically Separable Photocatalyst with Enhanced Activity. *Appl. Surf. Sci.* **2010**, *256* (21), 6191–6198.

(86) He, Z.; Hong, T.; Chen, J.; Song, S. A Magnetic TiO_2 Photocatalyst Doped with Iodine for Organic Pollutant Degradation. *Sep. Purif. Technol.* **2012**, *96*, 50–57.

(87) Martyanov, I. N.; Klabunde, K. J. Comparative Study of TiO_2 Particles in Powder Form and as a Thin Nanostructured Film on Quartz. *J. Catal.* **2004**, *225* (2), 408–416.

(88) Tang, Y.; Zhang, G.; Liu, C.; Luo, S.; Xu, X. Magnetic TiO_2-Graphene Composite as a High-Performance and Recyclable Platform for Efficient Photocatalytic Removal of Herbicides from Water. *J. Hazard. Mater.* **2013**, *252–253*, 115–122.

(89) Wang, C.; Yin, L.; Zhang, L.; Kang, L.; Wang, X.; Gao, R. Magnetic (γ-Fe_2O_3@SiO_2)N@TiO_2 Functional Hybrid Nanoparticles with Actived Photocatalytic Ability. *J. Phys. Chem. C* **2009**, *113* (10), 4008–4011.

(90) Ibrahim, U.; Halim, A.; Zobir, M.; Zainal, Z. Photocatalytic Removal of 2,4,6-Trichlorophenol from Water Exploiting Commercial ZnO Powder. *DES* **2010**, *263* (1–3), 176–182.

(91) Nam, W.; Kim, J.; Han, G. Photocatalytic Oxidation of Methyl Orange in a Three-Phase Fluidized Bed Reactor. *Chemosphere* **2002**, *47*, 1019–1024.

(92) Guettaï, N.; Ait Amar, H. Photocatalytic Oxidation of Methyl Orange in Presence of Titanium Dioxide in Aqueous Suspension. Part I: Parametric Study. *Desalination* **2005**, *185* (1–3), 427–437.

(93) Mozia, S. Photocatalytic Membrane Reactors (PMRs) in Water and Wastewater Treatment . A Review. *Sep. Purif. Technol.* **2010**, *73* (2), 71–91.

(94) MURUGANANDHAM, M.; SWAMINATHAN, M. TiO_2–UV Photocatalytic Oxidation of Reactive Yellow 14: Effect of Operational Parameters. *J. Hazard. Mater.* **2006**, *135* (1–3), 78–86.

(95) Zhong, N.; Chen, M.; Luo, Y.; Wang, Z.; Xin, X.; Rittmann, B. E. A Novel Photocatalytic Optical Hollow-Fiber with High Photocatalytic Activity for Enhancement of 4-Chlorophenol Degradation. *Chem. Eng. J.* **2019**, *355* (August 2018), 731–739.

(96) Yang, J.; Chen, H.; Gao, J.; Yan, T.; Zhou, F.; Cui, S.; Bi, W. Synthesis of Fe_3O_4/g-C_3N_4 Nanocomposites and Their Application in the Photodegradation of 2,4,6-Trichlorophenol under Visible Light. *Mater. Lett.* **2016**, *164*, 183–189.

(97) Lin, J. C. Te; Sopajaree, K.; Jitjanesuwan, T.; Lu, M. C. Application of Visible Light on Copper-Doped Titanium Dioxide Catalyzing Degradation of Chlorophenols. *Sep. Purif. Technol.* **2018**, *191*, 233–243.

(98) Liu, L.; Chen, F.; Yang, F.; Chen, Y.; Crittenden, J. Photocatalytic Degradation of 2 , 4-Dichlorophenol Using Nanoscale Fe/TiO_2. *Chem. Eng. J.* **2012**, *181–182*, 189–195.

(99) Yang, J.; Cui, S.; Qiao, J. Q.; Lian, H. Z. The Photocatalytic

Dehalogenation of Chlorophenols and Bromophenols by Cobalt Doped Nano TiO$_2$. *J. Mol. Catal. A Chem.* **2014**, *395*, 42–51.

(100) Shen, Y. S.; Ku, Y.; Lee, K. C. The Effect of Light Absorbance on the Decomposition of Chlorophenols by Ultraviolet Radiation and u.v./H$_2$O$_2$ Processes. *Water Res.* **1995**, *29* (3), 907–914.

(101) Czaplicka, M. Photo-Degradation of Chlorophenols in the Aqueous Solution. *J. Hazard. Mater.* **2006**, *134* (1–3), 45–59.

(102) Hinojosa – Reyes, M.; Camposeco – Solis, R.; Ruiz, F.; Rodríguez – González, V.; Moctezuma, E. Promotional Effect of Metal Doping on Nanostructured TiO$_2$ during the Photocatalytic Degradation of 4-Chlorophenol and Naproxen Sodium as Pollutants. *Mater. Sci. Semicond. Process.* **2019**, *100* (May), 130–139.

(103) Long, G.; Ding, J.; Xie, L.; Sun, R.; Chen, M.; Zhou, Y.; Huang, X.; Han, G.; Li, Y.; Zhao, W. Fabrication of Mediator-Free g-C$_3$N$_4$/Bi$_2$WO$_6$ Z-Scheme with Enhanced Photocatalytic Reduction Dechlorination Performance of 2,4-DCP. *Appl. Surf. Sci.* **2018**, *455*, 1010–1018.

(104) Li, F.; Du, P.; Liu, W.; Li, X.; Ji, H.; Duan, J.; Zhao, D. Hydrothermal Synthesis of Graphene Grafted Titania/Titanate Nanosheets for Photocatalytic Degradation of 4-Chlorophenol: Solar-Light-Driven Photocatalytic Activity and Computational Chemistry Analysis. *Chem. Eng. J.* **2018**, *331*, 685–694.

(105) Xu, L.; Wang, J. Degradation of 2,4,6-Trichlorophenol Using Magnetic

Nanoscaled Fe_3O_4/CeO_2 Composite as a Heterogeneous Fenton-like Catalyst. *Sep. Purif. Technol.* **2015**, *149*, 255–264.

(106) Rengaraj, S.; Li, X. Z. Enhanced Photocatalytic Activity of TiO_2 by Doping with Ag for Degradation of 2,4,6-Trichlorophenol in Aqueous Suspension. *J. Mol. Catal. A Chem.* **2006**, *243* (1), 60–67.

(107) Sclafani, A.; Herrmann, J. M. Influence of Metallic Silver and of Platinum-Silver Bimetallic Deposits on the Photocatalytic Activity of Titania (Anatase and Rutile) in Organic and Aqueous Media. *J. Photochem. Photobiol. A Chem.* **1998**, *113* (2), 181–188.

(108) Vijayan, P.; Mahendiran, C.; Suresh, C.; Shanthi, K. Photocatalytic Activity of Iron Doped Nanocrystalline Titania for the Oxidative Degradation of 2,4,6-Trichlorophenol. *Catal. Today* **2009**, *141* (1–2), 220–224.

(109) Peng, H.; Cui, J.; Zhan, H.; Zhang, X. Improved Photodegradation and Detoxification of 2,4,6-Trichlorophenol by Lanthanum Doped Magnetic TiO_2. *Chem. Eng. J.* **2015**, *264*, 316–321.

(110) Sinirtas, E.; Isleyen, M.; Soylu, G. S. P. Photocatalytic Degradation of 2,4-Dichlorophenol with V_2O_5-TiO_2 Catalysts: Effect of Catalyst Support and Surfactant Additives. *Chinese J. Catal.* **2016**, *37* (4), 607–615.

(111) Li Fenfang, Dai Youzhi, Gong, Min, Yu Tieping, C. X. Synthesis, Characterization of Magnetic-Sepiolite Supported with TiO_2, and the

Photocatalytic Performance over Cr(VI) and 2,4-Dichlorophenol Co-Existed Wastewater. *J. Alloys Compd.* **2015**, *638*, 435–442.

(112) Li, K.; Zeng, Z.; Yan, L.; Huo, M.; Guo, Y.; Luo, S.; Luo, X. Fabrication of C/X-TiO$_2$@C$_3$N$_4$ NTs (X = N, F, Cl) Composites by Using Phenolic Organic Pollutants as Raw Materials and Their Visible-Light Photocatalytic Performance in Different Photocatalytic Systems. *Appl. Catal. B Environ.* **2016**, *187*, 269–280.

(113) Antonopoulou, M.; Vlastos, D.; Konstantinou, I. Photocatalytic Degradation of Pentachlorophenol by N-F-TiO$_2$: Identification of Intermediates, Mechanism Involved, Genotoxicity and Ecotoxicity Evaluation. *Photochem. Photobiol. Sci.* **2015**, *14* (3), 520–527.

(114) Ma, H. Y.; Zhao, L.; Guo, L. H.; Zhang, H.; Chen, F. J.; Yu, W. C. Roles of Reactive Oxygen Species (ROS) in the Photocatalytic Degradation of Pentachlorophenol and Its Main Toxic Intermediates by TiO$_2$/UV. *J. Hazard. Mater.* **2019**, *369*, 719–726.

(115) Ling, L.; Feng, Y.; Li, H.; Chen, Y.; Wen, J.; Zhu, J.; Bian, Z. Microwave Induced Surface Enhanced Pollutant Adsorption and Photocatalytic Degradation on Ag/TiO$_2$. *Appl. Surf. Sci.* **2019**, *483*, 772–778.

(116) Mangrulkar, P. A.; Kamble, S. P.; Joshi, M. M.; Meshram, J. S.; Labhsetwar, N. K.; Rayalu, S. S. Photocatalytic Degradation of Phenolics by N-Doped Mesoporous Titania under Solar Radiation. *Int.*

J. Photoenergy **2012**, *2012*, 1–10.

(117) Song, S.; Wang, C.; Hong, F.; He, Z.; Cai, Q.; Chen, J. Gallium- and Iodine-Co-Doped Titanium Dioxide for Photocatalytic Degradation of 2-Chlorophenol in Aqueous Solution: Role of Gallium. *Appl. Surf. Sci.* **2011**, *257* (8), 3427–3432.

(118) Sharotri, N.; Sud, D. A Greener Approach to Synthesize Visible Light Responsive Nanoporous S-Doped TiO_2 with Enhanced Photocatalytic Activity. *New J. Chem.* **2015**, *39*, 2217–2223.

(119) Sharma, A.; Lee, B. K. Rapid Photo-Degradation of 2-Chlorophenol under Visible Light Irradiation Using Cobalt Oxide-Loaded TiO_2/Reduced Graphene Oxide Nanocomposite from Aqueous Media. *J. Environ. Manage.* **2016**, *165*, 1–10.

(120) Lan, Z.; Yu, Y.; Yan, S.; Wang, E.; Yao, J.; Cao, Y. Synergetic Effect of N^{3-}, In^{3+} and Sn^{4+} Ions in TiO_2 towards Efficient Visible Photocatalysis. *J. Photochem. Photobiol. A Chem.* **2018**, *356*, 132–137.

(121) Bilgin Simsek, E. Solvothermal Synthesized Boron Doped TiO_2 Catalysts: Photocatalytic Degradation of Endocrine Disrupting Compounds and Pharmaceuticals under Visible Light Irradiation. *Appl. Catal. B Environ.* **2017**, *200*, 309–322.

(122) Chen, X.; Sun, H.; Zhang, J.; Ahmed Zelekew, O.; Lu, D.; Kuo, D. H.; Lin, J. Synthesis of Visible Light Responsive Iodine-Doped

Mesoporous TiO_2 by Using Biological Renewable Lignin as Template for Degradation of Toxic Organic Pollutants. *Appl. Catal. B Environ.* **2019**, *252*, 152–163.

(123) Al-Fahdi, T.; Al Marzouqi, F.; Kuvarega, A. T.; Mamba, B. B.; Al Kindy, S. M. Z.; Kim, Y.; Selvaraj, R. Visible Light Active CdS@TiO_2 Core-Shell Nanostructures for the Photodegradation of Chlorophenols. *J. Photochem. Photobiol. A Chem.* **2019**, *374*, 75–83.

(124) Choi, K. H.; Min, J.; Park, S. Y.; Park, B. J.; Jung, J. S. Enhanced Photocatalytic Degradation of Tri-Chlorophenol by Fe_3O_4@TiO_2@Au Photocatalyst under Visible-Light. *Ceram. Int.* **2019**, *45* (7), 9477–9482.

(125) Lu, Y. Y.; Zhang, Y. Y.; Zhang, J.; Shi, Y.; Li, Z.; Feng, Z. C.; Li, C. In Situ Loading of CuS Nanoflowers on Rutile TiO_2 Surface and Their Improved Photocatalytic Performance. *Appl. Surf. Sci.* **2016**, *370*, 312–319.

(126) Mahmiani, Y.; Sevim, A. M.; Gül, A. Photocatalytic Degradation of 4-Chlorophenol under Visible Light by Using TiO_2 Catalysts Impregnated with Co(II) and Zn(II) Phthalocyanine Derivatives. *J. Photochem. Photobiol. A Chem.* **2016**, *321*, 24–32.

(127) Zhao, X.; Wu, P.; Liu, M.; Lu, D.; Ming, J.; Li, C.; Ding, J.; Yan, Q.; Fang, P. Y_2O_3 Modified TiO_2 Nanosheets Enhanced the Photocatalytic Removal of 4-Chlorophenol and Cr (VI) in Sun Light.

Appl. Surf. Sci. **2017**, *410*, 134–144.

(128) Neubert, S.; Pulisova, P.; Wiktor, C.; Weide, P.; Mei, B.; Guschin, D. A.; Fischer, R. A.; Muhler, M.; Beranek, R. Enhanced Photocatalytic Degradation Rates at Rutile TiO_2 Photocatalysts Modified with Redox Co-Catalysts. *Catal. Today* **2014**, *230*, 97–103.

(129) Ozturk, B.; Soylu, G. S. P. Promoting Role of Transition Metal Oxide on $ZnTiO_3$-TiO_2 Nanocomposites for the Photocatalytic Activity under Solar Light Irradiation. *Ceram. Int.* **2016**, *42* (9), 11184–11192.

(130) Pozan, G. S.; Kambur, A. Significant Enhancement of Photocatalytic Activity over Bifunctional ZnO-TiO_2 Catalysts for 4-Chlorophenol Degradation. *Chemosphere* **2014**, *105*, 152–159.

(131) Shojaie, A.; Fattahi, M.; Jorfi, S.; Ghasemi, B. Hydrothermal Synthesis of Fe-TiO_2-Ag Nano-Sphere for Photocatalytic Degradation of 4-Chlorophenol (4-CP): Investigating the Effect of Hydrothermal Temperature and Time as Well as Calcination Temperature. *J. Environ. Chem. Eng.* **2017**, *5* (5), 456–4572.

(132) Martínez-Sánchez, C.; Montiel-González, F.; Díaz-Cervantes, E.; Rodríguez-González, V. Unraveling the Strength Interaction in a TiO_2-Graphene Photocatalytic Nanocomposite Synthesized by the Microwave Hydrothermal Method. *Mater. Sci. Semicond. Process.* **2019**, *101*, 262–271.

(133) Yu, J.; Wang, T.; Rtimi, S. Magnetically Separable TiO_2/FeOx/POM

Accelerating the Photocatalytic Removal of the Emerging Endocrine Disruptor: 2,4-Dichlorophenol. *Appl. Catal. B Environ.* **2019**, *254*, 66–75.

(134) Pino, E.; Encinas, M. V. Photocatalytic Degradation of Chlorophenols on TiO_2-325 mesh and TiO_2-P25. An Extended Kinetic Study of Photodegradation under Competitive Conditions. *J. Photochem. Photobiol. A Chem.* **2012**, *242*, 20–27.

(135) Shoneye, A.; Tang, J. Highly Dispersed FeOOH to Enhance Photocatalytic Activity of TiO_2 for Complete Mineralisation of Herbicides. *Appl. Surf. Sci.* **2020**, *511*, 145479.

(136) Ji, H.; Chang, F.; Hu, X.; Qin, W.; Shen, J. Photocatalytic Degradation of 2,4,6-Trichlorophenol over g-C_3N_4 under Visible Light Irradiation. *Chem. Eng. J.* **2013**, *218*, 183–190.

(137) Flohr J.K. Marta. X-Ray Powder Diffraction. *United States Geol. Surv.* **1997**, No. 1–2. Web accessed July **2017**. https://pubs.usgs.gov/info/diffraction/xrd.pdf

(138) Kaliva, M.; Vamvakaki, M. Nanomaterials Characterization. *Polymer Science and Nanotechnology*; *Elsevier*, **2020**; pp 401–433.

(139) Lewis, B. J.; Thompson, W. T.; Iglesias, F. C. Fission Product Chemistry in Oxide Fuels. *Elsevier Inc.*, **2012**; Vol. 2, 516–546. ISBN 978-0-08-056033-5.

(140) Benelmekki, M.; Erbe, A. Nanostructured Thin Films–Background, Preparation and Relation to the Technological Revolution of the 21st Century. *Elsevier Ltd.,* **2019**; Vol. 14, 1–34. ISBN 978-0-08-102572-7.

(141) Valeev, R. G.; Vakhrushev, A. V.; Fedotov, A. Y.; Petukhov, D. I. Nanostructured Semiconductors in Porous Alumina Matrices: Modeling, Synthesis, and Properties. *Apple Academic Press Inc.*: USA, **2019**. ISBN 978-0-42-967523-2.

(142) Gardiner, D. J.; Graves, P. R. Practical Raman Spectroscopy. *Springer-Verlag*: USA, **1989**. ISBN 978-0-387-50254-0.

(143) Bhagyaraj, S.; Oluwafemi, O. S.; Krupa, I. Polymers in Optics. *Polymer Science and Innovative Applications*; *Elsevier Inc.*, **2020**, 423–455. ISBN 978-0-12-816808-0.

(144) Abraham, J.; Jose, B.; Jose, A.; Thomas, S. Characterization of Green Nanoparticles from Plants. *Phytonanotechnology*; *Elsevier Inc.*, **2020**, 21–39. ISBN 978-0-12-822348-2.

(145) Gregg, S. J.; Sing, K. S. W. Adsorption, Surface Area and Porosity. *Academic Press Inc.*: London, **1982**, 2nd edition, 1–303. ISBN 978-0-12-300956-2.

(146) Lowell, S.; Shields, J. E.; Thomas, M. A.; Thommes, M. Characterization of Porous Solids and Powders: Surface Area, Pore Size and Density; Particle Technology Series; *Springer,* Netherlands: Dordrecht, **2004**; Vol. 16. ISBN 978-9-04-816633-6.

(147) Swapp, S. "Scanning Electron Microscopy (SEM)." *The Science Education Resource Center*, Carleton, USA. Web accessed July **2017**. https://serc.carleton.edu/18401.

(148) Goldstein, J. I.; Newbury, D. E.; Echlin, P.; Joy, D. C.; Lyman, C. E.; Lifshin, E.; Sawyer, L.; Michael, J. R. Scanning Electron Microscopy and X-Ray Microanalysis. *Springer* US: Boston, MA, **2003**.

(149) Martin, D. J. Investigation into High Efficiency Visible Light Photocatalysts for Water Reduction and Oxidation. *Springer Theses*; *Springer International Publishing*: Cham, **2015**.

(150) Pavia, D. L.; Lampman, G. M.; Kriz, G. S. Introduction to Spectroscopy. *Thomson Learning Inc.*: USA, **2001**; pp 1–680. ISBN 0-03-031961-7.

(151) Gesesse, G. D.; Gomis-Berenguer, A.; Barthe, M. F.; Ania, C. O. On the Analysis of Diffuse Reflectance Measurements to Estimate the Optical Properties of Amorphous Porous Carbons and Semiconductor/Carbon Catalysts. *J. Photochem. Photobiol. A Chem.* **2020**, *398*, 112622.

(152) Shimadzu, "TOC-L Series - Features." Web accessed July **2017**. https://www.shimadzu.com/an/products/total-organic-carbon-analysis/toc-analysis/toc-l-series/features.html.

(153) Senesi, N.; Senesi, G. S. ELECTRON-SPIN RESONANCE SPECTROSCOPY. *Encyclopedia of Soils in the Environment*;
230

Elsevier Ltd, **2005**; Vol. 3, pp 426–437.

(154) Rhodes, C. J. Unpaired Electrons as Probes of Catalytic Systems. *Sci. Prog.* **2014**, *97* (4), 303–370.

(155) Fu, F.; Shen, H.; Sun, X.; Xue, W.; Shoneye, A.; Ma, J.; Luo, L.; Wang, D.; Wang, J.; Tang, J. Synergistic Effect of Surface Oxygen Vacancies and Interfacial Charge Transfer on Fe(III)/Bi_2MoO_6 for Efficient Photocatalysis. *Appl. Catal. B Environ.* **2019**, *247*, 150–162.

(156) Djikanović, D.; Kalauzi, A.; Jeremić, M.; Mićić, M.; Radotić, K. Deconvolution of Fluorescence Spectra: Contribution to the Structural Analysis of Complex Molecules. *Colloids Surfaces B Biointerfaces* **2007**, *54* (2), 188–192.

(157) Karoui, R.; Blecker, C. Fluorescence Spectroscopy Measurement for Quality Assessment of Food Systems-a Review. *Food Bioprocess Technol.* **2011**, *4* (3), 364–386.

(158) Xiang, Q.; Yu, J.; Wong, P. K. Quantitative Characterization of Hydroxyl Radicals Produced by Various Photocatalysts. *J. Colloid Interface Sci.* **2011**, *357* (1), 163–167.

(159) Ishibashi, K. I.; Fujishima, A.; Watanabe, T.; Hashimoto, K. Detection of Active Oxidative Species in TiO_2 Photocatalysis Using the Fluorescence Technique. *Electrochem. commun.* **2000**, *2* (3), 207–210.

(160) Skoog, D. A.; West, D. M.; Holler, F. J.; Crouch, S. R. Analytical

Chemistry 7th (Seventh) Edition. *Brooks/Cole Publishing Company*: USA, **1999**. ISBN B004TLTOVW.

(161) Scholtzova, A. The Scale up and Modelling of High Performance Liquid Chromatography. PhD Thesis, *University College London*, United Kingdom. **2000**.

(162) Banerjee, S.; Mazumdar, S. Electrospray Ionization Mass Spectrometry: A Technique to Access the Information beyond the Molecular Weight of the Analyte. *Int. J. Anal. Chem.* **2012**, *2012*, 1–40.

(163) Anandhi, A.; Palraj, S.; Subramanian, G.; Selvaraj, M. Corrosion Resistance and Improved Adhesion Properties of Propargyl Alcohol Impregnated Mesoporous Titanium Dioxide Built-in Epoxy Zinc Rich Primer. *Prog. Org. Coatings.* **2016**, *97*, 10–18.

(164) Wang, Y.; Yang, W.; Chen, X.; Wang, J.; Zhu, Y. Photocatalytic Activity Enhancement of Core-Shell Structure $g\text{-}C_3N_4@TiO_2$ via Controlled Ultrathin $g\text{-}C_3N_4$ Layer. *Appl. Catal. B Environ.* **2017**, *220*, 337–347.

(165) Yamashita, T.; Hayes, P. Analysis of XPS Spectra of Fe^{2+} and Fe^{3+} Ions in Oxide Materials. *Appl. Surf. Sci.* **2008**, *254* (8), 2441–2449.

(166) Baltrusaitis, J.; Jayaweera, P. M.; Grassian, V. H. XPS Study of Nitrogen Dioxide Adsorption on Metal Oxide Particle Surfaces under Different Environmental Conditions. *Phys. Chem. Chem. Phys.* **2009**, *11* (37), 8295–8305.

(167) Huang, H.; Lin, J.; Zhu, G.; Weng, Y.; Wang, X.; Fu, X.; Long, J. A Long-Lived Mononuclear Cyclopentadienyl Ruthenium Complex Grafted onto Anatase TiO_2 for Efficient CO_2 Photoreduction. *Angew. Chemie - Int. Ed.* **2016**, *55* (29), 8314–8318.

(168) Adán, C.; Bahamonde, A.; Fernández-García, M.; Martínez-Arias, A. Structure and Activity of Nanosized Iron-Doped Anatase TiO_2 catalysts for Phenol Photocatalytic Degradation. *Appl. Catal. B Environ.* **2007**, *72* (1–2), 11–17.

(169) Shimura, K.; Kawai, H.; Yoshida, T.; Yoshida, H. Bifunctional Rhodium Cocatalysts for Photocatalytic Steam Reforming of Methane over Alkaline Titanate. *ACS Catal.* **2012**, *2* (10), 2126–2134.

(170) Lan, L.; Shao, Y.; Jiao, Y.; Zhang, R.; Hardacre, C.; Fan, X. Chinese Journal of Chemical Engineering Systematic Study of H_2 Production from Catalytic Photoreforming of Cellulose over Pt Catalysts Supported on TiO_2. *Chinese J. Chem. Eng.* **2020**, *28* (8), 2084–2091.

(171) Rao, G.; Zhao, H.; Chen, J.; Deng, W.; Jung, B.; Abdel-wahab, A.; Batchelor, B.; Li, Y. FeOOH and Fe_2O_3 Co-Grafted TiO_2 Photocatalysts for Bisphenol A Degradation in Water. *Catal. Commun.* **2017**, *97*, 125–129.

(172) Anandan, S.; Vinu, A.; Mori, T.; Gokulakrishnan, N.; Srinivasu, P.; Murugesan, V.; Ariga, K. Photocatalytic Degradation of 2,4,6-Trichlorophenol Using Lanthanum Doped ZnO in Aqueous

Suspension. *Catal. Commun.* **2007**, *8* (9), 1377–1382.

(173) S, S.; Nagashree, K. L.; Maiyalagan, T.; Keerthiga, G. Photocatalytic Degradation of 2,4-Dichlorophenoxyacetic Acid - A Comparative Study in Hydrothermal TiO_2 and Commercial TiO_2. *Appl. Surf. Sci.* **2018**.

(174) Liu, S.; Zhu, J.; Guo, X.; Ge, J.; Wu, H. Preparation of α-Fe_2O_3-TiO_2/Fly Ash Cenospheres Photocatalyst and Its Mechanism of Photocatalytic Degradation. *Colloids Surfaces A Physicochem. Eng. Asp.* **2015**, *484*, 434–440.

(175) Geng, B.; Tao, B.; Li, X.; Wei, W. Ni^{2+}/Surfactant-Assisted Route to Porous α-Fe_2O_3 Nanoarchitectures. *Nanoscale.* **2012**, *4* (5), 1671.

(176) Lu, M. N.; Das, R. P.; Li, W.; Peng, J. H.; Zhang, L. B. Microwave Mediated Precipitation and Aging of Iron Oxyhydroxides at Low Temperature for Possible Hydrometallurgical Applications. *Hydrometallurgy.* **2013**, *134–135*, 110–116.

(177) Kulyukhin, S. A.; Kamenskaya, A. N. Mechanism of Decomposition of $UO_2(NO_3)$ $2 \cdot 6H_2O$ + $Fe(NO_3)_3 \cdot$ $9H_2O$ Mixture under the Action of Microwave Radiation. *Radiochemistry.* **2012**, *54* (5), 465–472.

(178) de Faria, D. L. A.; Venâncio Silva, S.; de Oliveira, M. T. Raman Microspectroscopy of Some Iron Oxides and Oxyhydroxides. *J. Raman Spectrosc.* **1997**, *28* (11), 873–878.

(179) Kong, L.; Wang, C.; Wan, F.; Zheng, H.; Zhang, X. Synergistic Effect

of Surface Self-Doping and Fe Species-Grafting for Enhanced Photocatalytic Activity of TiO_2 under Visible-Light. *Appl. Surf. Sci.* **2017**, *396*, 26–35.

(180) Lee, S. C.; Lintang, H. O.; Yuliati, L. High Photocatalytic Activity of Fe_2O_3/TiO_2 Nanocomposites Prepared by Photodeposition for Degradation of 2,4-Dichlorophenoxyacetic Acid. *Beilstein J. Nanotechnol.* **2017**, *8*, 915–926.

(181) Cong, Y.; Zhang, J.; Chen, F.; Anpo, M. Synthesis and Characterization of Nitrogen-Doped TiO_2 Nanophotocatalyst with High Visible Light Activity. *J. Phys. Chem. C* **2007**, *111* (19), 6976–6982.

(182) Liu, H.; Shon, H. K.; Sun, X.; Vigneswaran, S.; Nan, H. Preparation and Characterization of Visible Light Responsive Fe_2O_3-TiO_2 Composites. *Appl. Surf. Sci.* **2011**, *257* (13), 5813–5819.

(183) Zhao, W.; Zhang, J.; Zhu, X.; Zhang, M.; Tang, J.; Tan, M.; Wang, Y. Enhanced Nitrogen Photofixation on Fe-Doped TiO_2 with Highly Exposed (101) Facets in the Presence of Ethanol as Scavenger. *Appl. Catal. B Environ.* **2014**, *144*, 468–477.

(184) Lente, G.; Espenson, J. H. Photoreduction of 2,6-Dichloroquinone in Aqueous Solution: Use of a Diode Array Spectrophotometer Concurrently to Drive and Detect a Photochemical Reaction. *J. Photochem. Photobiol. A Chem.* **2004**, *163* (1–2), 249–258.

(185) Sorokin, A.; De Suzzoni-Dezard, S.; Poullain, D.; Noël, J. P.; Meunier,

B. CO_2 as the Ultimate Degradation Product in the H_2O_2 Oxidation of 2,4,6-Trichlorophenol Catalyzed by Iron Tetrasulfophthalocyanine. *J. Am. Chem. Soc.* **1996**, *118* (31), 7410–7411.

(186) Sen Gupta, S.; Stadler, M.; Noser, C. A.; Ghosh, A.; Steinhoff, B.; Lenoir, D.; Horwitz, C. P.; Schramm, K. W.; Collins, T. J. Rapid Total Destruction of Chlorophenol Priority Pollutants by Activated Hydrogen Peroxide. *Science (80-.).* **2002**, *296*, 326–328.

(187) Pino-Chamorro, J. Á.; Ditrói, T.; Lente, G.; Fábián, I. A Detailed Kinetic Study of the Direct Photooxidation of 2,4,6-Trichlorophenol. *J. Photochem. Photobiol. A Chem.* **2016**, *330*, 71–78.

(188) Neubert, S.; Mitoraj, D.; Shevlin, S. A.; Pulisova, P.; Heimann, M.; Du, Y.; Goh, G. K. L.; Pacia, M.; Kruczała, K.; Turner, S.; et al. Highly Efficient Rutile TiO 2 Photocatalysts with Single Cu(ii) and Fe(iii) Surface Catalytic Sites. *J. Mater. Chem. A* **2016**, *4* (8), 3127–3138.

(189) Yuliati, L.; Roslan, N. A.; Siah, W. R.; Lintang, H. O. Cobalt Oxide-Modified Titanium Dioxide Nanoparticle Photocatalyst for Degradation of 2,4-Dichlorophenoxyacetic Acid. *Indones. J. Chem.* **2017**, *17* (2), 284–290.

(190) Wu, J.; Li, C.; Zhao, X.; Wu, Q.; Qi, X.; Chen, X.; Hu, T.; Cao, Y. Photocatalytic Oxidation of Gas-Phase Hg0 by CuO/TiO$_2$. *Appl. Catal. B Environ.* **2015**, *176–177* (October), 559–569.

(191) Moniz, S. J. A.; Tang, J. Charge Transfer and Photocatalytic Activity

in CuO/TiO$_2$ Nanoparticle Heterojunctions Synthesised through a Rapid, One-Pot, Microwave Solvothermal Route. *ChemCatChem* **2015**, *7* (11), 1659–1667.

(192) Zhou, G.; Dong, Y.; He, D. Bimetallic Ru–M/TiO$_2$ (M = Fe, Ni, Cu, Co) Nanocomposite Catalysts Facribated by Galvanic Replacement: Structural Elucidation and Catalytic Behavior in Benzene Selective Hydrogenation. *Appl. Surf. Sci.* **2018**, *456*, 1004–1013.

(193) An, X.; Liu, H.; Qu, J.; Moniz, S. J. A.; Tang, J. Photocatalytic Mineralisation of Herbicide 2,4,5-Trichlorophenoxyacetic Acid: Enhanced Performance by Triple Junction Cu-TiO$_2$-Cu$_2$O and the Underlying Reaction Mechanism. *New J. Chem.* **2015**, *39* (1), 314–320.

(194) Qiu, X.; Miyauchi, M.; Sunada, K.; Minoshima, M.; Liu, M.; Lu, Y.; Li, D.; Yoshiki Shimodaira; Hosogi, Y.; Kuroda, Y.; et al. Hybrid Cu$_x$O/ TiO$_2$ Nanocomposites As Risk-Reduction Materials in Indoor. *ACS Nano* **2012**, *6* (2), 1609–1618.

(195) Zhu, L.; Zeng, Y.; Zhang, S.; Deng, J.; Zhong, Q. Effects of Synthesis Methods on Catalytic Activities of CoOx–TiO$_2$ for Low-Temperature NH$_3$-SCR of NO. *J. Environ. Sci. (China)* **2017**, *54*, 277–287.

(196) Petitto, S. C.; Langell, M. A. Surface Composition and Structure of Co$_3$O$_4$(110) and the Effect of Impurity Segregation. *J. Vac. Sci. Technol. A Vacuum, Surfaces, Film.* **2004**, *22* (4), 1690–1696.

(197) Shen, Z.-X.; Allen, J. W.; Lindberg, P. A. P.; Dessau, D. S.; Wells, B. O.; Borg, A.; Ellis, W.; Kang, J. S.; Oh, S.-J.; Lindau, I.; et al. Photoemission Study of CoO. *Phys. Rev. B* **1990**, *42* (3), 1817–1828.

(198) Xie, J.; Jin, R.; Li, A.; Bi, Y.; Ruan, Q.; Deng, Y.; Zhang, Y.; Yao, S.; Sankar, G.; Ma, D.; et al. Highly Selective Oxidation of Methane to Methanol at Ambient Conditions by Titanium Dioxide-Supported Iron Species. *Nat. Catal.* **2018**, *1* (11), 889–896.

(199) McIntyre, N. S.; Zetaruk, D. G. X-Ray Photoelectron Spectroscopic Studies of Iron Oxides. *Anal. Chem.* **1977**, *49* (11), 1521–1529.

(200) Mylonas, A.; Papaconstantinou, E. Photocatalytic Degradation of Chlorophenols to CO_2 and HCl with Polyoxotungstates in Aqueous Solution. *J. Mol. Catal.* **1994**, *92* (3), 261–267.

(201) Burrows, H. D.; Ernestova, L. S.; Kemp, T. J.; Skurlatov, Y. I.; Purmal, A. P.; Yermakov, A. N. Kinetics and Mechanism of Photodegradation of Chlorophenols. *Prog. React. Kinet. Mech.* **1998**, *23* (3), 145–207.

(202) Shoneye, A.; Tang, J. Highly Dispersed FeOOH to Enhance Photocatalytic Activity of TiO_2 for Complete Mineralisation of Herbicides. *Appl. Surf. Sci.* **2020**, *511*, 145479.

(203) Kim, T. W.; Choi, K.-S. Nanoporous $BiVO_4$ Photoanodes with Dual-Layer Oxygen Evolution Catalysts for Solar Water Splitting. *Science (80-.).* **2014**, *343* (6174), 990–994.

(204) Oehler, F.; Naumann, R.; Köferstein, R.; Hesse, D.; Ebbinghaus, S. G.

Photocatalytic Activity of $CaTaO_2N$ Nanocrystals Obtained from a Hydrothermally Synthesized Oxide Precursor. *Mater. Res. Bull.* **2016**, *73*, 276–283.

(205) Oehler, F.; Ebbinghaus, S. G. Photocatalytic Properties of CoOx-Loaded Nano-Crystalline Perovskite Oxynitrides ABO_2N (A = Ca, Sr, Ba, La; B = Nb, Ta). *Solid State Sci.* **2016**, *54*, 43–48.

(206) Zhang, F.; Yamakata, A.; Maeda, K.; Moriya, Y.; Takata, T.; Kubota, J.; Teshima, K.; Oishi, S.; Domen, K. Cobalt-Modified Porous Single-Crystalline $LaTiO_2N$ for Highly Efficient Water Oxidation under Visible Light. *J. Am. Chem. Soc.* **2012**, *134* (20), 8348–8351.

(207) Barroso, M.; Cowan, A. J.; Pendlebury, S. R.; Grätzel, M.; Klug, D. R.; Durrant, J. R. The Role of Cobalt Phosphate in Enhancing the Photocatalytic Activity of $α$-Fe_2O_3 toward Water Oxidation. *J. Am. Chem. Soc.* **2011**, *133* (38), 14868–14871.

(208) Kamata, K.; Maeda, K.; Lu, D.; Kako, Y.; Domen, K. Synthesis and Photocatalytic Activity of Gallium-Zinc-Indium Mixed Oxynitride for Hydrogen and Oxygen Evolution under Visible Light. *Chem. Phys. Lett.* **2009**, *470* (1–3), 90–94.

(209) Guerrero-Araque, D.; Acevedo-Peña, P.; Ramírez-Ortega, D.; Lartundo-Rojas, L.; Gómez, R. SnO_2–TiO_2 Structures and the Effect of CuO, CoO Metal Oxide on Photocatalytic Hydrogen Production. *J. Chem. Technol. Biotechnol.* **2017**, *92* (7), 1531–1539.

(210) Pandiyan, T.; Martínez Rivas, O.; Orozco Martínez, J.; Burillo Amezcua, G.; Martínez-Carrillo, M. A. Comparison of Methods for the Photochemical Degradation of Chlorophenols. *J. Photochem. Photobiol. A Chem.* **2002**, *146* (3), 149–155.

(211) Ma, Y.; Zhang, Y.; Zhu, X.; Lu, N.; Li, C.; Yuan, X.; Qu, J. Photocatalytic Degradation and Rate Constant Prediction of Chlorophenols and Bisphenols by $H_3PW_{12}O_{40}$/GR/TiO_2 Composite Membrane. *Environ. Res.* **2020**, *188*, 109786.

(212) Zhen, Y.; Zhang, Q.; Zhang, X.; Zhang, G.; Chen, X.; Zhao, C. A Novel Tubular Up-Flow Magnetic Film Photocatalytic System Optimized by Main Factors Control for Efficient Removal of Chlorophenols Wastewater. *J. Hazard. Mater.* **2020**, *398*.

(213) Antonaraki, S.; Androulaki, E.; Dimotikali, D.; Hiskia, A.; Papaconstantinou, E. Photolytic Degradation of All Chlorophenols with Polyoxometallates and H_2O_2. *J. Photochem. Photobiol. A Chem.* **2002**, *148* (1–3), 191–197.

(214) Kochany, J.; Bolton, J. R. Mechanism of Photodegradation of Aqueous Organic Pollutants. 1. EPR Spin-Trapping Technique for the Determination of •OH Radical Rate Constants in the Photooxidation of Chlorophenols Following the Photolysis of H_2O_2. *J. Phys. Chem.* **1991**, *95* (13), 5116–5120.

(215) Goldstein, S.; Czapski, G.; Rabani, J. Oxidation of Phenol by

Radiolytically Generated .Bul.OH and Chemically Generated SO$_4$.Bul.-. A Distinction between .Bul.OH Transfer and Hole Oxidation in the Photolysis of TiO$_2$ Colloid Solution. *J. Phys. Chem.* **1994**, *98* (26), 6586–6591.

(216) Utami, F. D.; Rahman, D. Y.; Sustini, E.; Abdullah, M. Immobilization of TiO$_2$ on Transparent Plastic and Its Application in Photocatalytic Wastewater Treatment. *J. Phys. Conf. Ser.* **2019**, (1), *1171.*

(217) Nakata, K.; Fujishima, A. TiO$_2$ Photocatalysis: Design and Applications. *J. Photochem. Photobiol. C Photochem. Rev.* **2012**, *13* (3), 169–189.

(218) Stylidi, M.; Kondarides, D. I.; Verykios, X. E. Pathways of Solar Light-Induced Photocatalytic Degradation of Azo Dyes in Aqueous TiO$_2$ Suspensions. *Appl. Catal. B Environ.* **2003**, *40* (4), 271–286.

(219) Loeb, S. K.; Alvarez, P. J. J.; Brame, J. A.; Cates, E. L.; Choi, W.; Crittenden, J.; Dionysiou, D. D.; Li, Q.; Li-Puma, G.; Quan, X.; et al. The Technology Horizon for Photocatalytic Water Treatment: Sunrise or Sunset? *Environ. Sci. Technol.* **2019**, *53* (6), 2937–2947.

(220) Benotti, M. J.; Stanford, B. D.; Wert, E. C.; Snyder, S. A. Evaluation of a Photocatalytic Reactor Membrane Pilot System for the Removal of Pharmaceuticals and Endocrine Disrupting Compounds from Water. *Water Res.* **2009**, *43* (6), 1513–1522.

(221) Behnajady, M. A.; Modirshahla, N.; Mirzamohammady, M.; Vahid, B.;

Behnajady, B. Increasing Photoactivity of Titanium Dioxide Immobilized on Glass Plate with Optimization of Heat Attachment Method Parameters. *J. Hazard. Mater.* **2008**, *160* (2), 508–513.

(222) Islam, T.; Dominguez, A.; Turley, R. S.; Kim, H.; Sultana, K. A.; Shuvo, M. A. I.; Alvarado-tenorio, B.; Montes, M. O.; Lin, Y.; Gardea-torresdey, J.; et al. Development of Photocatalytic Paint Based on TiO_2 and Photopolymer Resin for the Degradation of Organic Pollutants in Water. *Sci. Total Environ.* **2020**, *704*, 135406.

(223) Ounas, O.; El Foulani, A. A.; Lekhlif, B.; Jamal-Eddine, J. Immobilization of TiO_2 into a Poly Methyl Methacrylate (PMMA) as Hybrid Film for Photocatalytic Degradation of Methylene Blue. *Mater. Today Proc.* **2019**, *22*, 35–40.

(224) Dong, C.; Ni, X. The Photopolymerization and Characterization of Methyl Methacrylate Initiated by Nanosized Titanium Dioxide. *J. Macromol. Sci. - Pure Appl. Chem.* **2004**, *41 A* (5), 547–563.

(225) Wang, Y.; Huang, Z.; Gurney, R. S.; Liu, D. Superhydrophobic and Photocatalytic PDMS/TiO2 Coatings with Environmental Stability and Multifunctionality. *Colloids Surfaces A Physicochem. Eng. Asp.* **2019**, *561*, 101–108.

(226) Liu, X.; Chen, Q.; Lv, L.; Feng, X.; Meng, X. Preparation of Transparent PVA/TiO_2 Nanocomposite Films with Enhanced Visible-Light Photocatalytic Activity. *Catal. Commun.* **2015**, *58*, 30–33.

(227) Yasin, S. A.; Abbas, J. A.; Ali, M. M.; Saeed, I. A.; Ahmed, I. H. Methylene Blue Photocatalytic Degradation by TiO_2 Nanoparticles Supported on PET Nanofibres. *Mater. Today Proc.* **2020**, *20*, 482–487.

(228) Tran, M. L.; Fu, C. C.; Chiang, L. Y.; Hsieh, C. Te; Liu, S. H.; Juang, R. S. Immobilization of TiO_2 and TiO_2-GO Hybrids onto the Surface of Acrylic Acid-Grafted Polymeric Membranes for Pollutant Removal: Analysis of Photocatalytic Activity. *J. Environ. Chem. Eng.* **2020**, *8* (5), 104422.

(229) Bonnefond, A.; González, E.; Asua, J.; Leiza, J.; Ieva, E.; Brinati, G.; Carella, S.; Marrani, A.; Veneroni, A.; Kiwi, J.; et al. Stable Photocatalytic Paints Prepared from Hybrid Core-Shell Fluorinated/Acrylic/TiO_2 Waterborne Dispersions. *Crystals* **2016**, *6* (10), 136.

(230) Guo, M.-Z.; Maury-Ramirez, A.; Poon, C. S. Self-Cleaning Ability of Titanium Dioxide Clear Paint Coated Architectural Mortar and Its Potential in Field Application. *J. Clean. Prod.* **2016**, *112*, 3583–3588.

(231) Enea, D.; Bellardita, M.; Scalisi, P.; Alaimo, G.; Palmisano, L. Effects of Weathering on the Performance of Self-Cleaning Photocatalytic Paints. *Cem. Concr. Compos.* **2019**, *96*, 77–86.

(232) Delnavaz, M.; Ayati, B.; Ganjidoust, H.; Sanjabi, S. Application of Concrete Surfaces as Novel Substrate for Immobilization of TiO_2 Nano Powder in Photocatalytic Treatment of Phenolic Water. *J.*

Environ. Heal. Sci. Eng. **2015**, *13* (1), 58.

(233) Feng, S.; Liu, F.; Fu, X.; Peng, X.; Zhu, J.; Zeng, Q.; Song, J. Photocatalytic Performances and Durability of TiO_2/Cement Composites Prepared by a Smear Method for Organic Wastewater Degradation. *Ceram. Int.* **2019**, *45* (17, Part B), 23061–23069.

(234) Feng, S.; Song, J.; Liu, F.; Fu, X.; Guo, H.; Zhu, J.; Zeng, Q.; Peng, X.; Wang, X.; Ouyang, Y.; et al. Photocatalytic Properties, Mechanical Strength and Durability of TiO_2/Cement Composites Prepared by a Spraying Method for Removal of Organic Pollutants. *Chemosphere* **2020**, *254*, 126813.

(235) Wang, D.; Hou, P.; Zhang, L.; Xie, N.; Yang, P.; Cheng, X. Photocatalytic Activities and Chemically-Bonded Mechanism of SiO_2@TiO_2 Nanocomposites Coated Cement-Based Materials. *Mater. Res. Bull.* **2018**, *102*, 262–268.

(236) Mendoza, C.; Valle, A.; Castellote, M.; Bahamonde, A.; Faraldos, M. TiO_2 and TiO_2–SiO_2 Coated Cement: Comparison of Mechanic and Photocatalytic Properties. *Appl. Catal. B Environ.* **2015**, *178*, 155–164.

(237) Yang, J.; Wang, G.; Wang, D.; Liu, C.; Zhang, Z. A Self-Cleaning Coating Material of TiO_2 Porous Microspheres/Cement Composite with High-Efficient Photocatalytic Depollution Performance. *Mater. Lett.* **2017**, *200*, 1–5.

(238) Zou, Q.; Li, H.; Yang, Y.; Miao, Y.; Huo, Y. Bi_2O_3/TiO_2 Photocatalytic

Film Coated on Floated Glass Balls for Efficient Removal of Organic Pollutant. *Appl. Surf. Sci.* **2019**, *467–468*, 354–360.

(239) Łęcki, T.; Zarębska, K.; Sobczak, K.; Skompska, M. Photocatalytic Degradation of 4-Chlorophenol with the Use of $FTO/TiO_2/SrTiO_3$ Composite Prepared by Microwave-Assisted Hydrothermal Method. *Appl. Surf. Sci.* **2019**, *470*, 991–1002.

(240) Zeng, J.; Liu, S.; Cai, J.; Zhang, L. TiO_2 Immobilized in Cellulose Matrix for Photocatalytic Degradation of Phenol under Weak UV Light Irradiation. *J. Phys. Chem. C* **2010**, *114* (17), 7806–7811.

(241) Lin, Z.; Huang, J. A Hierarchical $H_3PW_{12}O_{40}/TiO_2$ Nanocomposite with Cellulose as Scaffold for Photocatalytic Degradation of Organic Pollutants. *Sep. Purif. Technol.* **2021**, *264*, 118427.

(242) Yu, Y.; Zhu, X.; Wang, L.; Wu, F.; Liu, S.; Chang, C.; Luo, X. A Simple Strategy to Design 3-Layered $Au-TiO_2$ Dual Nanoparticles Immobilized Cellulose Membranes with Enhanced Photocatalytic Activity. *Carbohydr. Polym.* **2020**, *231*, 115694.

(243) Wu, H.; Inaba, T.; Wang, Z.-M.; Endo, T. Photocatalytic TiO_2@CS-Embedded Cellulose Nanofiber Mixed Matrix Membrane. *Appl. Catal. B Environ.* **2020**, *276*, 119111.

(244) Sharma, D.; Kumari, M.; Dhayal, V. Fabrication and Characterization of Cellulose/PVA/TiO_2 Nanocomposite Thin Film as a Photocatalyst. *Mater. Today Proc.* **2021**.

(245) Petrisková, P.; Monfort, O.; Satrapinskyy, L.; Dobročka, E.; Plecenik, T.; Plesch, G.; Papšík, R.; Bermejo, R.; Lenčéš, Z. Preparation and Photocatalytic Activity of TiO_2 Nanotube Arrays Prepared on Transparent Spinel Substrate. *Ceram. Int.* **2021**, *47* (9), 12970–12980.

(246) Magnone, E.; Kim, M. K.; Lee, H. J.; Park, J. H. Facile Synthesis of TiO_2-Supported Al_2O_3 Ceramic Hollow Fiber Substrates with Extremely High Photocatalytic Activity and Reusability. *Ceram. Int.* **2021**, *47* (6), 7764–7775.

(247) Venkata Subba Rao, K.; Rachel, A.; Subrahmanyam, M.; Boule, P. Immobilization of TiO_2 on Pumice Stone for the Photocatalytic Degradation of Dyes and Dye Industry Pollutants. *Appl. Catal. B Environ.* **2003**, *46* (1), 77–85.

(248) Shao, L.; Liu, H.; Zeng, W.; Zhou, C.; Li, D.; Wang, L.; Lan, Y.; Xu, F.; Liu, G. Immobilized and Photocatalytic Performances of PDMS-SiO_2-Chitosan@TiO_2 Composites on Pumice under Simulated Sunlight Irradiation. *Appl. Surf. Sci.* **2019**, *478*, 1017–1026.

(249) Li, D.; Zheng, H.; Wang, Q.; Wang, X.; Jiang, W.; Zhang, Z.; Yang, Y. A Novel Double-Cylindrical-Shell Photoreactor Immobilized with Monolayer TiO_2-Coated Silica Gel Beads for Photocatalytic Degradation of Rhodamine B and Methyl Orange in Aqueous Solution. *Sep. Purif. Technol.* **2014**, *123*, 130–138.

(250) Brossault, D. F. F.; McCoy, T. M.; Routh, A. F. Self-Assembly of

TiO$_2$/Fe$_3$O$_4$/SiO$_2$ Microbeads: A Green Approach to Produce Magnetic Photocatalysts. *J. Colloid Interface Sci.* **2021**, *584*, 779–788.

(251) Belessi, V.; Lambropoulou, D.; Konstantinou, I.; Katsoulidis, A.; Pomonis, P.; Petridis, D.; Albanis, T. Structure and Photocatalytic Performance of TiO$_2$/Clay Nanocomposites for the Degradation of Dimethachlor. *Appl. Catal. B Environ.* **2007**, *73* (3), 292–299.

(252) Zhou, P.; Shen, Y.; Zhao, S.; Li, G.; Cui, B.; Wei, D.; Shen, Y. Synthesis of Clinoptilolite-Supported BiOCl/TiO$_2$ Heterojunction Nanocomposites with Highly-Enhanced Photocatalytic Activity for the Complete Degradation of Xanthates under Visible Light. *Chem. Eng. J.* **2021**, *407*, 126697.

(253) Mehrabadi, Z.; Faghihian, H. Clinoptilolite Modified with TiO$_2$ for Simultaneous Elimination of Two Herbicides; 2,4-D and MCPA by UV and Sunlight-Assisted Photocatalytic Degradation. *Mater. Res. Bull.* **2019**, *119*, 110569.

(254) Wu, A.; Wang, D.; Wei, C.; Zhang, X.; Liu, Z.; Feng, P.; Ou, X.; Qiang, Y.; Garcia, H.; Niu, J. A Comparative Photocatalytic Study of TiO$_2$ Loaded on Three Natural Clays with Different Morphologies. *Appl. Clay Sci.* **2019**, *183*, 105352.

(255) Alfred, M. O.; Omorogie, M. O.; Bodede, O.; Moodley, R.; Ogunlaja, A.; Adeyemi, O. G.; Günter, C.; Taubert, A.; Iermak, I.; Eckert, H.; et al. Solar-Active Clay-TiO$_2$ Nanocomposites Prepared via Biomass

Assisted Synthesis: Efficient Removal of Ampicillin, Sulfamethoxazole and Artemether from Water. *Chem. Eng. J.* **2020**, *398*, 125544.

(256) Kusiak-Nejman, E.; Czyżewski, A.; Wanag, A.; Dubicki, M.; Sadłowski, M.; Wróbel, R. J.; Morawski, A. W. Photocatalytic Oxidation of Nitric Oxide over AgNPs/TiO$_2$-Loaded Carbon Fiber Cloths. *J. Environ. Manage.* **2020**, *262*, 110343.

(257) Cao, N.; Gu, M.; Gao, M.; Li, C.; Liu, K.; Zhao, X.; Feng, J.; Ren, Y.; Wei, T. A Three-Layer Photocatalyst Carbon Fibers/TiO$_2$ Seed/TiO$_2$ Nanorods with High Photocatalytic Degradation under Visible Light. *Appl. Surf. Sci.* **2020**, *530*, 147289.

(258) Nguyen, T. D.; Jitae, K.; Viet, N. M.; Thang, P. Q.; Huong, P. T. Combination of La-TiO$_2$ and Activated Carbon Fiber for Degradation of Toxic Organic Pollutants under the Visible Light. *J. Environ. Chem. Eng.* **2019**, *7* (3), 103180.

(259) Samy, M.; Ibrahim, M. G.; Gar Alalm, M.; Fujii, M.; Ookawara, S.; Ohno, T. Photocatalytic Degradation of Trimethoprim Using S-TiO$_2$ and Ru/WO$_3$/ZrO$_2$ Immobilized on Reusable Fixed Plates. *J. Water Process Eng.* **2020**, *33*, 3–10.

(260) Gar Alalm, M.; Samy, M.; Ookawara, S.; Ohno, T. Immobilization of S-TiO$_2$ on Reusable Aluminum Plates by Polysiloxane for Photocatalytic Degradation of 2,4-Dichlorophenol in Water. *J. Water Process Eng.* **2018**, *26*, 329–335.

(261) Ho, W.; Yu, J. C.; Lee, S. Photocatalytic Activity and Photo-Induced Hydrophilicity of Mesoporous TiO_2 Thin Films Coated on Aluminum Substrate. *Appl. Catal. B Environ.* **2007**, *73* (1), 135–143.

(262) Srikanth, B.; Goutham, R.; Badri Narayan, R.; Ramprasath, A.; Gopinath, K. P.; Sankaranarayanan, A. R. Recent Advancements in Supporting Materials for Immobilised Photocatalytic Applications in Waste Water Treatment. *J. Environ. Manage.* **2017**, *200*, 60–78.

(263) Li Puma, G.; Bono, A.; Krishnaiah, D.; Collin, J. G. Preparation of Titanium Dioxide Photocatalyst Loaded onto Activated Carbon Support Using Chemical Vapor Deposition: A Review Paper. *J. Hazard. Mater.* **2008**, *157* (2), 209–219.

(264) Pozzo, R. L.; Baltanás, M. A.; Cassano, A. E. Supported Titanium Oxide as Photocatalyst in Water Decontamination: State of the Art. *Catal. Today* **1997**, *39* (3), 219–231.

(265) Fabiyi, M. E.; Skelton, R. L. Photocatalytic Mineralisation of Methylene Blue Using Buoyant TiO_2-Coated Polystyrene Beads. *J. Photochem. Photobiol. A Chem.* **2000**, *132* (1), 121–128.

(266) Hashemzadeh, F.; Gaffarinejad, A.; Rahimi, R. Porous p-NiO/n-Nb_2O_5 Nanocomposites Prepared by an EISA Route with Enhanced Photocatalytic Activity in Simultaneous Cr (VI) Reduction and Methyl Orange Decolorization under Visible Light Irradiation. *J. Hazard. Mater.* **2015**, *286*, 64–74.

(267) Auerbach, S. S.; Bristol, D. W.; Peckham, J. C.; Travlos, G. S.; Hébert, C. D.; Chhabra, R. S. Toxicity and Carcinogenicity Studies of Methylene Blue Trihydrate in F344N Rats and B6C3F1 Mice. *Food Chem. Toxicol.* **2010**, *48* (1), 169–177.

(268) Stover, N. M. DIPHENYLCARBAZIDE AS A TEST FOR CHROMIUM. *J. Am. Chem. Soc.* **1928**, *50* (9), 2363–2366.

(269) Wang, N.; Xu, Y.; Zhu, L.; Shen, X.; Tang, H. Reconsideration to the Deactivation of TiO_2 Catalyst during Simultaneous Photocatalytic Reduction of Cr(VI) and Oxidation of Salicylic Acid. *J. Photochem. Photobiol. A Chem.* **2009**, *201* (2–3), 121–127.

(270) Choi, Y.; Koo, M. S.; Bokare, A. D.; Kim, D.; Bahnemann, D. W.; Choi, W. Sequential Process Combination of Photocatalytic Oxidation and Dark Reduction for the Removal of Organic Pollutants and Cr(VI) Using Ag/TiO_2. *Environ. Sci. Technol.* **2017**, *51* (7), 3973–3981.

(271) Du, Z.; Cheng, C.; Tan, L.; Lan, J.; Jiang, S.; Zhao, L.; Guo, R. Enhanced Photocatalytic Activity of Bi_2WO_6/TiO_2 Composite Coated Polyester Fabric under Visible Light Irradiation. *Appl. Surf. Sci.* **2018**, *435*, 626–634.

(272) Liu, S.; Sun, H.; Liu, S.; Wang, S. Graphene Facilitated Visible Light Photodegradation of Methylene Blue over Titanium Dioxide Photocatalysts. *Chem. Eng. J.* **2013**, *214*, 298–303.

(273) Barrera-Díaz, C. E.; Lugo-Lugo, V.; Bilyeu, B. A Review of Chemical,

Electrochemical and Biological Methods for Aqueous Cr(VI) Reduction. *J. Hazard. Mater.* **2012**, *223–224*, 1–12.

(274) Xu, S. C.; Ding, H. L.; Pan, S. S.; Luo, Y. Y.; Li, G. H. Electric-Field-Enhanced Photocatalytic Removal of Cr(VI) under Sunlight of TiO_2 Nanograss Mesh with Nondestructive Regeneration and Feasible Collection for Cr(III). *ACS Sustain. Chem. Eng.* **2016**, *4* (12), 6887–6893.

(275) Reinhardt, R. A. The Interaction of Chromium(III) Ion with Hydroxide Ion: An Experiment for the Undergraduate Inorganic Laboratory. *J. Chem. Educ.* **1966**, *43* (7), 382–384.